

ASPECTS OF TURBULENCE AND STOCHASTIC PROCESSES IN FLUID
MECHANICS

by

Jerry Lynn Dahlberg Jr.

A dissertation submitted to the faculty of
The University of North Carolina at Charlotte
in partial fulfillment of the requirements
for the degree of Doctor of Philosophy in
Mechanical Engineering

Charlotte

2018

Approved by:

Dr. Peter Tkacik

Dr. Russell Keanini

Dr. Samuel Hellman

Dr. Yogendra Kakad

Dr. Jae Hoon Lim

© 2018
Jerry Lynn Dahlberg Jr.
ALL RIGHTS RESERVED

ABSTRACT

JERRY LYNN DAHLBERG JR.. Aspects of Turbulence and Stochastic Processes
in Fluid Mechanics.

(Under the direction of DR. PETER TKACIK)

Three experimental studies are executed to examine aspects of turbulence and stochastic processes in fluid mechanics. Each experimental study is conducted in a different medium; water, wind and vibrated grain piles. Each study requires upgrades to existing equipment and data analysis hardware. The first two studies were conducted to develop a better understanding of the physics of flow conditions in general, and more specifically around a bluff body, while the third study utilizes a proposed experimental method to use macroscopic scale grains for studying molecular hydrodynamics.

The first experimental study examines wake structures in the flow past a bluff body utilizing the university hydrodynamic water channel and upgraded tomographic particle image velocimetry system. This volumetric PIV method utilizes an asymmetric camera configuration. This method allows for an accurate instantaneous visualization and characterization of flow structures present in the wake region without stitching multiple planes together to generate a time-averaged volume. One advantage of the updated system is that the flow can be realized on the time scale of the image capture, therefore wake motions can be seen as a function of time at the velocity tested. Tests were conducted to determine the best surface color of the model to improve processing methods. The results of this volumetric flow study are then compared to the benchmark diagram by Martinuzzi and Tropea.

The second study examines flow structures and pressure correlations in the wind tunnel utilizing a 100 Hz standard 2D PIV and five pressure sensors to gather data on the walls of the bluff body as well as eight pressure sensors in the floor of the wake

region. Three seeding materials are tested to determine which provided the most reliable and uniform results. The pressure data is utilized to determine if there is a correlation in the pressures on the sides of the bodies, specifically in the reattachment zones with pressures along the top of the body. The PIV data is then compared with the data analyzed in the previous study.

The third study examines molecular hydrodynamic processes in dense liquids and gases. This experiment utilizes a standard vibratory polishing rig and high speed camera to gather images to be used in a non-traditional PIV process which allows for macroscopic observations of a variety of dynamical processes. This data, coupled with force and vibration data demonstrate the framework of an analog method for studying molecular hydrodynamics, which is historically studied using photonic or neutron beam scattering techniques. Utilizing this unique experimental set up, the packing density as well as kinematic and dynamic viscosities are determined for seven different types of solid media.

ACKNOWLEDGMENTS

I would like to sincerely thank my advisor and mentor, Dr. Peter Tkacik for his never ending patience, friendship and guidance during my studies at UNC Charlotte. As an undergraduate student, the research opportunities I was afforded by Dr. Tkacik was instrumental in my decision to pursue a graduate degree. The support and faith that Dr. Tkacik provided, both on research and day to day operations of the research group provided me with the drive and motivation to succeed. I would also like to thank Dr. Russell Keanini for being the theoretical sounding board which was the foundation for much of this dissertation. His support was invaluable. I would like to thank Dr. Yogendra Kakad, Dr. Samuel Hellman and Dr. Jae Hoon Lim for serving on my committee and providing guidance.

The PIV portions of this dissertation was possible due to the equipment support and expertise of Dr. Hellman and assistance with PIV processing methods by Tucker Bisel. Franklin Greene was also instrumental in assisting with LabVIEW programming and equipment.

I also acknowledge the funding sources that made my PhD work possible. I have been funded and supported first by the Veterans Administration Vocational Rehabilitation Program, then the Office of Naval Research, as well as a University of North Carolina Graduate Summer Scholarship Fellowship.

Finally, I would like to personally thank my wife, Claudette and my children, Alexis and Dakota for encouraging and supporting me in my decision to return to school after a long military career. Additionally, I would like to thank Dr. Jerre Hill and Dr. Karen Thorsett-Hill for encouraging me to stay the course after my undergraduate and earn my Ph.D.

TABLE OF CONTENTS

LIST OF TABLES	ix
LIST OF FIGURES	xi
LIST OF SYMBOLS	xxi
CHAPTER 1: INTRODUCTION	1
CHAPTER 2: GENERAL BACKGROUND	4
2.1 Bluff Body Aerodynamics	4
2.2 Water channel	14
2.3 Wind tunnel	15
2.4 Molecular Hydrodynamics	18
2.5 Particle Image Velocimetry	21
2.5.1 Flow Seeding	23
2.5.2 Tomographic Particle Image Velocimetry	25
2.5.3 Particle Image Velocimetry Uncertainty	27
2.5.4 Non-Traditional Uses of Particle Image Velocimetry	28
CHAPTER 3: PIV AND WATER CHANNEL	30
3.1 Water Channel	30
3.2 Tomographic PIV	32
3.2.1 Cameras	33
3.2.2 Laser	34
3.2.3 Calibration	35
3.2.4 Seeding Particles	36
3.2.5 Model	36
3.2.6 Model Reflectivity	37
3.2.7 Data Processing	41
3.3 Water Channel Corrections for Non-Uniform Flow	41

3.4	Turbulent Structures in Wake Behind Wall Mounted Cube	50
3.4.1	Experimental Set Up and Processing	50
3.4.2	Flow Visualization Results	53
3.5	Summary	60
3.5.1	Future Work	61
CHAPTER 4: PIV AND WIND TUNNEL		63
4.1	Wind Tunnel	64
4.2	Particle Image Velocimetry	67
4.2.1	Camera	67
4.2.2	Laser	67
4.2.3	Calibration	68
4.2.4	Seeding Particles	69
4.3	Sensors and Program	70
4.4	Turbulent Structures and Pressure Correlations	73
4.4.1	Experimental Set Up and Processing	73
4.4.2	Empty Tunnel Results	75
4.4.3	Flow Visualization Results	83
4.4.4	Comparison between water channel and wind tunnel results	99
4.4.5	Pressure and Correlation Results	106
4.5	Summary	118
4.5.1	Future Work	120
CHAPTER 5: PIV AND MOLECULAR HYDRODYNAMIC PROPERTIES		121
5.1	Vibrating Grain System	122
5.1.1	Media	122
5.2	Particle Image Velocimetry	125
5.2.1	Camera	126
5.2.2	Calibration	126

5.3	Sensors and Programs	127
5.4	Experimental Setup and Processing	128
5.4.1	Data Acquisition	129
5.4.2	Data Processing	130
5.5	Results	131
5.5.1	Vibrational Spectra	131
5.5.2	Force Measurements	133
5.5.3	Velocity Measurements	142
5.5.4	Media Coefficient of Drag	144
5.5.5	Determining Reynolds Number	144
5.5.6	Kinematic and Dynamic Viscosity Realization for Vibrated Grain Piles	146
5.6	Summary	148
5.6.1	Future Work	149
	REFERENCES	150
	APPENDIX A: WIND TUNNEL PROGRAMS AND CODE	162
A.1	LabVIEW® Data Acquisition Program Block Diagram for Wind Tun- nel Pressures and Wind Velocity	162
A.2	MATLAB® Pressure Data Filtering Program	164
A.3	MATLAB® Pressure Data Correlation / Autocorrelation Program	170
A.4	Wake Region Cross-Correlation Tables	173
	APPENDIX B: VIBRATED GRAIN PILE PROGRAM AND CODE	179
B.1	LabVIEW® Frequency Data Acquisition Program Block Diagram	179
B.2	LabVIEW® Force Data Acquisition Program Block Diagram	180
B.3	MATLAB® Image Conversion Program	183
B.4	Reynolds number / Coefficient of Drag Table	185
	APPENDIX C: CURRICULUM VITAE	187

LIST OF TABLES

TABLE 4.1: Vector Map Statistics	86
TABLE 4.2: Pressure Autocorrelation	110
TABLE 4.3: Cross-Correlation between Sensors A and B	113
TABLE 4.4: Cross-Correlation with Front Sensor	115
TABLE 4.5: Cross-Correlation with Top Sensor	116
TABLE 4.6: Cross-Correlation with Rear Sensor	116
TABLE 4.7: Cross-Correlation with Right Sensor	117
TABLE 4.8: Cross-Correlation with Left Sensor	118
TABLE 5.1: Media Dimensions and Characteristics	124
TABLE 5.2: Media Weight and Calculated Packing Densities	124
TABLE 5.3: Media Weight and Calculated Densities by Geometry	125
TABLE 5.4: Average Impact Measurement and Force	133
TABLE 5.5: Point Velocities	143
TABLE 5.6: Coefficient of Drag	144
TABLE 5.7: Reynolds Number Comparison	146
TABLE 5.8: Kinematic and Dynamic Viscosity	148
TABLE 5.9: Common Material Dynamic Viscosity	148
TABLE A.1: Cross-Correlation with Sensor H	173
TABLE A.2: Cross-Correlation with Sensor I	173
TABLE A.3: Cross-Correlation with Sensor J	174
TABLE A.4: Cross-Correlation with Sensor K	174
TABLE A.5: Cross-Correlation with Sensor L	175
TABLE A.6: Cross-Correlation with Sensor M	176
TABLE A.7: Cross-Correlation with Sensor N	177
TABLE A.8: Cross-Correlation with Sensor O	178

TABLE B.1: Reynolds Number Comparison

185

TABLE B.2: Reynolds Number Comparison Continued

186

LIST OF FIGURES

FIGURE 2.1:	Simplified schematic of the Martinuzzi and Tropea representation of flow around a surface mounted cube	7
FIGURE 2.2:	Schematic of flow around a surface mounted cube identifying structures A)top recirculating vortex, B) side recirculating vortex, C) arch (horseshoe) vortex, and D) trumpet (horseshoe) vortex	10
FIGURE 2.3:	Commercially available ELD model 504 ducted water tunnel	14
FIGURE 2.4:	UNC Charlotte water channel during initial build	15
FIGURE 2.5:	Commercially available Aerolab open return educational wind-tunnel	16
FIGURE 2.6:	Commercially available Aerolab closed return wind tunnel	17
FIGURE 3.1:	Side view of water channel as photographed during move and assembly by Dr. Samuel Hellman	31
FIGURE 3.2:	Top view of water channel with overhead crane and mezzanine installed.	32
FIGURE 3.3:	Schematic of the tomographic PIV camera set up and test area	34
FIGURE 3.4:	Side view of tomographic PIV camera set up and test area	34
FIGURE 3.5:	Prism tank installed on side of water channel with arrows depicting the matching camera and wall angles	35
FIGURE 3.6:	Image of cube mounted to flat plate A) from the top and B) from the side as mounted in the water channel	37
FIGURE 3.7:	Image of cube painted flat white with over-saturation taken during color comparison test	38
FIGURE 3.8:	Image of cube painted flat black during color comparison test	39

FIGURE 3.9:	Image of cube painted florescent orange during color comparison test	39
FIGURE 3.10:	Image of cube painted florescent pink during color comparison test	40
FIGURE 3.11:	Image of cube painted with Rhodamine 6G taken during color comparison test	40
FIGURE 3.12:	Voxel pre-processing steps; A) define mask, B) apply mask, C) background subtraction, D) image arithmetic. Image modified from Fleischhauer <i>et al.</i> [1]	42
FIGURE 3.13:	$180\text{ mm} \times 100\text{ mm} \times 70\text{ mm}$ processed vector field at motor frequency of 25 Hz showing non-uniform flow.	42
FIGURE 3.14:	$180\text{ mm} \times 100\text{ mm} \times 70\text{ mm}$ processed vector field at motor frequency of A) 7.5 Hz, B) 10 Hz and C) 15 Hz showing non-uniform flow.	43
FIGURE 3.15:	Velocity profile in the water channel test section prior to flow modification	43
FIGURE 3.16:	Schematic of water channel modified from Dr. Samuel Hellman's dissertation demonstrating A) toroidal flow area, B) high speed flow area, C) recirculation area and D) recirculation area	44
FIGURE 3.17:	$180\text{ mm} \times 100\text{ mm} \times 70\text{ mm}$ processed vector field at motor frequency of 25 Hz after screen initial installation	46
FIGURE 3.18:	$180\text{ mm} \times 100\text{ mm} \times 70\text{ mm}$ processed vector field at motor frequency of A) 7.5 Hz, B) 10 Hz and C) 15 Hz showing non-uniform flow with screens installed	46
FIGURE 3.19:	$180\text{ mm} \times 100\text{ mm} \times 70\text{ mm}$ processed vector field at motor frequency of 25 Hz of A) initial and B) post screen installation flow.	47

- FIGURE 3.20: Anti-cavitation plate installed over water channel motor to reduce cavitation 47
- FIGURE 3.21: $180\text{ mm} \times 100\text{ mm} \times 70\text{ mm}$ processed vector field at motor frequency of 25 Hz after anti-cavitation plate was installed 48
- FIGURE 3.22: $180\text{ mm} \times 100\text{ mm} \times 70\text{ mm}$ processed vector field at motor frequency of 25 Hz comparison of the A) initial and B) third test 48
- FIGURE 3.23: $180\text{ mm} \times 100\text{ mm} \times 70\text{ mm}$ processed vector field at motor frequency of 25 Hz after screens were installed at the entrance of the nozzle 49
- FIGURE 3.24: $180\text{ mm} \times 100\text{ mm} \times 70\text{ mm}$ processed vector field at motor frequency of A) 7.5 Hz, B) 10 Hz and C) 15 Hz showing improvements to the non-uniform flow 50
- FIGURE 3.25: $180\text{ mm} \times 100\text{ mm} \times 70\text{ mm}$ processed vector field at motor frequency of 25 Hz comparison of the A) initial and B) third test 50
- FIGURE 3.26: Comparison of the Martinuzzi and Tropea schematic and experimental results showing A) top recirculating vortex and C) rear arch vortex. 53
- FIGURE 3.27: Comparison of the Martinuzzi and Tropea schematic and experimental results showing B) side recirculating vortex and D) trumpet (horseshoe) vortex. 54
- FIGURE 3.28: Flow of combined vector maps as seen from the top showing A) top recirculating vortex, B) side recirculating vortex, C) rear arch vortex and D) trumpet (horseshoe) vortex. 54
- FIGURE 3.29: Flow of combined vector maps as seen from the near side showing A) top recirculating vortex, B) side recirculating vortex, C) rear arch vortex and the outside edge of D) trumpet (horseshoe) vortex. 55

- FIGURE 3.30: Flow of combined vector maps as seen viewing the rear face showing A) top recirculating vortex and B) side recirculating vortex. 55
- FIGURE 3.31: Flow of combined vector maps from the side showing A) rear arch vortex, B) top recirculation, C) top front separation and D) flow moving up rear face of cube 56
- FIGURE 3.32: Close up view from the side of the rear arch vortex showing A) the center peak of the vortex, B) the reverse flow up the rear face of the cube and C) the joining of the vortex and the separated flow over the cube. 56
- FIGURE 3.33: Close up view from the side of the top of the cube showing A) the top recirculation vortex, B) the front separated flow and C) reverse flow along rear face. 57
- FIGURE 3.34: Center plane slice of flow around the cube as seen from the side showing velocities at A) front face, B) top corner flow separation, C) top recirculating region, D) reverse flow and E) rear arch vortex region. 58
- FIGURE 3.35: Plane slice $2mm$ above cube of flow around the cube as seen from the top showing velocities at A) separation around the side of the cube, B) side recirculating vortex, C) higher velocity region between trumpet horseshoe vortex and rear arch vortex and D) rear arch vortex region. 58
- FIGURE 3.36: Isosurface of the flow at $0.04 \frac{m}{sec}$ showing A) top recirculating vortex, B) rear arch vortex and C) trumpet horseshoe vortex 59
- FIGURE 3.37: Zoomed in view of iso surface of the flow at $0.04 \frac{m}{sec}$ showing A) top recirculating vortex and B) rear arch vortex 60

FIGURE 4.1:	Original configuration of UNC Charlotte Motor Sports Research Lab scale wind tunnel	65
FIGURE 4.2:	Wind tunnel after wall replacement	65
FIGURE 4.3:	Wind tunnel roof center section with pitot tube installed	65
FIGURE 4.4:	Modular test section floor with A) cube and pressure sensors and B) rolling road	66
FIGURE 4.5:	Schematic of Eiffel wind tunnel with settling chamber	67
FIGURE 4.6:	Laser and camera attached to isolated frame	68
FIGURE 4.7:	PIV Measure Scale Factor window showing location markers, absolute distance and computed scale factor	69
FIGURE 4.8:	Placement of pressure sensor taps along floor and walls of cube	70
FIGURE 4.9:	Front screen of wind tunnel pressure and airspeed LabView® program A) airspeed, B) pressure before cube, C) pressure on the cube and D) pressure after the cube.	71
FIGURE 4.10:	Schematic of wind tunnel test section with placement and iden- tification of sensors	72
FIGURE 4.11:	Back panel of wind tunnel pressure and airspeed LabView® program	72
FIGURE 4.12:	Velocity profile at the cube location with the cube removed	76
FIGURE 4.13:	Boundary layer mean profile at the cube location with the cube removed	77
FIGURE 4.14:	Raw data image of empty tunnel smoke test	77
FIGURE 4.15:	Processed vector map of empty tunnel smoke test	78
FIGURE 4.16:	Processed vector statistics map of empty tunnel smoke test	78
FIGURE 4.17:	Processed vector statistics map of smoke test with expanded view of boundary layer	79
FIGURE 4.18:	Raw data image of empty tunnel olive oil test	79

FIGURE 4.19: Processed vector map of empty tunnel olive oil test	80
FIGURE 4.20: Processed vector statistics map of empty tunnel olive oil test	81
FIGURE 4.21: Processed vector statistics map of olive oil test with expanded view of boundary layer	81
FIGURE 4.22: Raw data image of empty tunnel helium filled soap bubble test	82
FIGURE 4.23: Processed vector map of empty tunnel helium filled soap bubble test	82
FIGURE 4.24: Data pre-processing steps; A) define mask and B) apply mask	85
FIGURE 4.25: Full combined vector map of -10 <i>mm</i> (near side) plane	87
FIGURE 4.26: Single processed vector map of the 0 <i>mm</i> /near face plane	87
FIGURE 4.27: Full combined vector map of 0 <i>mm</i> /near face showing A) gap in data, B) area of top recirculating vortex, C) flow moving up the rear face of the cube, D) area of rear arch vortex and E) erroneous vectors near floor	88
FIGURE 4.28: Full combined vector map of 10 <i>mm</i> from the close edge of the cube showing A) the top recirculating vortex, B) flow moving up the rear face of the cube and C) the rear arch vortex	89
FIGURE 4.29: Full combined vector map of 20 <i>mm</i> from the close edge of the cube showing A) the top recirculating vortex, B) separation region on top rear corner, C) wide area of flow moving up the rear face of the cube and D) core of the rear arch vortex	89
FIGURE 4.30: Full combined vector map of 30 <i>mm</i> from the close edge of the cube showing A) the top recirculating vortex, B) separation region on top rear corner, C) wide area of flow moving up the rear face of the cube and D) core of the rear arch vortex	90

- FIGURE 4.31: Full combined vector map of 40 *mm* from the close edge of the cube showing A) the top recirculating vortex, B) separation region on top rear corner, C) near 0 velocity area at base of cube and D) center of the core of the rear arch vortex 91
- FIGURE 4.32: Full combined vector map of 50 *mm* from the close edge of the cube showing higher vector concentrations at the A) flow separation point on top edge and B) in the rear horseshoe vortex 92
- FIGURE 4.33: Full combined vector map of 60 *mm* from the close edge of the cube showing higher vector concentrations at the A) flow separation point on top edge and B) in the rear horseshoe vortex 92
- FIGURE 4.34: Full combined vector map of 70 *mm* from the close edge of the cube showing higher vector concentrations at the A) flow separation point on top edge and B) in the rear arch vortex 93
- FIGURE 4.35: Full combined vector map of 80 *mm*/far face showing A) area of top recirculating vortex, B) flow moving up the rear face of the cube and C) area of rear arch vortex 93
- FIGURE 4.36: Full combined vector map of 90 *mm* with A) separation area along top and rear of cube 94
- FIGURE 4.37: Reduced density combined vector map of -10 *mm* (near side) plane 95
- FIGURE 4.38: Reduced density combined vector map of 40 *mm* plane showing A) core of rear horseshoe vortex and B) reverse flow region along rear of cube 95
- FIGURE 4.39: Tecplot image with eleven planes inserted 96
- FIGURE 4.40: Flow of combined vector planes as seen from the top showing A) top recirculating vortex, B) side recirculating vortex and C) rear arch vortex 97

FIGURE 4.41: Flow of combined vector planes as seen from the top showing A) top recirculating vortex, B) side recirculating vortex and C) rear arch vortex	97
FIGURE 4.42: Flow of combined center three vector planes as seen from the top showing A) top recirculating vortex and B) rear arch vortex	98
FIGURE 4.43: Flow of combined center three vector planes as seen from the side showing A) top recirculating vortex B) separation zone and C) rear arch vortex	99
FIGURE 4.44: Comparison of wind tunnel (top) and water channel (bottom) combined streamline maps showing A) top recirculating vortex B) side recirculating vortex, C) rear arch vortex and D) trumpet (horseshoe) vortex	100
FIGURE 4.45: Comparison of wind tunnel (top) and water channel (bottom) combined streamline maps (cube width) showing A) top recir- culating region B) reverse flow region and C) rear arch vortex	102
FIGURE 4.46: Comparison of wind tunnel (top) and water channel (bottom) combined streamline maps showing the top recirculating region	103
FIGURE 4.47: Comparison of wind tunnel (top) and water channel (bottom) combined streamline maps showing the rear arch vortex	105
FIGURE 4.48: Raw pressure data in region upstream in front of the cube	107
FIGURE 4.49: Filtered pressure data in region of upstream in front of the cube	107
FIGURE 4.50: Raw pressure data on the walls of the cube	108
FIGURE 4.51: Filtered pressure data on the walls of the cube	109
FIGURE 4.52: Raw pressure data in wake region of cube from 0.5H to 4H	109
FIGURE 4.53: Filtered pressure data in wake region of cube from 0.5H to 4H	110
FIGURE 4.54: Number of lags in autocorrelation based on location for pressure data	112

FIGURE 4.55:	Cross-correlation graph between sensors A and B in front of the cube for the first 30,000 data points	113
FIGURE 5.1:	Vibratory system experimental set-up with camera and lighting modified from Dahlberg <i>et al</i>	123
FIGURE 5.2:	Seven media types used. A) RS 10/10, B) RS 19K, C) RS 10/22 ZS, D) RDP 09/09, E) 2mm Ball, F) RS 10/10S and G) H-10 08D	123
FIGURE 5.3:	Density of media by geometry and displacement	125
FIGURE 5.4:	Camera field of view with ruler used for calibration	126
FIGURE 5.5:	Load cell drag measurement apparatus	127
FIGURE 5.6:	Front screen of vibrated grain piles A) accelerometer LabView® program and B) force LabView® program.	128
FIGURE 5.7:	Bowl vibrational spectra without media present	132
FIGURE 5.8:	Bowl vibrational spectra with RS 10/10 media (blue) and without (red) media present	133
FIGURE 5.9:	Normalized bowl vibrational spectra without media overlaid on vibrational spectra with media present for A)RS 19K B) RS 10/22 ZX C) RCP 09/09 D) 2mm Ball E) RS 10/10S and F) 2050 40/13 DZ	134
FIGURE 5.10:	A) Raw force data and B) histogram of the force data from one 10/10S test	135
FIGURE 5.11:	A) Raw force data and B) histogram of the force data from one RS 19K test	136
FIGURE 5.12:	A) Raw force data and B) histogram of the force data from one RS 10/22 ZS test	137
FIGURE 5.13:	A) Raw force data and B) histogram of the force data from one RCP 09/09 test	138

FIGURE 5.14: A) Raw force data and B) histogram of the force data from one 2mm ball test	139
FIGURE 5.15: A) Raw force data and B) histogram of the force data from one RS 10/10 test	140
FIGURE 5.16: A) Raw force data and B) histogram of the force data from one 2050 40/13 DZ test	141
FIGURE 5.17: RS 10/10S grain pile A) without force sensor B) with force sensor C) vector map without force sensor D) vector map with force sensor	143
FIGURE A.1: Block diagram for LabVIEW® program used to acquire pres- sure and velocity data. Detailed areas outlined in red box is shown in following five figures.	162
FIGURE A.2: Detailed view of block 1 from block diagram in Figure A.1	162
FIGURE A.3: Detailed view of block 2 from block diagram in Figure A.1	163
FIGURE A.4: Detailed view of block 3 from block diagram in Figure A.1	163
FIGURE A.5: Detailed view of block 4 from block diagram in Figure A.1	164
FIGURE A.6: Detailed view of block 5 from block diagram in Figure A.1	164
FIGURE B.1: Block diagram for LabVIEW® program used to acquire ac- celerometer data in vibratory polishing experiments	179
FIGURE B.2: Block diagram for LabVIEW® program used to acquire force data in vibratory polishing experiments. Detailed areas out- lined in red box is shown in following five figures.	180
FIGURE B.3: Detailed view of block 1 from block diagram in Figure B.2	181
FIGURE B.4: Detailed view of block 2 from block diagram in Figure B.2	182
FIGURE B.5: Detailed view of block 3 from block diagram in Figure B.2	182
FIGURE B.6: Detailed view of block 4 from block diagram in Figure B.2	182
FIGURE B.7: Detailed view of block 5 from block diagram in Figure B.2	183

List of Symbols

x, y, z	Cartesian Coordinate System
h	Height of Tunnel / Channel
l	Characteristic Length
M	Mass
A	Orthogonal Projection Area of the Cylinder
H	Height of Model
L	Length of Model
W	Width of Model
St	Strouhal Number
f_s	Vortex Shedding Frequency
C_d	Coefficient of Drag
F_d	Drag Force
Re	Reynolds Number
Re_l	Reynolds Number based on Characteristic Length
Re_h	Reynolds Number based on Height of Tunnel
Re_L	Reynolds Number based Length of Model
ρ	Fluid Density
ρ_p	Packing Density
U_∞	Free Stream Flow Velocity
v_A	Air Velocity
v_m	Media Velocity
μ	Dynamic Viscosity
ν	Kinematic Viscosity
γ	Euler Constant
τ	Shear Stress

δ_L	Laminar Boundary Layer Thickness
δ_T	Turbulent Boundary Layer Thickness
Δt	Time Step
ΔP	Pressure Difference
du	differential velocity step
dy	differential distance step
V_p	Packing Volume

CHAPTER 1: INTRODUCTION

Instabilities in the wake region behind bodies inside a flow are of great interest to engineers from all disciplines. One of the most common shapes used in experimentation and simulation for all engineering disciplines is the bluff body. These bluff bodies are used in place of the exact geometry to gather preliminary data. The forces and pressures associated with the flow are important elements to be considered for vehicles, aerospace, underwater structures, buildings and a multitude of other areas. The flow in the turbulent wake region behind the bluff body directly effects the forces and pressures, both steady and unsteady, that act on the body. Identifying flow structures, how they form and their magnitudes in the wake region, is key to better understanding the physics of the flow conditions around bluff bodies.

One focus of this dissertation is to visualize turbulent flow structures behind a cube in two different mediums; water and wind. Particle image velocimetry (PIV) is used to experimentally examine two specific cases of the wake structure identification and their formation. This dissertation also addresses a nontraditional approach where PIV is used to study molecular scale hydrodynamic processes in vibrated grain systems, which are used to represent dense gases and liquids. This document is broken down into five chapters which contain specific information that was relevant to conduct the research.

Chapter 2 provides general background on the equipment used in this document, to include the water channel, wind tunnel, vibrated grain systems and particle image velocimetry. Chapter 2 also discusses the history and current status of bluff body aerodynamics testing and how the experimental results impact other fluids research

methods such as computational fluid dynamics.

Chapter 3 provides information on upgrades to the university water channel and the existing Stereoscopic Particle Image Velocimetry (SPIV) system in the water channel to a four camera Tomographic Particle Image Velocimetry (TomoPIV) system, which is the one of only a handful of diagnostic tools available for instantaneously measuring velocities in three spatial dimensions. This updated system was used for all of the flow visualization experiments described in the water channel. The TomoPIV system, when updated, was one of only a handful of its kind and capability in the United States. Chapter 3 discusses the experimental set up and preliminary tests used to improve the processing of the newly upgraded TomoPIV system. Finally Chapter 3 shows the results of the TomoPIV study of the flow around a bluff body in which flow structures around a cube were identified and compared to the historic benchmark schematic presented by Martinuzzi and Tropea of flow around a wall-mounted cube.

Chapter 4 describes the updates to the 0.3 m^2 by 0.7 m long test section, Eiffel wind tunnel to allow the addition of flow visualization equipment and modular test section used to study the flow structures around a bluff body. A 2D PIV system with 100 Hz capabilities was installed along with a series of pressure sensors to gather data on the bluff body as well as in the wake region. A series of tests were conducted determine which type of flow seeding provides the most reliable results in the wind tunnel for the current experimental conditions. This chapter then shows the flow structures around the same 0.0058 m^2 cube utilized in the water channel as well as the pressure data gathered on the sides of the model and in the wake region. The flow visualization results are compared to the results attained in Chapter 3 and a cross-correlation of the pressure data in the wake on the cube faces are conducted.

Chapter 5 describes a vibrated grain piles experiment in which PIV was utilized in a non-traditional method to process data gathered from a high speed camera. The

results of the PIV data as well as bowl vibration frequency and granular impact force data were used to study molecular hydrodynamic processes in dense fluids and provide direct macroscopic observation of dynamical processes known and predicted to exist. From the experimental results, the packing density as well as the kinematic and dynamic viscosities were determined.

CHAPTER 2: GENERAL BACKGROUND

2.1 Bluff Body Aerodynamics

Instabilities in the wake region behind bodies inside a flow are of great interest to engineers from multiple disciplines. The flow and the forces and pressures associated with that flow are important elements to be considered in the design and implementation of vehicles, buildings, underwater structures, aerospace and a multitude of other areas. One common method of experimentation and simulation for all of these disciplines is to use a bluff body in place of the exact geometry of the structure in question to gather preliminary data.

A bluff body can be simply described as any square or near square shape and is used in an experiment or computation simulation. These elements may be used by themselves, or in a series of similar elements. The bluff bodies are easy to manufacture and provide reliable baseline results. A typical bluff body has sharp edges and produces separation regions larger than an aerodynamic body. A second common shape used to study wake regions, separation regions and turbulence qualities is known as the rear facing step. The rear facing step is basically a bluff body without a front face, so there is no stagnation point.

When conducting experimentation into flow and flow structures around bluff or aerodynamic bodies, the Reynolds number (Re) is an important reportable quantity. The Reynolds number is a dimensionless number, which is the ratio of inertial forces to viscous forces and can be used to predict flow patterns in different fluid flow situations. Laminar flow is known to have low Reynolds numbers where turbulent flow has large numbers. The Reynolds number is calculated based on fluid properties

and model length as shown in Equation 2.1.

$$Re = \frac{\rho U_{\infty} l}{\mu} = \frac{U_{\infty} l}{\nu} \quad (2.1)$$

Where Re is the dimensionless Reynolds number, ρ is flow fluid density in $\frac{kg}{m^3}$, l is the characteristic length of the body in m , U_{∞} is the flow velocity in $\frac{m}{sec}$, μ is the dynamic viscosity of the working fluid in $\frac{kg}{m*sec}$ and ν is the kinematic viscosity of the working fluid in $\frac{m^2}{sec}$.

The flow structures around bluff bodies of numerous types have been studied through a large variety of experimental means over the last 50 years. Specifically the flow around wall mounted cubes have been used to study lift and drag[2, 3], vortex formations [4, 5], turbulence and shear in the wake [6–8], pressure, and velocity, basic flow field structures [7, 9–12] and even energy distribution in the wake [13]. Other types of bluff bodies such as rear facing steps, cylinders and Ahmed bodies have been used to study vehicle pollutants [14, 15], flow and turbulence structures [16–21], aerodynamic yaw [22] and Reynolds number effects [23, 24]. As methods and equipment continue to improve, experimental studies into the flow around cubic bluff bodies presents the opportunity to gather data on a three-dimensional object that by the nature of its shape produce large amounts of vortices and turbulence compared to more streamline bodies. Bluff bodies also produce large drag values due to no pressure recovery region on the rear of the body [3].

Aerodynamic forces have been studied for decades in an attempt to understand the flow, its patterns and its effects. One of the first know studies using cubes was conducted by Hansche and Rinehart [2] in the early 1950s. They used steel cubes to determine the coefficient of drag (C_D) for projectiles in flight at speeds between .5 and 3.5 Mach to predict the behavior of missiles[2]. In 1955 Roshko was conducting experiments to gain a greater understanding of wake and vortex formations[4]. The goal was to combine the potential outer flow and the wake into a

single theory through the uses of the Kirchhoff method, which determines drag based on pressure distribution[4]. In these early experiments, the pressure distribution was the primary measurable variable and was used to determine all of the other variables. Images of the experiment could be gathered utilizing cameras, but they were only able to capture a few images in a minute and could take days to process.

In 1977, Castro and Robins [6] instrumented a cube with pressure taps to investigate the flow around a 60 *mm* wall-mounted brass cube. This was one of the preliminary investigations into three dimensional shapes. This investigation was valuable in determining surface constraints, but lacked the capability to determine the complex nature of the flow. Castro and Robins also utilized cubes positioned at different angles to the wind flow in a wind tunnel to measure velocities and pressures inside the wake region[6–8]. While studying the effects of upstream turbulence and shear on the wake, it was determined that the flow around the cube is highly dependent on its orientation with respect to the flow. When all other variables are constant, the greater the angle from 0 ° to 45 ° the more the near wake and pressure field is dominated by strong vortices shed from the top edge of the cube[6–8]. It was also determined that the turbulence and upstream shear alter the pressure around the cube for Reynolds numbers between 2×10^4 to 1×10^5 [6–8].

For decades, all of the research, including flow around three dimensional objects, focused on a single parameter. One of the first advances into studying a fully three dimension flow around obstacles came from Martinuzzi and Tropea [9] who utilized static pressure measurements, oil-film, crystal violet, and laser-sheet visualization techniques to investigate the flow over a wall-mounted three dimensional cube and compared it to a two dimensional rib. Theses studies were conducted in a water channel as well as in wind tunnel at various Reynolds numbers and produced results that were used to develop a schematic which became the benchmark for future flow studies[9, 12]. Figure 2.1 shows a simplified version of the Martinuzzi and Hussein

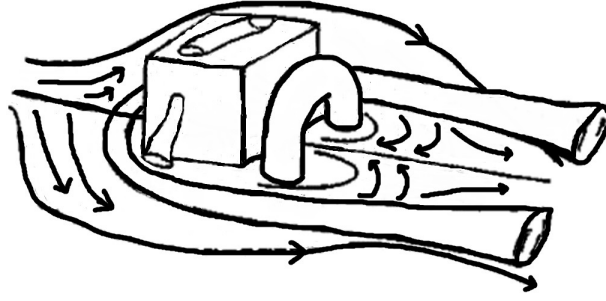


Figure 2.1: Simplified schematic of the Martinuzzi and Tropea representation of flow around a surface mounted cube [9]

schematic. Martinuzzi continued this line of research with Havel in a wind tunnel and expanded it to study the flow around surface mounted cubes in tandem[5, 10]. They were able to determine that certain flow structures are based on obstacle spacing[10] and that vortex shedding for this configuration was strongly dependent on interference between the vertical flow stream and the side shear layers[5].

Hussein and Martinuzzi then studied the turbulent wake region behind a surface mounted cube. They were focused on the production, convection and transport of turbulence kinetic energy using Laser Doppler Anemometry (LDA) along the centerline of the cube and then compared those experimental results to modeled terms [13].

Early in the 1980s, governmental regulations began to demand more of vehicle manufactures, specifically reduction of emissions and improvements in fuel conservation. Eskridge and Thompson [14, 15] utilized a wind tunnel with a rolling road and fixed block shaped vehicle suspended over the rolling road to simulate conditions a road vehicle may experience. They studied vertical, lateral mean and fluctuating velocities as well as Reynolds stresses in the wake region to predict pollutant transport along roadways. The experimental set up allowed for them to concentrate on momentum wakes containing vortices that disappear when time averaged. This research was

continued and developed an initial model to predict velocity and turbulence lengths and fields to determine pollution concentrations carried in the wake region of vehicles.

In the mid 1980s, Talmon *et al* conducted flow visualization and Reynolds-stress measurements in an investigation of a turbulent boundary layer in a water channel[25]. They used Laser Doppler Velocimetry (LDV) with hydrogen bubbles injected into the water stream of a water tunnel to visualize the flow patterns while measuring velocities and Reynolds stresses.

Adam and Johnson studied flow structures in the near-wall region of a turbulent flow. They utilized a slow speed wind tunnel, LDA and Pulsed Wire Anemometer (PWA) to measure velocities inside the turbulent separated flow region behind a backward facing step. This study suggested that the shear stress in this region is highly viscous with high fluctuations, yet remains laminar, like in nature[16]. They continued to study the turbulent flow inside the near wall region by first looking at the pressure and turbulence quantities effects on the reattachment flow structure [17] and then the reattachment length and wall shear stress effects[18].

In the mid 1990s, Jovic and Driver used a backward facing step and Laser-Oil Flow Interferometry (LOFI) to measure shear stress on the wall and determine that the skin friction coefficient decreased as the Reynolds number increased [24]. This study was part of a larger experiment conducted at the National Aeronautics and Space Administration (NASA) Ames Research Center to validate a computational Direct Numerical Simulation (DNS) solver used by NASA. The overall study was utilized to fill a gap in experimental data available at that time at $Re=5100$. It was determined that the separated flow field is divided into four interrelated areas. These areas are the separated shear, recirculating under the shear layer, a reattachment region and the recovery region [24].

Vehicle aerodynamics have also benefited from the study of bluff bodies. Gohoke *et al* utilized a bluff body to study the effect of cross winds on vehicles and gain a

deeper understanding of the influence of the flow structures on the stability of the vehicle [11].

Through 100 years of experimentation and analysis of the wake behind a moving body, either bluff or otherwise, has led to several breakthroughs. All of these different studies have shown that certain structures and phenomena are to be expected. On a bluff body, there will be a stagnation point on the front face normal to the flow, separation along the leading edges, and reattachment locations at some point along the top and sides. There will also be a wake region behind the body, whose size and volatility is dependent on the velocity of the flow and features of the body. The wake region is further broken up into two separate areas, the near wake and the far wake. The near wake area is described as the region directly downstream from the model and is bounded by free shear layers where the flow is reversed [26], typically one to three body length. The far wake is defined as the region following the near wake, where the wake is fully developed. All of these events or features occur to some extent at all Reynolds numbers. The large drag values produced by bluff bodies are an effect of the pressure gradients along the rear face of the body, inside the wake region.

One of the most documented and researched instabilities inside the wake region is the vortex shedding and its interactions in the flow behind the body. Several of the cited experiments report the appearance of a trumpet horseshoe type vortex that initiates on the front face of the object and wraps around the base of the body as seen in Figure 2.2, Structure D and an arch vortex on the wake side as seen in Figure 2.2, Structure C. Additionally there are flow separation regions along the top and sides due to sharp angles that result in additional vortex recirculation as seen in Figure 2.2, Structures A and B [9, 10, 12, 13, 20, 25]. Unfortunately, most experiments historically provide only visual results for the phenomena and very little measurements inside those regions due to the difficulty in acquiring reliable data without effecting the flow. These researchers have also successfully gathered data

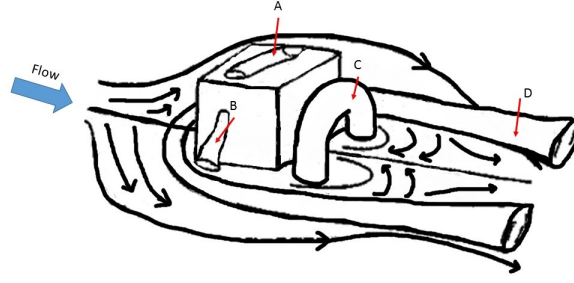


Figure 2.2: Schematic of flow around a surface mounted cube identifying structures A) top recirculating vortex, B) side recirculating vortex, C) arch (horseshoe) vortex, and D) trumpet (horseshoe) vortex

corresponding to Reynolds normal stresses and shear stresses, wall static pressures and mean velocities.

More recent work has been focused on the formation and shedding of spanwise vortices, also known as Kármán vortices, inside the near wake region [19, 20, 26, 27]. The vortex shedding contributes to the time averaged aerodynamic forces as well as the generation of fluctuating forces that act on the body[27]. The frequency of this shedding is described by the Strouhal number, which is a function of the Reynolds number[19, 27] and calculated using Equation 2.2.

$$St = \frac{f_s l}{U_\infty} \quad (2.2)$$

Where St is the dimensionless Strouhal number, f_s is the vortex shedding frequency in $\frac{1}{sec}$, l is the characteristic length of the body in m and U_∞ is the flow velocity in $\frac{m}{sec}$.

Although pressure correlations inside turbulent boundary layers have been theorized[28], very little work has been focused on finding the correlations[29, 30] in comparison to a large body of work focused on space and time correlations for velocity inside the

same region[31–33] . Additionally, there is no known quantitative correlation between the pressures on the top and sides of bodies, inside the separated and reattachment zones. There is also no known confirmed method of predicting instantaneous forces and pressures in and around the wake zone of a bluff body, especially at higher Reynolds number. A more thorough understanding of how wake structures develop is required to improve computation methods and simulations.

The largest problem associated with gathering pressure data inside the flow is the disturbance caused by the sensor itself. To minimize the disturbance, the pressure taps are placed inside of walls or on flat edges to gather the surface pressures. The pressure taps inside the wall, or model will record fluctuations which are created by the moving turbulent eddies inside the boundary layer as they pass the pressure sensor. The larger the eddies, the greater the fluctuations. Willmarth and Tu used space-time correlations of the wall pressures and velocity to investigate the evolution of turbulent eddies[29].

As stated earlier, measurement techniques for pressure are typically intrusive and are limited to the immediate location of the pressure tap inside the flow. This restricts the ability to measure or conduct any valuable analysis of an entire pressure field. Particle Image Velocimetry (PIV) systems have recently been used to determine pressure field data inside fully developed flows[34] and in the vicinity of a moving structure[35]. Velocity data previously gathered and indexed from PIV or Particle Tracking Velocimetry (PTV) has also been used to determine the pressure fields[36]. Since there is no direct method of measuring the pressure with a PIV system, the experimental velocity measurements are combined with the flow governing equations to calculate the pressure[37]. To determine the pressure field information, the velocity measurement is used in the Navier-Stokes equation with some simplifications[34] such as incompressibility and small temperature variations. One significant draw back to the pressure estimations based on velocity measurements is the uncertainty associated

with the velocity measurements[36].

Although a large amount of experimental work has been done in the area of turbulence modeling, a majority of the work has transferred to computational assessments of the flow. This transfer has led to a lack of current experimental results to compare to.

In the early 1990s, several new computational programs were invented. With these inventions, the decreasing cost of computing and increasing demand for simulated results, existing experimental values that could be used as a baseline for these programs became critical. This forced the experimentation to expand and become more focused on three dimensional objects and increase the accuracy of that data that could be achieved. Like with the experimental studies discussed earlier, many computation fluid dynamics (CFD) simulations use simple bluff bodies to simulate more complex shapes. These bluff bodies, to include rear facing steps are utilized because of their simple geometry and ease of numerical modeling. These early simulations were compared to experimental results to validate their procedures and findings.

Many different CFD model simulations have been conducted to compare their results to the the Martinuzzi and Tropea benchmark study[9], including, Direct Numerical Simulations (DNS)[38], Large Eddy Simulations (LES)[39–41], Detached Eddy Simulations (DES) [42, 43], Reynolds Averaged Navier-Stokes (RANS) simulations, and hybrids models[44]. The lack of current published experimental results forces computational methods to use results that are decades old. Curley *et al.* [44] used the results of Castro and Robins which was published in 1977 and Martinuzzi and Tropea from 1993 to conduct their evaluations of two turbulence models. Farhadi and Sedighi [45] also used Martinuzzi and Tropea’s results as well as Martinuzzi and Havel to simulate flow over tandem surface-mounted cubes numerically. Krajnović and Davidson [40] used Larousee results[12] from 1991 to conduct their simulations. Besides those already listed, Martinuzzi has produced numerous experimental results

with several co-authors, and those results are used for a large majority of the cube simulation papers[46–48].

Computational researchers use a variety of methods to verify their results, such as Yakhot *et al.* [38] and Chien [49] that have used multiple experimental results to validate their computations [38, 49] or Spalart who verifies RANS solvers with DES solvers [50] because experimental testing has difficulties in gathering reliable data in turbulent regions and transition areas. These errors are most commonly attributed to Reynolds number corrections, velocities as well as blockage due to set up which lead to misleading scaling effects. Another option that is sometimes utilized is a self supporting system where the researcher conducts their own experiment and computational simulation for comparison[51].

Where a majority of current numerical simulations discussed are based on and verify prior experimental results, the opposite can also be true. Jovic and Driver’s experiments in the mid 1990s were conducted to validate previous simulations conducted by NASA Center for Turbulence Research in which they studied the Reynolds number effect on skin friction behind a backward-facing step [23, 24].

Through the use of CFD software, the aerodynamic designs of vehicles have improved significantly and continue to improve to meet the ever increasing governmental regulations and performance desires. With a continuing reliance on CFD to simulate fluid flows, more traditional and time consuming experimental simulations are rarely used. As the CFD methods are becoming more and more powerful and dependable every year, there becomes less experimental verification for a majority of the results that are attained. If a computational result generally agrees with an old experimental result, they are declared valid, even if some or all of the initial conditions are unknown. According to Oberkampf and Barone, an additional issue is that a majority of the published experimental data does not specify all of the initial conditions and rarely published the uncertainty associated with the results [52]. The experiments must be



Figure 2.3: Commercially available ELD model 504 ducted water tunnel [57]

reproducible in order for them to be legitimately used to validate the computation models [53].

2.2 Water channel

There are predominately two types of experimental simulations commonly used for sub-scale through full-scale ground testing. Those two apparatuses are the wind tunnel and water tunnel. Water channels can be used to gather data about the flow and are typically better suited than wind tunnels for providing visual representations of the flow [25]. Numerous researchers have used water channels as the equipment of choice in observing three dimensional flow phenomena [3, 9, 12, 21, 25, 54–56]. The visualization can be done in a number of ways to include dye injection and bubble visualization, but is typically conducted by adding reflective particles into the water and using PIV or high speed photography [9]. Water tunnels can also be used to gather other types of data, such as pressure data, but it involves an additional layer of complication.

There are basically two styles of water channels, a constant cross section recirculating water channel and ducted return. In a commercially available ducted return



Figure 2.4: UNC Charlotte water channel during initial build

style of water channel, the water flows through the test section and then is pulled into a pipe which channels the flow under the test section into a centrifugal pump and is pumped back into the channel prior to re-entering the test section. Figure 2.3 shows a commercially available ducted water channel[57].

The constant cross section channels are similar to a closed return wind tunnel. The UNC Charlotte water channel is a constant cross section channel that was built in 2006 and is shown in Figure 2.4. Constant cross section channels are built in a variety of sizes, from a 15 *cm* cross sectional area [58] to the $1m^2$ cross section of the UNC Charlotte channel [59]. As can be seen when comparing Figure 2.3 and Figure 2.4, the constant cross section channel is larger and requires more space, but is cheaper to design and typically more efficient than the commercially available ducted water channels [59].

2.3 Wind tunnel

A small scale wind tunnel is the most reliable and cost effective method to conduct most flow experiments. Through the use of current technologies such as additive manufacturing and PIV to monitor the velocities around the body as well as more accurate sensors, the wind tunnel can provide updated and reliable experimental results.

Wind tunnels, like water channels are utilized to gather experimental aerodynamic data around a wide variety of objects. Wind tunnels are characterized by the type

of air return system they utilize, either open or closed [60]. In a wind tunnel, the air is passed over the model either by blowing or sucking. Sub-scale, open return, suction wind tunnels are the most accessible and cost effective method of gathering experimental data relatively quickly. Figure 2.5 shows a commercially available open return wind tunnel and Figure 2.6 shows a commercially available closed return wind tunnel. The types of tunnels used, have some effect on the types and amounts of data that can be collected, either from space available, or the flow conditioning possible.



Figure 2.5: Commercially available Aerolab open return educational windtunnel [61]

Open return wind tunnels, either suction high speed [5, 9–11, 13, 20, 62], or low speed [6–8, 11–19, 22–24, 63–65] are predominately used by most researchers for a variety of reasons. Some of the main advantages include low construction cost, good for propulsion and smoke visualization and no build up of particulates inside the tunnel that could alter the results. Some of the disadvantages include increased power consumption because the fan must continually run, excessive noise and since the entrance is open, local temperature and atmospheric conditions can have an impact on the results.

The closed return wind tunnel is similar to the UNC Charlotte water channel in design and are also occasionally used [3, 66, 67]. Some of the advantages of a closed return wind tunnel include good flow quality in the turn section, quieter than an open return and lower operating costs. The lower cost are due to the fan only needing to

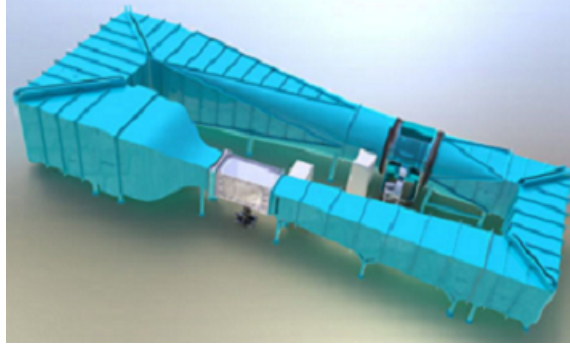


Figure 2.6: Commercially available Aerolab closed return wind tunnel [61]

recover losses incurred from flow along the wall and turning vanes. Some of the disadvantages of the closed return tunnel include higher construction cost, difficult to implement propulsion and smoke visualization and the requirement to evacuate exhaust and heat that builds up over the course of a test that may alter the results.

Besides the tunnels themselves, other variables and adaptations may be required to get more realistic results. One such variable is ground simulations. The two basic types of ground simulations in a wind tunnel are a fixed floor for models that do not have a rolling wheel component and the rolling road for those that do. Both types have pros and cons associated with their use. When an experiment requires the model to have wheels that are in contact with the ground, especially if there is a low ground clearance, the rolling road, although more costly to operate provides more reliable results due to ground effects in both sub-scale [15, 63, 68] and full scale testing [69–71].

Cooper made several advancements on the reliability of wind tunnels and the use of bluff bodies as vehicles. The work showed that the accuracy of the experiments depends entirely on how closely the actual conditions can be replicated in the wind tunnel, the accuracy of the model geometries and Reynolds number[72]. The first and largest obstacle to be addressed is the correction factor, if it is required and how it is found to compensate for differences in scale, cross winds, boundary layer effects and Reynolds number effects. Cooper also determined that the Reynolds number in

the flow around the model does not need to be exactly the same as the real world Reynolds number. In fact, it only needs to be high enough to cause boundary layers at the front face of the model that become turbulent before the flow reaches the edges. This may require the flow to be "tripped" before reaching the model.

Another variable to be considered in wind tunnel testing is the blockage ratio. The blockage ratio is the ratio of the total frontal area of the model to the cross sectional area of the tunnel and expresses the amount of blockage of the free stream flow inside the test area. Typically, if the blockage ratio is higher than 5 %, some sort of correction will need to be applied to the results to make them accurate. Maskell used bluff body aircraft models to develop a theory on blockage in closed wind tunnels and how to correct for the wake blockage behind the wings [73]. Based on these early results, Gould advanced the topic more and established a set of procedures and parameters to make corrections in a closed tunnel for rectangular plates[74], which were key to bluff body and streamline vehicle experimentation. Couch advanced the line of research into transonic region near Mach 1 to study how the blockage ratio effected the results and determined that significant corrections were required at these speeds despite low blockage ratios that would not effect results at lower speeds [75].

2.4 Molecular Hydrodynamics

The flow of non liquid materials are important in a wide range of applications. Two such applications are vibratory polishing[76–78] in manufacturing and geophysical studies to predict mud slides. Other studies into the mixing and segregation of the media has advanced the study of the flow dynamics of the granular media [79].

There are numerous parameters which control the final surface finish and are being studied, such as the type of vibratory system, the type, shape and size of the media used in the process as well as the amount of time the component is polished. Unfortunately, it is difficult to predict the amount of time it will take to get the desired surface

finish due to relatively few empirical models that can accurately predict the material removal rate. The difficulty lies in the lack of ability to gather good experimental data that describe the fundamentals, such as media speed and trajectories[77].

The study of vibrated systems in vibratory polishing is providing experimental results, which when analyzed can be used to develop more robust computational models based on given experimental parameters. These parameters and experimental results can then be used in numerical simulations to give rough surface predictions[76, 80], material removal rates[76, 80] and determine the intensity of the interactions between the work piece and the media [78]. The data captured in vibratory experiments are most often the vibrational frequency, workpiece speed (if present), time, impact velocities[81–83], contact forces[84] and recently media velocity with PIV systems[77, 85] and turbulence spectra[86]. This data can be used to further characterize the finishing media by determining the effective kinematic and dynamic viscosity of the fluidized granular media.

Molecular hydrodynamics is the study of the forces acting on or exerted on molecules in fluids. As a fluid, or system of molecules is disturbed, the disturbances are dissipated by diffusion, viscous forces and thermal conduction[87]. There are several methods to study these hydrodynamics systems, including molecular dynamic (MD) simulations[88, 89], inelastic neutron scattering[90] and light scattering[87, 91], all of which have pros and cons.

Molecular dynamic simulations are computer simulations which are used to study the movements and interactions of molecules over a limited amount of time. The limitations of this method are primarily concerned with time and space. The longer a simulation runs, the more cumulative errors that appear, which can be minimized with proper assumptions and algorithms, but not removed. The larger the test volume desired, the more molecules are required to fill that space resulting in excessive computational cost. Additionally, the programs tend to rely on approximate inter-

particle potentials and periodic boundary conditions. Despite these limitations, MD has been utilized to describe a granular media system as thermodynamics states at rest, dependent on only a single variable[92].

Inelastic neutron scattering is an experimental technique which uses a neutron beam fired into a sample to study molecular movements and interactions. This technique requires the ability to monitor and analyze the energy of the scattered neutrons at some fixed angle from the neutron beam. The largest drawback to this method is the accessibility of the neutron beam sources[90].

Light scattering techniques are similar to the inelastic neutron scattering in that the polarized light is focused on an interrogation volume containing the liquid being studied. The light is then scattered by the molecules and detected at a fixed angle relative to the light source[85]. This method requires some sort of light filtering or mixing during the detection and analysis of the scattered light[93]. This method is also very time and space limited.

The basic hypothesis of macroscopic continuum fluid dynamics and micro-scale molecular hydrodynamics assumes that local thermodynamic equilibrium occurs on the length and time scales that are large relative to the molecular diameters and collision times but small relative to continuum scales[85]. In the Navier-Stokes equations, local thermodynamic equilibrium is required[94] in order to set basically non-equilibrium continuum scale flow and energy features to strictly equilibrium thermodynamic properties (temperature and internal energy). Other micro-scale non-equilibrium processes are assumed to represent only minor separations from the local thermodynamic equilibrium[94].

The granular media used in the vibrating systems, when subjected to the external forces of the system will function or move in a statistical fashion[95]. This statistical motion occurs because of the individual pieces' shape, size and contacts[95]. Vibrated grain piles as described earlier can be used to investigate molecular hydrodynamic

processes with an understanding of elements of equilibrium and non-equilibrium statistical mechanics and four measurements[85, 96]. Those measurements include:

- i) The vibration spectra of the vibratory system, with media absent and present
- ii) Individual grain dynamics attained through the single particle velocity
- iii) Effective grain viscosities
- iv) Time-average and long-time flow surface velocity fields

To study any of these processes or elements using grain piles, it is assumed that energy will be constantly applied to the system or the system will fall dormant due to its dissipative nature[95].

One such study using granular media flows to study molecular liquids was conducted by Abdelrahman[86]. Abdelrahman showed that the turbulence spectra of the vibrated grain piles flow displayed similar energy dissipation and vortex breakdown observed in turbulent flow liquids.

Keanini *et al* has used the vibrated grain piles for visualization and as an analog method of studying hydrodynamic processes[96]. The first results showed that vibrated grain piles could theoretically serve as experimentally-accessible analogs for studying liquid-state molecular hydrodynamic processes. Additional results showed that it was possible to measure and analyze the effective viscosity of the grain systems to gain deeper understanding into origins of kinematic viscosity in diatomic liquids as well as monatomic liquids.

2.5 Particle Image Velocimetry

Since the wake region and near wall regions around any experimental model are highly sensitive to intrusion, new methods were needed that did not disrupt the flow while gathering valuable data. In the late 1970s, PIV grew out of previous flow visualization techniques such as Laser Doppler Velocimetry (LDV) and was developed as a more robust, non-intrusive method of measuring flow field properties, turbulent

regions, vortices and other structures that develop in the flow field. Through the use of PIV/ DPIV and high speed photographic equipment, visual data can be gathered and analyzed, quickly and easily, to determine quantities like velocity. PIV provides some information, such as instantaneous images of flow structures used to understand unsteady motion, which is very difficult to gather using LDV[97].

PIV has progressed since these early days of LDV which acquired a flow velocity at a particular point into the early PIV systems that were able to produce 2D flow fields. As the processes improved, some researchers spent years studying ways to improve laser-enhanced visualization methods such as seeding types, model preparation, enhancing photography and laser capabilities [55]. A typical 2D PIV system consists of a single camera and can produce a 2D (2 spatial dimensions) and 2C (2 component) velocity measurement[98]. The systems continued to improve and increase capabilities into Stereoscopic PIV (SPIV) [66, 99–101], Microscopic PIV (MicroPIV)[102] and on to more current methods such as Tomographic PIV (TomoPIV) [1, 56, 100, 101, 103–110]. Each method has a variety of capabilities and combinations of determinable dimension components from early 2D-2C to 2D-3C DPIV by Sousa[111] and 3D-3C as outlined later in this section. Individual systems also vary depending on cost and desired capabilities. Some use a single plenoptic camera to gather volumetric PIV data [112] to the more complex three camera[99, 105] and four camera systems[1, 103]. Through improvements in both the PIV systems and photographic capabilities, PIV, when properly equipped, can be used to visualize and analyze flows down to the micron level [102].

Current PIV systems operate by providing velocity vector measurements in an established cross-section of a flow in a wind tunnel or water tunnel. For PIV, a single camera captures two velocity components and presents a two dimensional field. SPIV utilizes two cameras to measure two velocity components and produce a small three dimensional field. TomoPIV uses three or more cameras to measure three

velocity components[113] and produce a three dimensional volume. Because of the high resolution and high speed photography, multiple exposures are used to determine how a particle moves through the test section and the correlation of different size areas of interest can be optimized in terms of accuracy and reliability [114]. With the flow uniformly seeded with appropriate reflective seeding, the laser is pulsed twice, which illuminates the test area. The cameras gather images timed with the laser pulses in which the reflections off of the seeding particles are visible. The two images are then broken into interrogation areas, which are correlated with each other to identify each particle position. The two images are then compared with each other to identify the displacement from the first image to the second in the pair and also the velocity[113]. This process is repeated for each image pair take during the test. The images, once analyzed give both the velocity and the direction which makes it an immensely powerful tool when studying the wake region behind flows [115]. The time step (Δt) between the double images is very important to ensure all motion within the test area is captured and there is not a loss of pairs due to out of plane motion [116–118]. Advances in PIV systems allow for not only classical averaged results, but also time-resolved vector maps.

2.5.1 Flow Seeding

PIV is dependent on the light scattering capabilities inside the flow. Various methods to include vapor screen, injected florescent dyes, and embedded particulates are available for use and are typically dependent on the type of flow and flow medium as well as the parameters to be recorded. The flow seeding must encompass the entire measurement area and should be uniform[119]. To acquire data on small flow structures, the flow must be highly seeded to provide good spatial resolution[120]. In order for the seeding to be reliable, it should be neutrally buoyant in the flow medium and thus follow the natural flow of the fluid.

When utilizing a wind tunnel, a vapor screen consisting of smoke, olive oil or some other neutrally buoyant particulate, which is ionized and introduced or directly introduced into the flow prior to the model is often used. This type of seeding requires constant addition into the test section in uniform amounts in order to be reliable. Although smoke is the easiest to utilize and most readily available, the small particles and large concentrations make it nearly impossible to follow individual particles[121]. The PIV system instead finds locations of local gray scale variations and tracks those variations inside the vapor screen. Olive oil particles, like the smoke, tend to be around $1\text{ }\mu\text{m}$ but can be adjusted to larger sizes based on the equipment used to produce the mist.

Helium filled soap bubbles provide a much larger particle size (from sub-millimeter to approximately 5 mm) and can be used for slower flows utilizing PIV[121, 122]. Kerho and Bragg noted a few known problems with the helium filled soap bubble method is that the diameter of the particles may fluctuate and not be buoyant in the flow and thus react slower than the flow and the seeding density is sparse and may be difficult to get multiple particles inside a single image[121]. In 2015, Scarano *et al.* stated that if careful consideration taken for the soap and helium volume flow rates and injection process, bubbles of approximately 300 microns could be produced and accurately follow the flow patterns in $30\text{ }\frac{\text{m}}{\text{sec}}$ flow[122] in wind tunnels. If the bubbles were denser than the surrounding air, they were slow to track the changes in the stream. When the bubbles were smaller, or lighter than air they anticipated flow changes. The primary drawback to the helium bubbles was the low seeding production rates of the generators, resulting in low seed density rates inside the test volume. Additionally they were able to increase the test area volume size in their time resolved TomoPIV experiments utilizing the helium filled bubbles, but still had problems with getting more than 1 particle/ mm^3 [122].

For water channel experiments, numerous variations of the injected dye or embed-

ded particulates are possible. Injected florescent dyes that are added either through ports in the model, or upstream from the model. Care must be taken in adding the dye so that there is enough to reflect the laser light, but not so much as to make the test chamber cloudy[55]. As a test progresses and more die is added to the flow, the tunnel will become saturated and will require the tunnel to be drained and cleaned. Embedded particulates can also be added in a known concentration into the water channel. Once circulated, the test section will have a uniform distribution through the test[1]. This is the simplest method of seeding and is the easiest to maintain.

2.5.2 Tomographic Particle Image Velocimetry

TomoPIV was originally developed in 2006 by Elsigna to produce a 3D measurement volume with PIV[106] and capable of studying unsteady three dimensional flows[123]. This was especially important to capture flows that do not exhibit symmetry which previously required numerous planar methods to visualize[106]. The technique typically uses multiple cameras (3-6) to record simultaneous images from different angles of the same volume[124]. These images are used to reconstruct three dimensional light intensity fields, which are then analyzed using a three dimensional correlation program to build a three dimensional, three component velocity field inside the volume. As technology continues to increase, camera cost decreases while their resolution and speed improve, leading to more common application of volumetric methods. Some of the more current imaging systems can capture PIV data on the order of 10,000 frames per second (fps) at a resolution of over 1 megapixel[65]. As the system processes improve, derived quantities such as acceleration, deformation and pressure for moderate Reynolds flows may be calculated without use of approximations [125]. One drawback to TomoPIV is that it is limited by the number of particles that can be resolved [126]. A second limiting factor is the imaging frequency and resolution as well as laser frequencies. Even at 10,000 fps, many complicated

flows, even at low velocities require frame rates and laser frequencies on the order of 100,000 per second[65]. It has also been determined that the tomographic reconstructions often contain "ghost" particles, or false light intensity readings[107]. Although some experiments have determined that the ghost particles have little effect on the accuracy of the vector fields produced[107], others show that under certain circumstances, they can add a significant velocity error, specifically around the edge of the test volume[110]. Additional work and methods on experimental set up to minimize or remove ghost particles has been conducted by Elsinga *et al*[108, 110].

Even with the drawbacks, time-resolved PIV is utilized to conduct turbulence research[103, 127]. It has been determined that by limiting the test volume, the acquisition frequency can be increased and produce time-resolved velocity measurements [65]. An additional benefit of TomoPIV is it can produce results at higher seeding densities[107] and finer spatial resolution[110].

TomoPIV originally used a minimum line Of sight (MinLOS) and/or multiplicative algebraic reconstruction technique (MART) to carry out the voxel reconstruction[106] which were extremely computationally expensive and required hours or days to reconstruct the voxel space[128]. The voxel is a 3D expansion of a pixel with respect to the data[125]. The system was improved to a simultaneous multiplicative algebraic reconstruction technique (SMART) which takes less time to carry out the reconstruction[128]. All PIV systems require some given experimental parameters to include calibration, setup and timing in order to produce reliable results.

The process uses a pixel by pixel reconstruction and looks for light intensity values instead of individual particles. The velocity data is based on the spatial averaging of the reconstructed measurements, which can lead to biases in flow with strong velocity gradients[120]. Then 3D Least Squares Matching (LSM) is utilized to process the data to determine velocity fields. LSM, when extended into 3D matches two cuboids (3D version of a rectangle) and compares the differences between the two

to determine velocity of the flow[129]. This processing method uses scale, shear and rotation parameters that are not accounted for in other 3D correlation methods [130]. To accomplish this, the program iteratively shifts, rotates, stretches and shears the voxel space until the first image in the image pair matches the second image of the pair[130]. This allows for a higher voxel precision and reliability in fewer iterations, typically reducing computation time compared to other methods.

2.5.3 Particle Image Velocimetry Uncertainty

Like all processes, PIV is susceptible to errors and those errors are dependent on both time and location within the vector field. The two categories of common errors are random (precision) and systematic (accuracy) [98]. A large amount of work has gone into determining sources of errors and how to determine the uncertainty associated with those errors[98, 131–134]. Below is a list of possible errors associated with PIV in general [98] and can be applied to TomoPIV specifically, which can be minimized by proper experimental set up. These include:

- i) Errors associated with timing and synchronization between laser pulses and cameras
- ii) Light sheet misalignment in test volume
- iii) Inaccurate calibration target
- iv) Inaccurate calibration process
- v) Errors due to camera(s) field of view
- vi) Errors due to refraction between air and water
- vii) Improper seeding size or density for fluid or required response time

Wieneke also outlined other possible sources of PIV error which should be part of the uncertainty calculation[98, 131], which include:

- i) Camera noise (background, dark and photon shot) ii) PIV processing scheme

- iii) Variations in illumination intensity between laser pulses
- iv) Particle size and shape should be near 2 pixel, where larger and smaller size lead to different types of errors which are difficult to determine with TomoPIV[98]
- v) Particle out of plane motion errors due to particles moving out of the illumination area

There are several PIV uncertainty and error correction methods proposed in literature. Since PIV results are dependent on the processing algorithm, an accurate uncertainty estimate must be processing algorithm based[134]. None of the methods are directly applicable to TomoPIV. One low cost, minimal time method of determining uncertainty is the "peak ratio" method which was developed by Charonko and Vlachos[132]. This method is a ratio of the largest correlation peak to the second largest correlation peak. This method does not, however, provide any information on the source of the errors or how to correct those errors[134] and it does not apply to LSM. This method, unlike other methods can be used regardless of flow condition or image quality[132]. Another method that was recently introduced by Sciacchitano was the image matching method which is based on super resolution[135].

2.5.4 Non-Traditional Uses of Particle Image Velocimetry

PIV has also been used to measure the velocity field of more non traditional mediums such as vibrated grain piles or granular flows. It has been used to measure free surface velocities and basal boundary in a granular flows such as those in shaken containers,[77, 85, 136] and tumblers[79]. To use PIV in the nontransparent media, certain modifications need to be taken in the data acquisition, or processing or both. The largest difference is the lack of need for foreign material to be added to the flow for tracking. Lueptow utilized a strobe light to illuminate the test area and processed the PIV using the different colors of the grains in place of seeding [136]. Others have

used high intensity lights and high speed cameras to record the flow and then process the PIV based on dark or light spots on the individual media pieces [76, 77, 80, 85].

As a final note on PIV, for this work, the specifics of what the PIV software does will be viewed as a black box with out going into details of what the system is doing. Required inputs by the user will be outlined as briefly explained.

CHAPTER 3: STUDY OF TURBULENT STRUCTURES UTILIZING PARTICLE IMAGE VELOCIMETRY IN A HYDRODYNAMIC WATER CHANNEL

To generate reliable volumetric velocity data near and in the wake of a bluff body, the UNCC hydrodynamic water channel and Stereoscopic Particle Image Velocimetry (SPIV) were upgraded. The first portion of this study required the SPIV upgraded to a four camera Tomographic Particle Image Velocimetry (TomoPIV) system, which was the one of only a handful of diagnostic tools available for instantaneously measuring velocities in three spatial dimensions. The data from empty channel tests were used to improve the uniformity of the flow in the channel and preliminary bluff body tests generated data used to improve TomoPIV processing methods.

The results of the final TomoPIV study of the flow around a bluff body provided volumetric data about the flow structures around a cube which were identified and compared to the historic benchmark schematic presented by Martinuzzi and Tropea of flow around a wall-mounted cube. The results provide detailed, numerical data of the velocities inside the volume near and in the wake of the bluff body not previously possible which can be used to validate computational models and expand aerodynamic studies.

3.1 Water Channel

The facility recirculating water channel, as seen in Figure 3.1, is installed in the University of North Carolina at Charlotte (UNCC) Graduate Motor Sports Research Lab (MSR). The channel has undergone numerous upgrades as seen in Figure 3.2.



Figure 3.1: Side view of water channel as photographed during move and assembly by Dr. Samuel Hellman [59]

These upgrades include the installation of a mezzanine to allow researchers to safely access the top of the channel and overhead crane to assist with the insertion of experimental models. The channel has a 1 m^2 by 3 m long test section and a maximum flow velocity of $1\frac{\text{m}}{\text{sec}}$ [59]. The test section of the water channel has a constant cross section and is capable of achieving flow velocities between $0.1\frac{\text{m}}{\text{sec}}$ and $1\frac{\text{m}}{\text{sec}}$. The closed tunnel design with submerged pump has several advantages over other designs. Experimental variables such as seed density may be assumed to be constant once the channel reaches steady state velocity, which reduces the need and cost of constant particulate addition required in other designs. Additionally the design minimizes heat being added to the system by the pump since it is submerged. The test section is situated in such a way that the test model or test rigging are lowered from the top and suspended in the flow from a traverse mechanism which allows for controlled movement ($\pm 0.01\text{mm}$).



Figure 3.2: Top view of water channel with overhead crane and mezzanine installed.

3.2 Tomographic PIV

To increase the flow visualization capability in the UNCC MSR Lab water channel, the existing Stereoscopic PIV (SPIV) system was updated to a TomoPIV system. The completed TomoPIV experimental system used in this study is one of only a few of its type in operation in the United States. Measurements obtained can provide microsecond time-scale and micron length-scale resolution of boundary layer structural and dynamic features. TomoPIV represents one of only a few diagnostic tools available for instantaneously measuring velocities within three-dimensional flow fields. The output consists of the measured three-dimensional velocity field (three components (3C)) within a three dimensional interrogation volume (3D), classifying TomoPIV output as 3D-3C. This approach can be contrasted with previous techniques such as SPIV, which is often referred to as 3D but is actually 2D-3C. When combined with LSM, this 3D-3C system has the ability to directly provide all nine terms of the velocity gradient tensor[126]. Due to its ability to capture velocity fields within interrogated volumes, the TomoPIV can be used to efficiently measure near-surface

turbulent boundary layers over a wide range of curved-surface artifacts, under a wide range of free stream Reynolds numbers. One advantage of visualizing the flow with TomoPIV is the wake motions can be seen as a function of time based on the time scale of the image capture [1].

3.2.1 Cameras

To carry out the 3D-3C measurements, 4 FlowSense EO 4M dual-framing CCD cameras are used to image a flow field seeded with small particles and illuminated by laser light as seen schematically in Figure 3.3. Each camera is equipped with a Nikon 60 *mm* lens and a 532 *nm* narrow band pass filter. The cameras are configured asymmetrically with one camera centered on the center plane of the model, normal to the direction of the flow with each camera off set by 15, 30 and 45 degrees from the normal as seen in Figure 3.4. All of the cameras are mounted on the same horizontal plane. The 2D pixel images from each of the four cameras are used to reconstruct a 3D voxel space which shows the location, in 3D space, for all of the particles in the flow. These 3D voxel spaces are then processed as with traditional PIV systems to generate velocity vector maps. A number of error minimization techniques are incorporated in the TomoPIV system.

Light travels in a straight line and only changes direction and speed as it enters a medium with a different density. The new TomoPIV system utilizes four cameras imaging the same region through both air and water at different angles. To compensate for the errors associated with the refraction caused by passing through air and water, a prism tank was designed as seen in Figure 3.5 and filled with water. The cameras are positioned so that the lenses' viewing axis are perpendicular to the wall of the tank and imaging straight into the water. The angles of the tank walls match the desired angles of the imaging axes, thus minimizing the refraction errors.

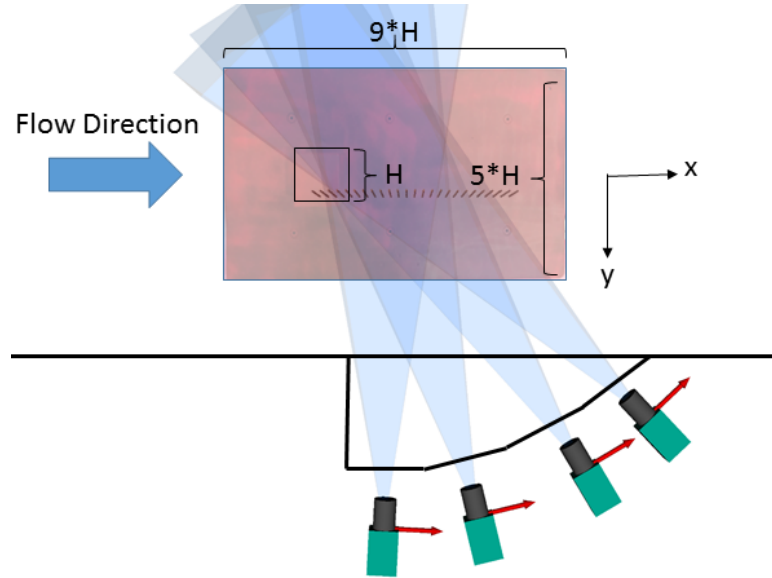


Figure 3.3: Schematic of the tomographic PIV camera set up and test area

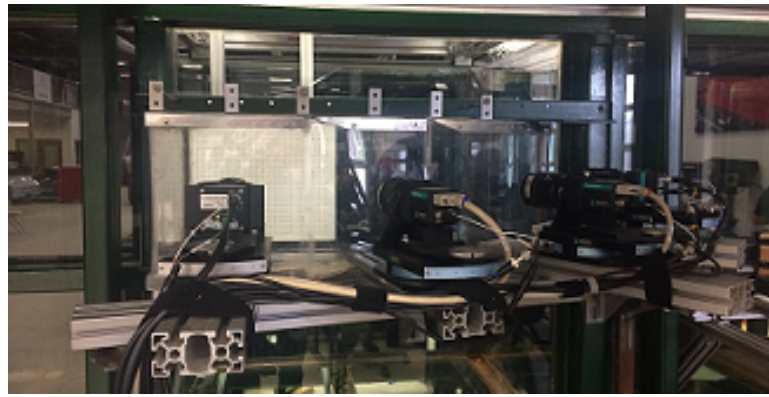


Figure 3.4: Side view of tomographic PIV camera set up and test area

3.2.2 Laser

The laser used in the water channel is a Nano L200-15 Class IV Litron, dual cavity, Nd:YAG, 532 nm wavelength with a pulse capability of 200 mJ per pulse and a pulse width of 4 ns . The laser volume is formed using a Dantec 5:1 tophat volumetric illumination optics.

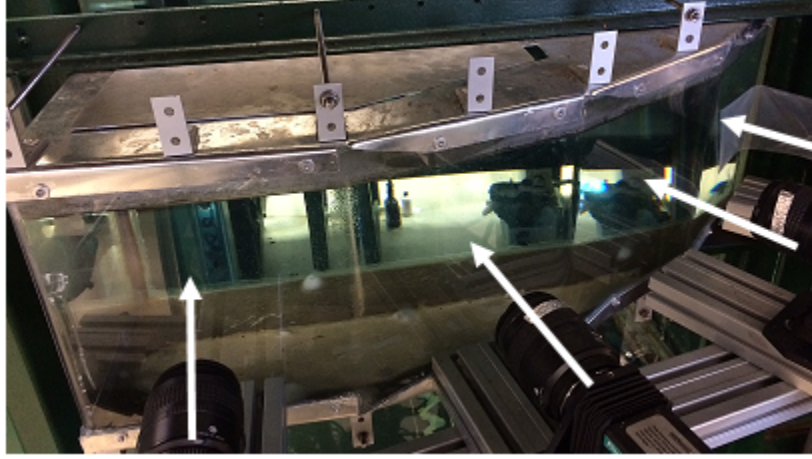


Figure 3.5: Prism tank installed on side of water channel with arrows depicting the matching camera and wall angles

3.2.3 Calibration

For the system to build a relationship between the image captured and the location of the volume, it must be calibrated. Each camera records an image at numerous positions in the volume, which is used by the system to triangulate the position of each particle in each image during reconstruction. The volumetric calibration can be done either manually or automatically. A $450\text{ mm} \times 450\text{ mm}$ dotted calibration target was used for the calibration. The calibrated volume depth was set to 100 mm , or $\pm 50\text{ mm}$ from the center plane of the channel. To conduct the multi-camera calibration, the traverse was set at -50 mm from the center plane of the channel and a single image was taken by all four cameras. The software then moved the target $+5\text{ mm}$ and held that position for 30 seconds allowing the water to settle before it took the next set of images. The process repeated in $+5\text{ mm}$ steps until the traverse reached the $+50\text{ mm}$ position from the center plane. Once all of the images were acquired, a 3rd order polynomial process was conducted as described by Soloff *et al* [137]. Each experiment required a new calibration, all of which resulted in an average re-projection error of less than 0.4 as specified by Elsigna *et al* [106].

3.2.4 Seeding Particles

Two different size seeding particles were tested to determine which produced the best results for both TomoPIV processing and volume reconstruction size. The first, smaller particles were 10 μm silver coated hollow glass spheres. The second particles were PSP-50 (Polyamid Seeding Particles) which had a diameter of 50 μm . This larger size particle allows for a slightly larger test area and deeper depth of field than the smaller particles.

3.2.5 Model

To manufacture the model(s) quickly and repeatably, a 3-D printer was utilized. Despite the minor problems with material directional strength and finished dimensional tolerances[138], 3-D printing the model for small scale experimentation is still one of the most cost and time effective methods. With a small amount of post processing, such as light surface smoothing, can produce a model within acceptable tolerances[139]. It is not recommended to print models that require material strength in all directions, for structural testing, or in tunnels that will place significant stress on the model. From simple cubic shapes to more extensive complete scale model vehicles, 3-D printing can render a complete model in one step. The model for both the wind tunnel and water channel experiments were made out of acrylonitrile butadiene styrene (ABS) in the UNCC Mechanical Engineering additive manufacturing lab. The models were printed on the same date in the same run and measure 7.62 *cm* square. The cubes were both attached to flat polycarbonate plates as seen in Figure 3.6 and Figure 4.4A.

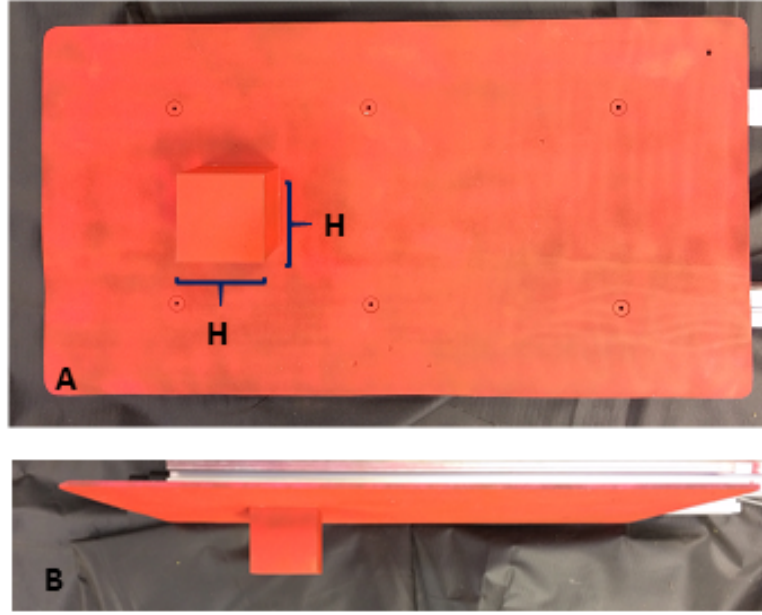


Figure 3.6: Image of cube mounted to flat plate A) from the top and B) from the side as mounted in the water channel

3.2.6 Model Reflectivity

The model described in the previous section was suspended from the top of the channel, 30 *cm* from the surface of the water. The cube was painted five times, with five different paints to determine which color provided the TomoPIV system greatest resolution and afforded the most detailed view of the wake region and inside the boundary layers.¹ This test was conducted to prove which surface preparation technique mitigated the surface reflections, which can affect the PIV systems capability to process accurate vector fields or even damage the cameras. There are numerous methods to mitigate the reflections with a typical 2D PIV system including camera placement and laser light intensity, but when utilizing TomoPIV the only method available is the surface preparation[100].

¹This section is a collaborative work with Tucker Bisel, Tony Martin, Spencer Owen, Peter Tkacik, Russel Keanini and Navid Goudarzi, UNC Charlotte, published in part in Biselet *et al* (2017) A Comparison of Flat White Aerosol and Rhodamine (R6G) Fluorescent Paints and Their Effect on the Results of Tomographic PIV Measurements, in the Proceedings of the International Mechanical Engineering Congress and Exposition (IMECE), IMECE Paper ID# 71507, Tampa, FL, November 2017

The first paint tested was an over the counter flat white aerosol paint. This paint, like the flat black, florescent pink and florescent orange, is low cost, commercially available and can be applied quickly. The flat white paint produced very intense surface reflections coming off of both the cube and the flat plate as seen in Figure 3.7. The gray value minimum observed by the camera was 137 with a maximum of 4095 and mean of 705. These reflections increased the background noise intensity and interfered with the PIV system's capability to recognize particles and limited the vector creation in the regions closest to the model and plate surface [140].

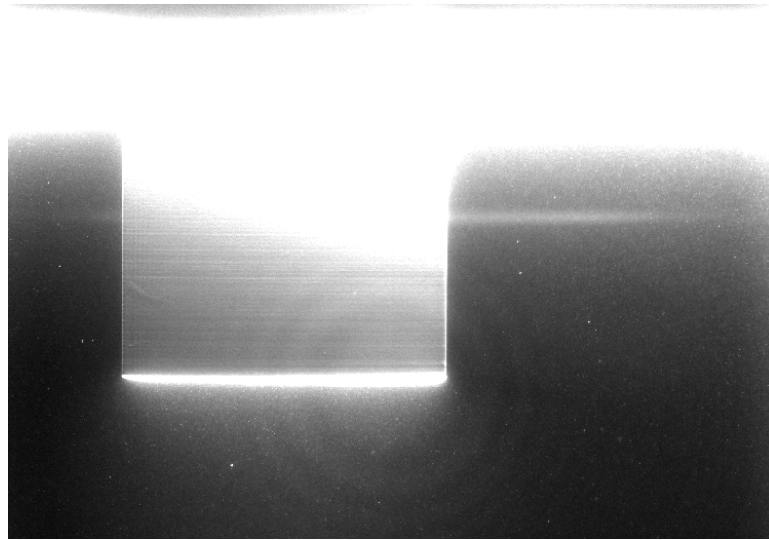


Figure 3.7: Image of cube painted flat white with over-saturation taken during color comparison test

The second paint tested was an over the counter flat black aerosol paint. The light intensity value minimum was 0 with a maximum of 1859 and mean of 34.7 as seen in Figure 3.8. The reflections were minimum and the black paint absorbed a majority of the light from its surroundings.

The third paint tested was an over the counter florescent orange aerosol paint used in conjunction with a low pass camera filter that blocks fluorescent light. The light intensity value minimum was 0 with a maximum of 3714 and mean of 52 as seen in Figure 3.9.

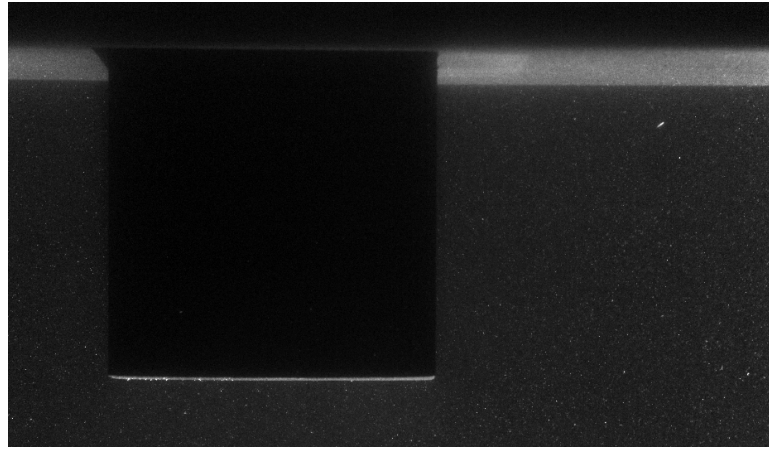


Figure 3.8: Image of cube painted flat black during color comparison test

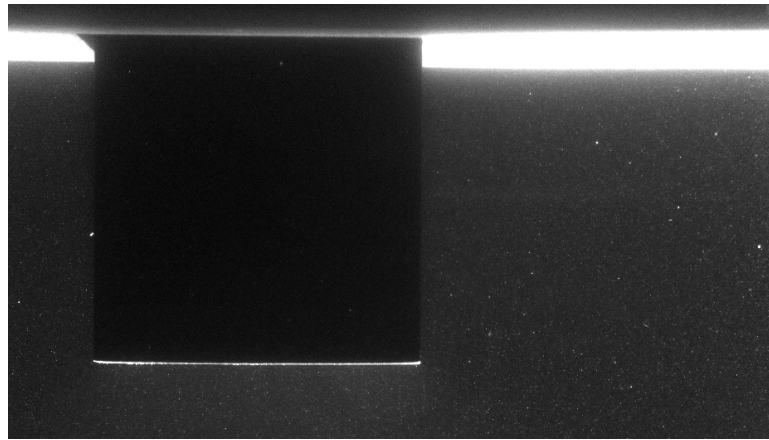


Figure 3.9: Image of cube painted florescent orange during color comparison test

The fourth paint tested was an over the counter florescent pink aerosol paint used in conjunction with a low pass camera filter that blocks fluorescent light. The light intensity value minimum was 0 with a maximum of 1509 and mean of 27 as seen in Figure 3.10.

The final paint type that was tested was Rhodamine 6G (R6G) from Flow Visualization Components, dr.gindele-fischer-nauwerek GBR used in conjunction with a low pass camera filter that blocks fluorescent light. This paint was highly recommended for its absorption characteristics, but has an extremely high cost of approximately \$400 per fluid ounce. Additionally, this paint breaks down over time and requires occasional re-coating. The R6G absorbs green light with a maximum absorption of

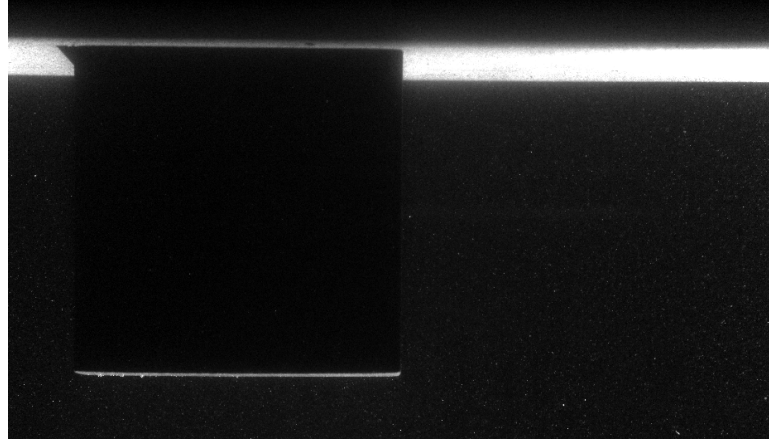


Figure 3.10: Image of cube painted florescent pink during color comparison test

540 nm, which shifts the spectrum to orange, which can be filtered out. The R6G was airbrushed onto the model and required several coats to ensure complete coverage. The R6G coated model had very low surface reflections as seen in Figure 3.11, resulting in high signal to noise ratio. The light intensity value minimum was 0 with a maximum of 3857 and mean of 718.5. This allowed the PIV system to recognize particles close to the surfaces and maximized vector creation throughout the volume [140].

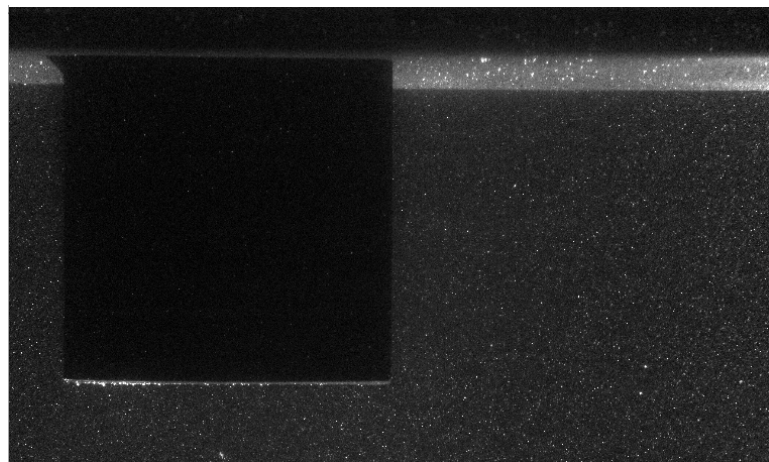


Figure 3.11: Image of cube painted with Rhodamine 6G taken during color comparison test

It was determined that the most suitable color to minimize surface reflections and produce the best overall results with the largest total volume was Rhodamine 6G

[140]. Commercially available florescent orange or pink paint was comparable with additional processing steps.

3.2.7 Data Processing

Each experiment was conducted for 25 seconds. The image acquisition frequency was set to 5 Hz (5 image pairs per second) for a total 125 images captured per experiment. The image acquisition and subsequent analysis was performed by Dantec Dynamics, Dynamic Studio. Dynamic Studios utilizes a Simultaneous Multiplicative Algebraic Reconstruction Technique (SMART) to execute the voxel reconstruction. The SMART reconstruction ran for 12 iterations to create the total volume. The spatial resolution and total voxel space created depended on the input parameters for each experiment. Dantecs 3D Least Squares Matching (LSM) technique was utilized to process vectors.

Other pre-processing methods are occasionally required, such as masking to remove non-realistic or ghost particles near the boundaries. To conduct a masking procedure, first, a mask must be defined in the software to cover the visible walls of the cube as well as the flat plate for each of the four cameras as seen in Figure 3.12A. The mask, when applied to each image, blacks out the unwanted area for each camera as seen in Figure 3.12B. The software then searches all of the images for the minimum intensity level at each pixel and creates an image with those values as seen in Figure 3.12C. This minimum value image is then subtracted out of each image in the original set to create a crisper particle image as seen in 3.12D. This process also increases the signal to noise ratio[1],

3.3 Water Channel Corrections for Non-Uniform Flow

During initial experimentation and data processing utilizing the TomoPIV system, it was determined that the flow through the test section of the water channel was not

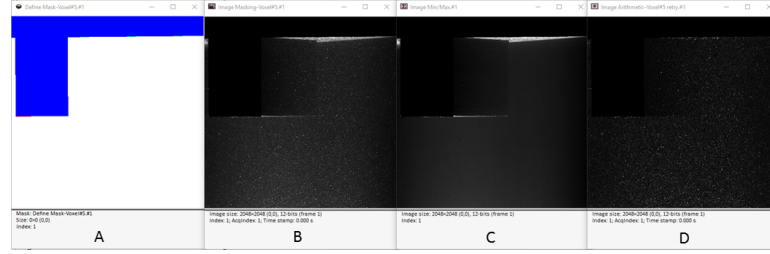


Figure 3.12: Voxel pre-processing steps; A) define mask, B) apply mask, C) background subtraction, D) image arithmetic. Image modified from Fleischhauer *et al.*[1]

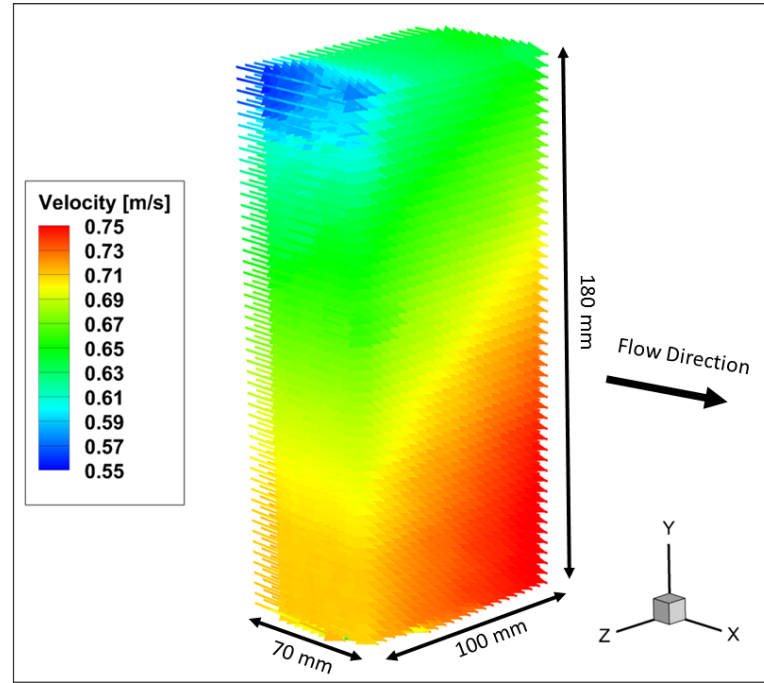


Figure 3.13: $180\text{ mm} \times 100\text{ mm} \times 70\text{ mm}$ processed vector field at motor frequency of 25 Hz showing non-uniform flow.

uniform as seen in Figure 3.13. Figure 3.13 shows a $180\text{ mm} \times 100\text{ mm} \times 70\text{ mm}$ processed vector field from the center of the test area of the empty water channel with the motor operating at 25 Hz. Figure 3.13 shows a difference in velocity of slightly larger than $0.2\frac{m}{sec}$ across the test section. Since this test area was in the center of the water channel it was expected to be nearly uniform.

Additional tests were conducted at 7.5 Hz, 10 Hz and 15 Hz showing that the non-uniformity was consistent across multiple motor velocities as seen in Figure 3.14.

Based on the TomoPIV results, the entire cross sectional area of the test section

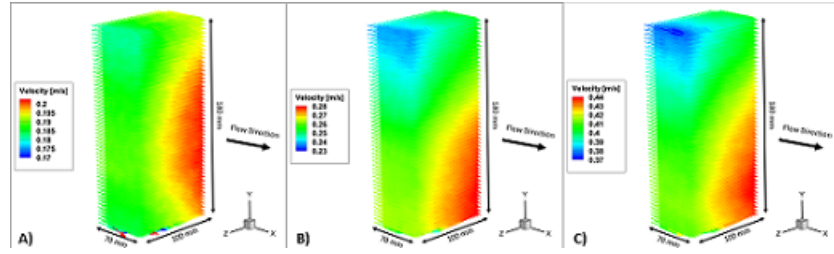


Figure 3.14: $180\text{ mm} \times 100\text{ mm} \times 70\text{ mm}$ processed vector field at motor frequency of A) 7.5 Hz, B) 10 Hz and C) 15 Hz showing non-uniform flow.

was measured using a Vernier LabQuest hand held flow rate sensor which was capable of $0.0012 \pm 1\% \frac{m}{sec}$ resolution. An 18×18 grid was laid out across the width and depth of the channel with a δx and δz of 0.05 m . The water channel motor frequency set at 15 Hz and measurements were taken in 30 seconds intervals, three measurements per position and averaged. Each set of measurements resulted in a standard deviation of $0.008 \frac{m}{sec}$. Figure 3.15 shows the flow profile prior to any flow modification. This profile shows that the flow has a maximum velocity approximately 65 cm below the surface and 15 cm from the inside wall instead of in the center of the test area. It was also determined during this test that there was pulsing present in the test section.

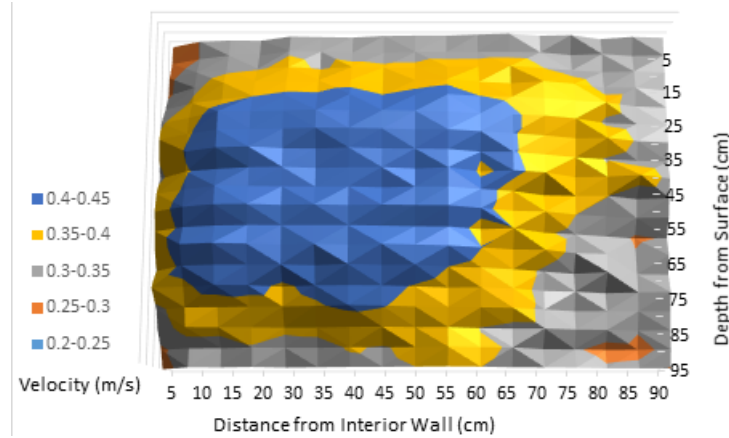


Figure 3.15: Velocity profile in the water channel test section prior to flow modification

Figure 3.15 shows the peak velocity for the entire channel to be $0.447 \frac{m}{sec}$ and the lowest velocity to be $0.270 \frac{m}{sec}$ which results in a 39.7% difference at a motor frequency

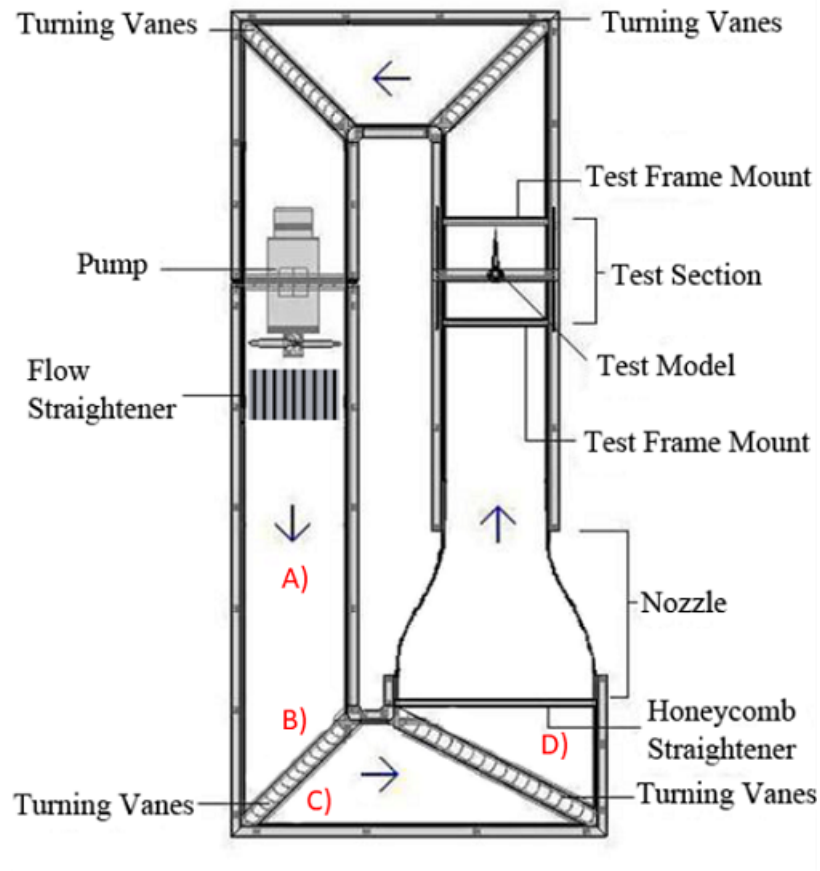


Figure 3.16: Schematic of water channel modified from Dr. Samuel Hellman's dissertation [59] demonstrating A) toroidal flow area, B) high speed flow area, C) recirculation area and D) recirculation area

of 15 Hz. Since no testing is conducted close to the walls or floor, the boundary layer results were discarded which left the same maximum velocity of $0.447 \frac{m}{sec}$ with a new minimum velocity of $0.321 \frac{m}{sec}$ which resulted in a 28.3% difference across the test area.

Using string and visual testing methods, various back flow regions were located, specifically inside the corners of the channel near the turning vanes. Additional testing revealed that the initial non-uniformity was due in part to the type of motor (which operates without a shroud). It was also determined that the motor was pulling air down into the water causing voids and fluctuations in the velocity at random intervals. When in close proximity to the motor (before the flow straightener) the flow is toroidal

with near zero velocities in the center of the motor and along the walls and floor. After the flow straightener and before the first turning vane as seen in Figure 3.16 area A) the flow continues in a toroidal shape with the center region of the tunnel picking up speed. As the flow enters into the first set of turning vanes (Figure 3.16 area B) flow speeds up along the inside wall while slowing down along the outside wall due to increased travel distance. This causes the flow to form a recirculation zone in the farthest corner (Figure 3.16 area C) where the flow goes in reverse back through the turning vanes. A similar scenario happens in the second set of turning vanes as seen in Figure 3.16 area D) prior to the honeycomb straightener and nozzle.

A $90\text{ cm} \times 120\text{ cm}$ piece of stainless steel mesh screen with 0.635 mm wire diameter screen and 44% blockage was attached to the first turning vane (Figure 3.16, area B), 10 cm in from the interior wall and 20 cm up from the floor of the channel to slow the flow through the center of the channel and create blockage forcing the flow to speed up along the outside of then channel. A second screen, $40\text{ cm} \times 42\text{ cm}$ was attached to the second turning vane, prior to the nozzle (Figure 3.16, area D), 30 cm in from the interior wall and 35 cm from the bottom of the channel.

The flow was then tested a second time using the TomoPIV system in the same location as the original test volume at 25 Hz, 15 Hz, 10 Hz and 5 Hz. Figure 3.17 shows the processed vector field at 25 Hz after the screens were installed.

Figure 3.18 shows the results of the 7.5 Hz, 10 Hz and 15 Hz showing that the non-uniformity remained and was consistent across multiple motor velocities after installation of screens.

Figure 3.19 shows a comparison of the initial test with the second test. The second test shows a 14% difference between maximum and minimum velocities compared to 27% difference in velocity observed during the initial test, which is 48% improvement. It also shows a 15% reduction in speed from $0.75\frac{m}{sec}$ to $0.64\frac{m}{sec}$ at 25 Hz.

To decrease the 14% difference below the desired 10% difference and reduce the

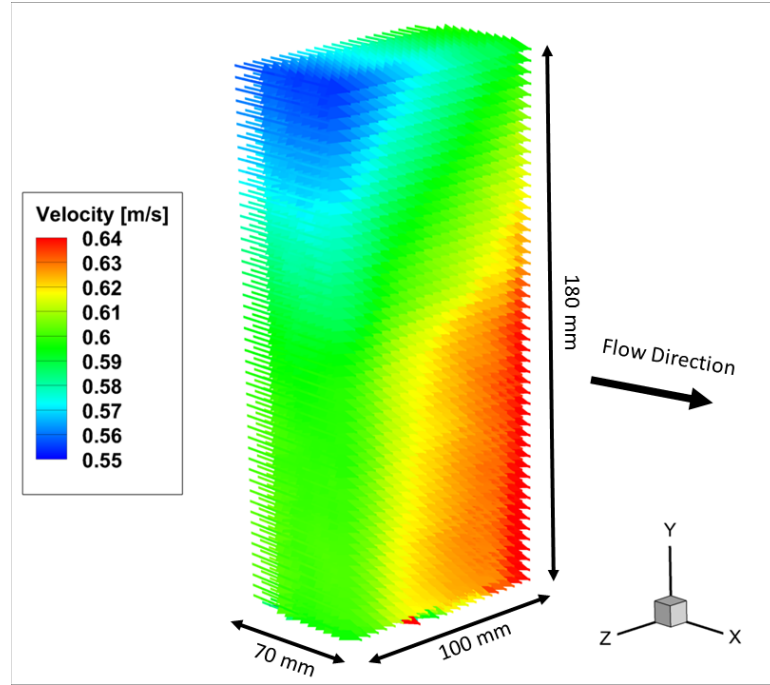


Figure 3.17: $180\text{ mm} \times 100\text{ mm} \times 70\text{ mm}$ processed vector field at motor frequency of 25 Hz after screen initial installation

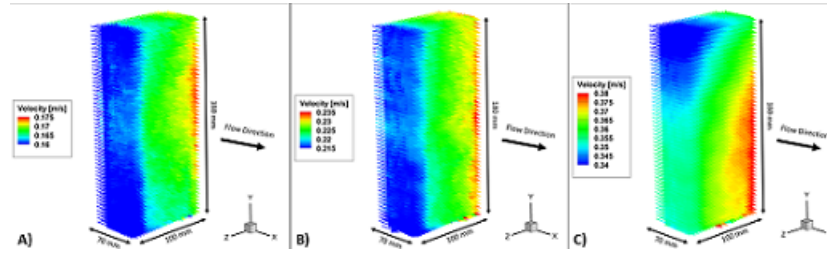


Figure 3.18: $180\text{ mm} \times 100\text{ mm} \times 70\text{ mm}$ processed vector field at motor frequency of A) 7.5 Hz, B) 10 Hz and C) 15 Hz showing non-uniform flow with screens installed

pulsing, an anti-cavitation plate as seen in Figure 3.20 was installed over the motor to minimize the air pockets created by the propeller during operation. The anti-cavitation plate, which spans the width of the channel and is 60 *cm* long was suspended 8 *cm* below the surface of the water directly over the propeller.

The flow was tested a third time using the TomoPIV system in the same location as the original test volume at 25 Hz, 15 Hz, 10 Hz and 5 Hz. Figure 3.21 shows the processed vector field for 25 Hz after the anti-cavitation plate was installed.

Figure 3.22 shows a comparison of the initial test with the third test. The third

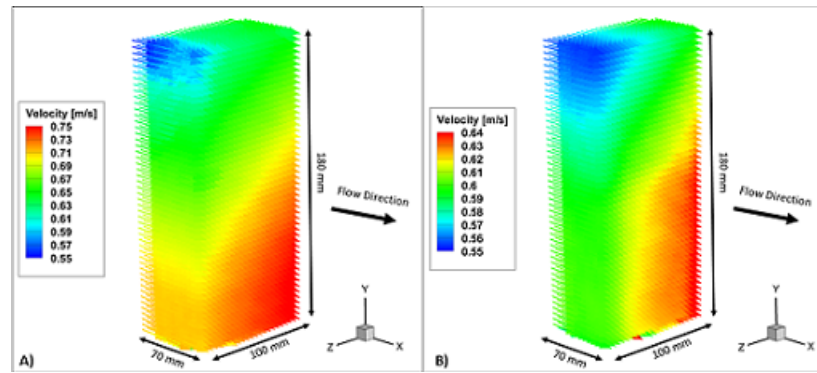


Figure 3.19: 180 mm × 100 mm × 70 mm processed vector field at motor frequency of 25 Hz of A) initial and B) post screen installation flow.

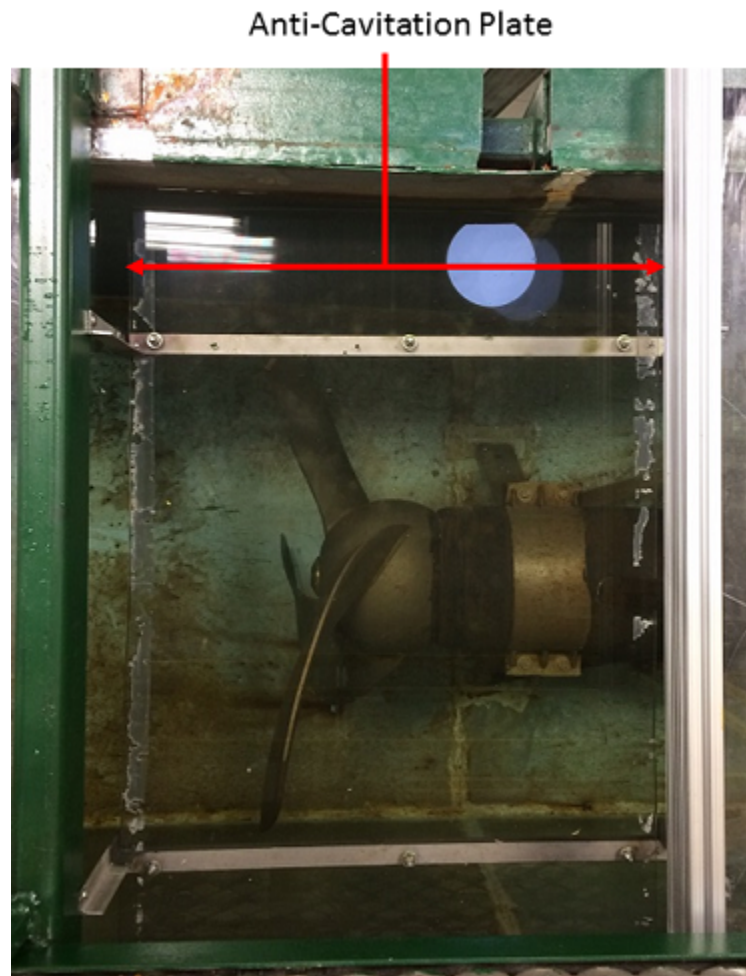


Figure 3.20: Anti-cavitation plate installed over water channel motor to reduce cavitation

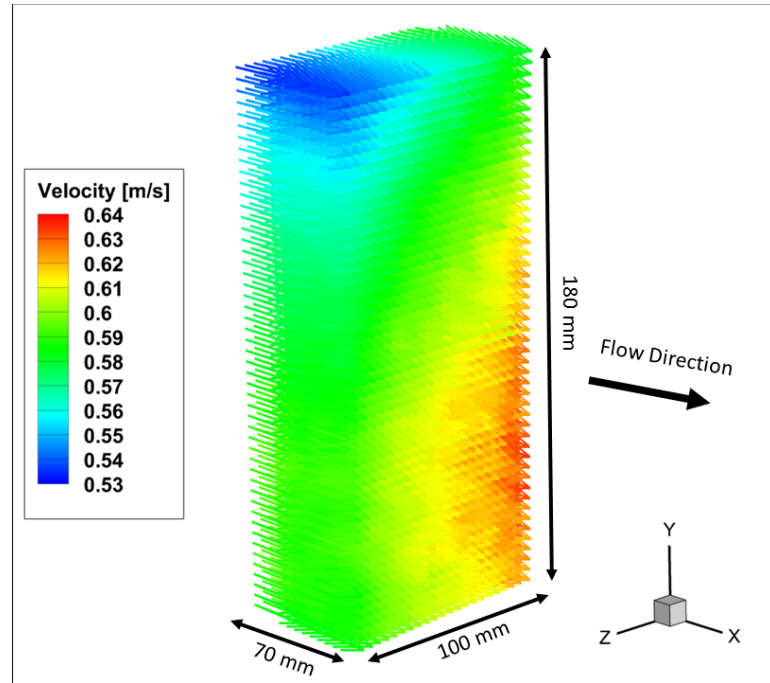


Figure 3.21: $180\text{ mm} \times 100\text{ mm} \times 70\text{ mm}$ processed vector field at motor frequency of 25 Hz after anti-cavitation plate was installed

test shows a 17% difference between maximum and minimum velocities compared to 27% difference in velocity observed during the initial test. The anti-cavitation plate smoothed out the flow considerably, but slightly increased the velocity differences between maximum and minimum.

The flow was re-tested with the hand held flow meter which showed reduced pulsing inside the test section and a velocity gradient that still increased across the

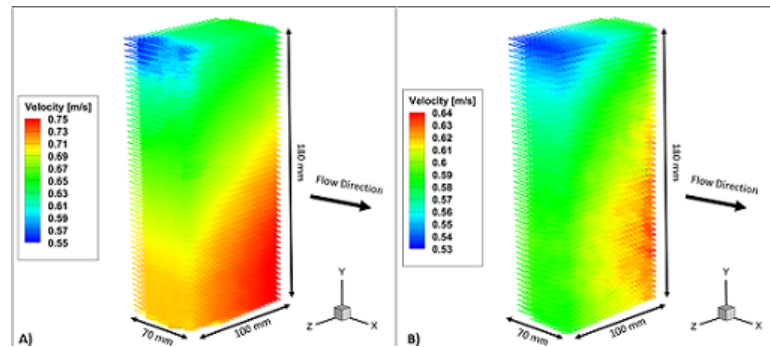


Figure 3.22: $180\text{ mm} \times 100\text{ mm} \times 70\text{ mm}$ processed vector field at motor frequency of 25 Hz comparison of the A) initial and B) third test

width of the test section from the outside wall to the inside wall. To minimize the pulsing, a full width screen was placed across the mouth of the nozzle between the honeycomb straightener and the test section. To even out the gradient, a second screen, 1/4 the width of the channel was secured along the inside wall of the channel behind the full width screen.

The flow was then tested a fourth time using the TomoPIV system in the same location as the original test volume at 25 Hz, 15 Hz, 10 Hz and 7.5 Hz. Figure 3.23 shows the processed vector field for 25 Hz after the large screens were installed at the entrance of the nozzle.

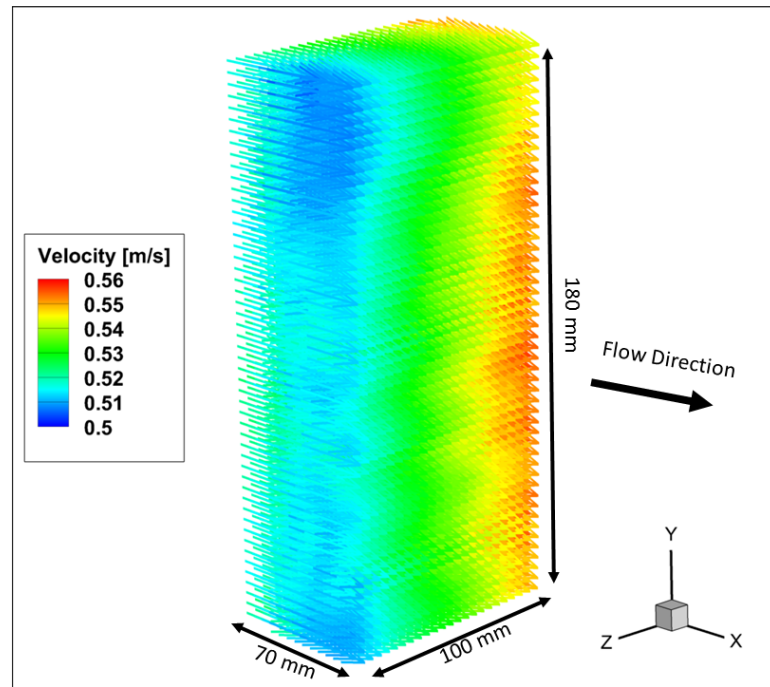


Figure 3.23: $180\text{ mm} \times 100\text{ mm} \times 70\text{ mm}$ processed vector field at motor frequency of 25 Hz after screens were installed at the entrance of the nozzle

Figure 3.24 shows the results of the 7.5 Hz, 10 Hz and 15 Hz. Each frequency shows an approximate 10% difference in average velocity across the test section, which is an improvement from the initial tests which varied from 15% to 20% depending on the motor frequency.

Figure 3.25 shows a comparison of the initial test with the fourth test. The fourth

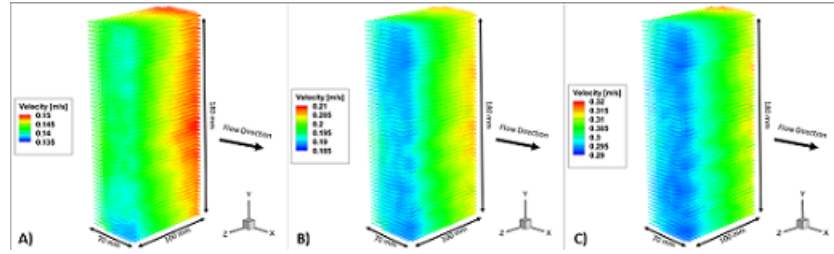


Figure 3.24: 180 mm \times 100 mm \times 70 mm processed vector field at motor frequency of A) 7.5 Hz, B) 10 Hz and C) 15 Hz showing improvements to the non-uniform flow

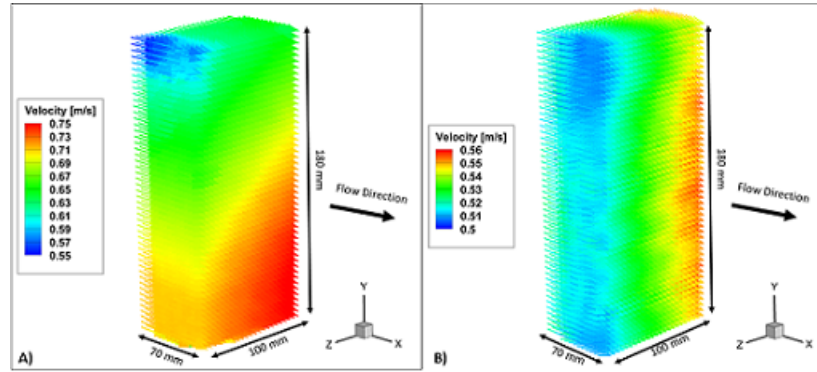


Figure 3.25: 180 mm \times 100 mm \times 70 mm processed vector field at motor frequency of 25 Hz comparison of the A) initial and B) third test

test shows a 10% difference between maximum and minimum velocities compared to 27% difference in velocity observed during the initial test. The screens placed in the entrance to the nozzle smoothed out the flow and eliminated a majority of the pulsing as well as decreasing the velocity gradients across the test section. The disadvantage of the screens was the overall flow velocity reduction from $0.75 \frac{m}{sec}$ to $0.56 \frac{m}{sec}$ at the same motor drive frequency.

3.4 Turbulent Structures in Wake Behind Wall Mounted Cube

3.4.1 Experimental Set Up and Processing

With the water channel motor disengaged and no flow present in the water channel, the calibration target was lowered into the test section. The Dantec Dynamics software was set on live run and all four cameras were individually focused on the

calibration target. External lighting was provided with a high intensity halogen light shining directly on the calibration target. The TomoPIV system was then calibrated as outlined in section 3.2.3. Once the calibration was complete, the calibration target was removed from the test section. The calibration images were processed using a 3rd order polynomial[137], which resulted in an average re-projection error of 0.3093.

The water channel was seeded with 50 μm PSP-50 (Polyamid Seeding Particles) and circulated for five minutes to ensure uniform distribution. The wall-mounted, Rhodamine 6G painted cube was then lowered into the center of the calibrated test volume. The center of the cube was positioned in line with camera #1 as seen in Figure 3.4. The flow was considered fully developed where the viscous effects due to the shear stress between the fluid particles and channel wall do not effect the velocity profile in the center of the test volume[12]. The cameras and laser were controlled from the Dantec Dynamic Studio v2016a and processed as outline in Section 3.2.7.

The average seeding density inside the wake region behind the model was determined to be 0.015 particles per pixel (ppp) and 0.018 ppp in the free stream region. The free stream flow velocity (U_∞) was recorded at $0.75 \frac{m}{sec}$ upstream from the cube. The Reynolds number based on the position of the model on the flat plate was calculated using Equation 2.1 to be 139,000. For examining boundary layer thickness, the characteristic length (l) was based on the length from the knife edge of the plate to the front face of the cube (16.5 cm).

The boundary layer thickness in front of the model on the plate was calculated to be 3.45 mm using Equation 3.1 for laminar flow along the plate [141, 142] for the calculated Reynolds number.

$$\delta_L = \frac{5}{\sqrt{Re_l}} l \quad (3.1)$$

Where δ_L is the laminar boundary layer thickness in mm , Re_l is the dimensionless Reynolds number based on location along the plate and l is the characteristic distance

along the plate in *mm*.

If the Reynolds number had been larger than 5×10^5 , then Equation 3.2 [141, 142] would have been used to calculate the turbulent boundary layer thickness.

$$\delta_T = \frac{0.037}{Re_l^{1/5}} l \quad (3.2)$$

Where δ_T is the turbulent boundary layer thickness in *mm*, Re_l is the dimensionless Reynolds number based on location along the plate and l is the characteristic distance along the plate in *mm*.

The experiment was conducted at 5 Hz for 25 seconds resulting in 125 image pairs. Once the experiment was conducted, the images were analyzed using Dantec Dynamics, Dynamic Studio. The SMART reconstruction ran for 30 iterations with a relaxation value of 0.2 and a threshold value of 0.03 to create the total volume. The resulting spatial resolution was 0.125 *mm*/voxel. The interrogation volume was 91 x 91 x 91 voxels with a 50% overlap and a step size of 30 voxels in each direction. The vector field was created by 12 iterations of LSM technique, which resulted in .019 vectors per *mm*³ totaling 29,000 vectors. Of the 29,000 vectors created, 640 were substituted vectors and 7,680 were rejected.

Unlike 2D PIV systems, there is no direct PIV local error analysis in commercially available TomoPIV software packages. Sources of experimental error were minimized by ensuring proper timing and synchronization between laser pulses and cameras, light volume alignment in the calibrated test volume and light sheet intensity variations, calibration, proper alignment of cameras and compensation for refraction as well as adequate seeding density and size. The sum of processing errors were estimated to be an average of 0.05 pixels [98] based on camera noise, PIV processing scheme, particle size and shape consistency as well as particle out of plane motion.

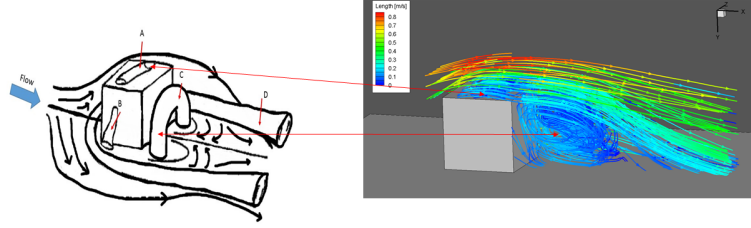


Figure 3.26: Comparison of the Martinuzzi and Tropea schematic and experimental results showing A) top recirculating vortex and C) rear arch vortex.

3.4.2 Flow Visualization Results

The results of the combined volume test of the TomoPIV was compared to the schematic presented by Tropea which was based off of a Re_h (based on height of the channel) range from 80,000 to 115,000 in both water and wind[9]. When this range is converted to the size of the square model used (2.5 cm), the Re_L (based on length of model) is from 40,000 to 57,700, which is slightly lower than the $Re_L = 57,100$ calculated for this experiment a majority of the time. The experimental model aspect ratio: $W/H=1$ where the original reported model aspect ratio: $W/H=0.5$ up to 24. The original model with $W/H=1$ had $H=2.5$ cm compared to the current experimental model of $H=7.62$ cm.

Due to the orientation of the cube in the water channel as seen in Figure 3.6B, the system cannot image the far side of the cube. It is assumed that near side and far side structures are symmetric about the cube. Figure 3.26 show the complete streamline map of the model and the labeled Martinuzzi and Tropea schematic for comparison. The top recirculating vortex (A) as well as the rear arch vortex (C) are clearly visible.

Figure 3.27 show the complete streamline map of the model and the labeled Martinuzzi and Tropea schematic. In this image, the schematic is inverted to better illustrate the near side structures visible to the PIV system. The side recirculating vortex (B) as well as the trumpet (horseshoe) vortex (D) which runs around the model

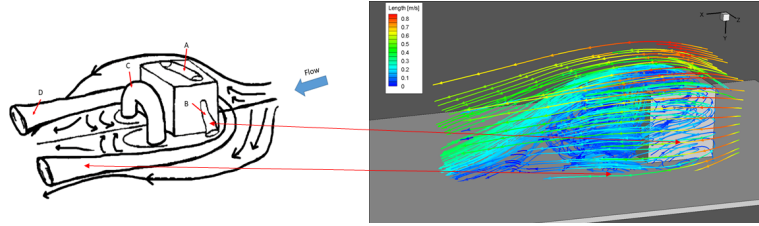


Figure 3.27: Comparison of the Martinuzzi and Tropea schematic and experimental results showing B) side recirculating vortex and D) trumpet (horseshoe) vortex.

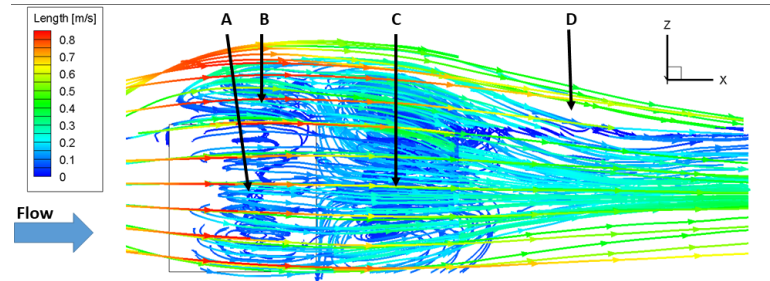


Figure 3.28: Flow of combined vector maps as seen from the top showing A) top recirculating vortex, B) side recirculating vortex, C) rear arch vortex and D) trumpet (horseshoe) vortex.

near the floor are clearly visible.

Figures 3.28- 3.30 show all of the combined vectors maps from the top, side and front of the model and identify the major flow features present and visible from each view. Figure 3.28 shows the complete volume visible to the PIV as seen from the top of the cube. All four flow structures are visible and recognizable. The top recirculating vortex (A) and the side recirculating vortex (B) are visible along the center of the faces of the cube while the rear arch vortex (C) is visible on the back side of the cube. The trumpet horseshoe vortex (D) is more difficult to recognize due to close proximity the body, but its generation is visible between the other structures and the free stream and is expected to grow larger outside of the view of the current test configuration. It also appears that the side recirculating vortex and the top recirculating vortex are connected and feed from the region between the rear horseshoe vortex and the cube.

Figure 3.29 shows the complete volume visible to the PIV as seen from the near

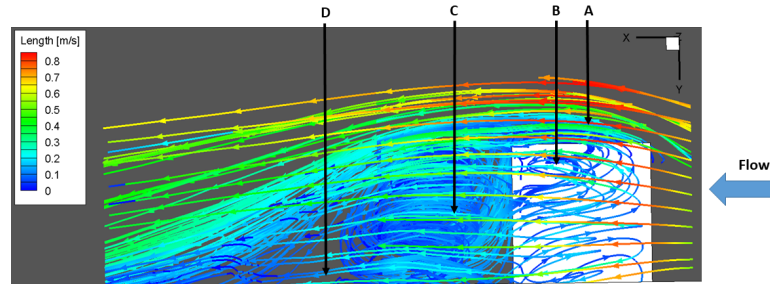


Figure 3.29: Flow of combined vector maps as seen from the near side showing A) top recirculating vortex, B) side recirculating vortex, C) rear arch vortex and the outside edge of D) trumpet (horseshoe) vortex.

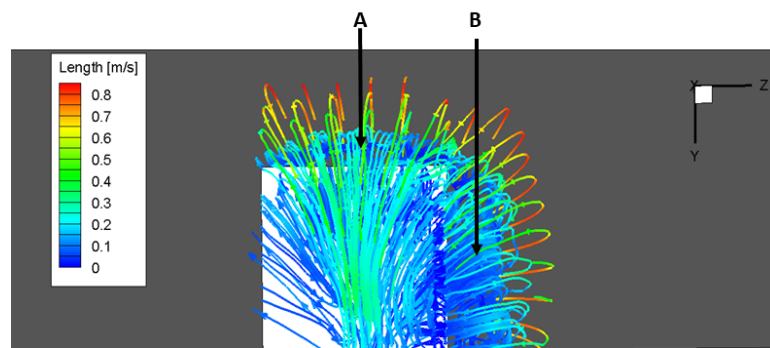


Figure 3.30: Flow of combined vector maps as seen viewing the rear face showing A) top recirculating vortex and B) side recirculating vortex.

side of the cube. From this view, the size of the rear arch vortex (C) is determined to be approximately one cube length and span the region starting at the rear face of the cube. It can also be seen that the free stream velocity is maintained at a distance of approximately $0.5H$ above the cube. Figure 3.31 shows the cube from the opposite side. From this view, the core of the top recirculating vortex (A) and the core of the rear arch vortex (C) are visible.

Figure 3.30 shows the complete volume visible to the PIV as seen looking at the rear face of the cube. From this view, the top recirculating vortex (A) and the side recirculating vortex (B) are visible under the free stream flow vectors. The rear arch vortex is partially visible under the free stream flow vectors.

Figure 3.31 shows a closer view of the flow from the side of the cube. The center of rear arch (A) is visible as well as a more defined top recirculation vortex (B). It can

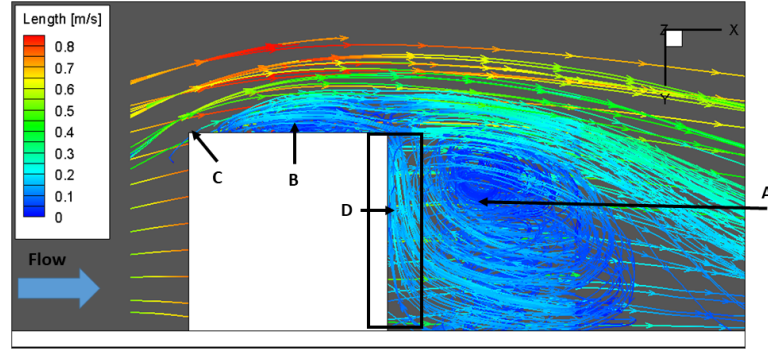


Figure 3.31: Flow of combined vector maps from the side showing A) rear arch vortex, B) top recirculation, C) top front separation and D) flow moving up rear face of cube

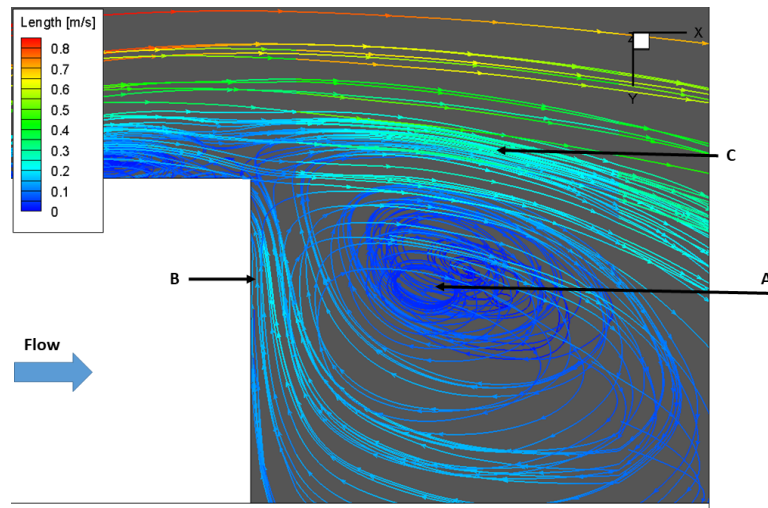


Figure 3.32: Close up view from the side of the rear arch vortex showing A) the center peak of the vortex, B) the reverse flow up the rear face of the cube and C) the joining of the vortex and the separated flow over the cube.

be seen that the flow separates sharply at the front face of the cube at point (C) and does not reattach to the cube at the given flow velocity and body dimensions. This image also shows that a single streamline can be traced from the rear of the cube in the arch vortex, up the rear face of the cube (D) and into the top recirculating vortex before eventually rejoining the flow either above the cube or further downstream. This feeding of the top (and side) vortexes from the rear of the cube is visible in several images.

Figure 3.32 shows a close up view of the rear arch vortex as seen from the side

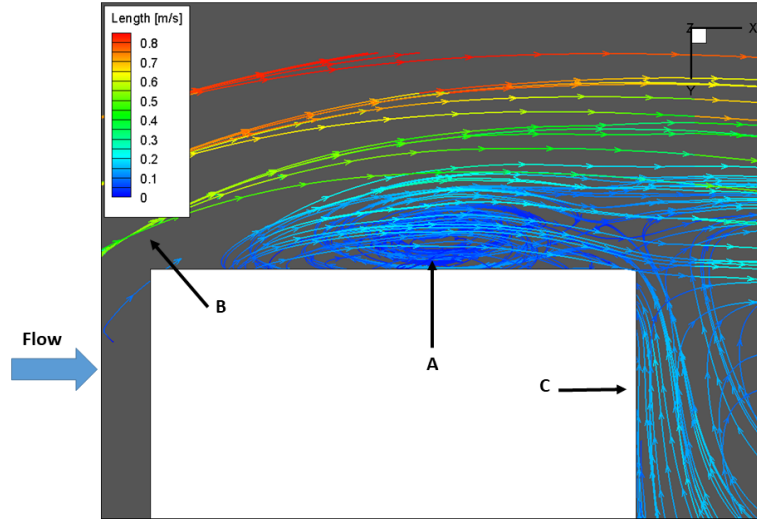


Figure 3.33: Close up view from the side of the top of the cube showing A) the top recirculation vortex, B) the front separated flow and C) reverse flow along rear face.

of the cube. The image clearly shows the center of the rear vortex with a velocity of near $0 \frac{m}{sec}$ at the core of the structure (A). Point (B) shows the recirculation as the flow leaves the arch vortex on the rear of the cube and proceeds up the rear face of the cube at slightly higher velocity than the vortex and then joins the top recirculating vortex (not visible). Point (C) shows where the separated flow over the cube meets and mixes with the top of the arch vortex.

Figure 3.33 shows a close up view of the top recirculating vortex as seen from the side of the cube. The image clearly shows the center of the rear vortex with a velocity of approximately $0.10U_{\infty}$ at point (A). Point (B) shows the separated flow at the front top corner of the model. The streamlines at point (C) are flowing up the rear face of the cube at approximately $0.25U_{\infty}$ and feed the top recirculating vortex.

Figure 3.34 shows a slice of the center plane of the cube as seen from the side. Region (A) on the front face of the cube shows a zero velocity, high pressure area. Point (B) clearly shows the flow velocity gradient from the separation point on the front top corner of the cube up to the free stream. Region (C) is the top recirculating region which has a velocity range from approximately 0 to $0.25U_{\infty}$. Region (D) is the

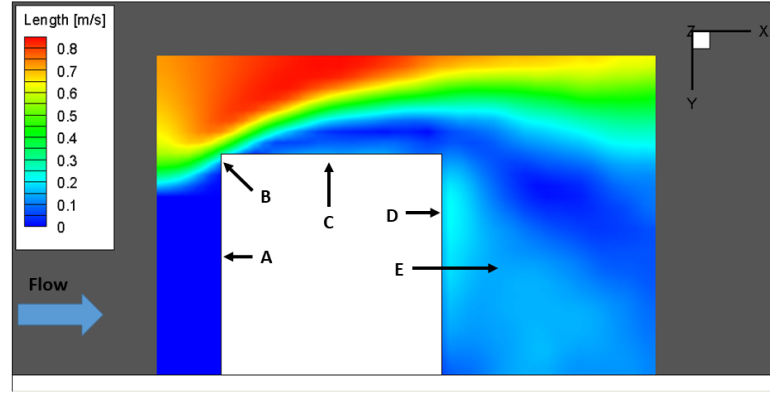


Figure 3.34: Center plane slice of flow around the cube as seen from the side showing velocities at A) front face, B) top corner flow separation, C) top recirculating region, D) reverse flow and E) rear arch vortex region.

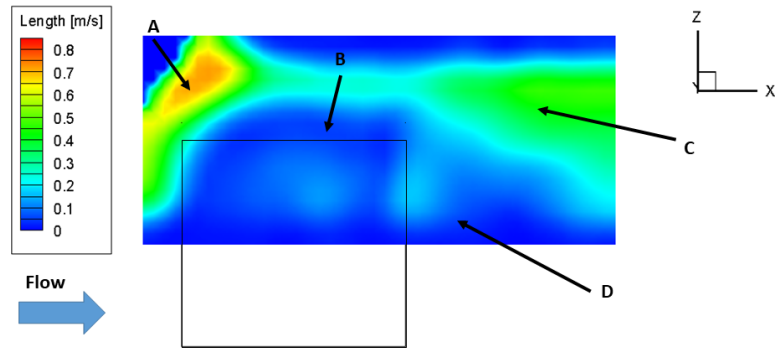


Figure 3.35: Plane slice 2mm above cube of flow around the cube as seen from the top showing velocities at A) separation around the side of the cube, B) side recirculating vortex, C) higher velocity region between trumpet horseshoe vortex and rear arch vortex and D) rear arch vortex region.

reverse flow region up the rear face of the cube, which is also approximately $0.25U_\infty$. Region (E) is the approximate center of the rear arch vortex region, which shows velocities approximately $0.25U_\infty$.

Figure 3.35 shows a slice of the flow 2 mm above the cube as seen from above looking down. Region (A) in front of the cube shows a near free stream velocity after flow separates from the front face and the top. Point (B) shows the near zero velocity side recirculation region. Region (C) is a higher velocity region, approx $0.5U_\infty$ that resides between the trumpet horseshoe vortex and the rear arch vortex. The edge of

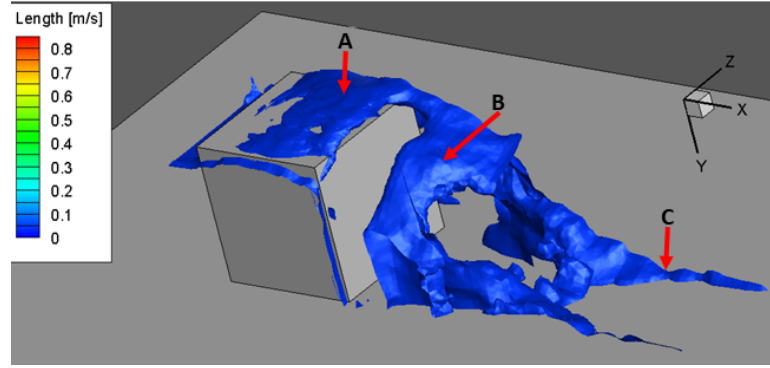


Figure 3.36: Isosurface of the flow at $0.04 \frac{m}{sec}$ showing A) top recirculating vortex, B) rear arch vortex and C) trumpet horseshoe vortex

the trumpet vortex is visible above the higher velocity region. Region (D) shows the top of the rear arch vortex and the reverse circulation along the rear face of the cube, which is also approximately $0.25U_{\infty}$.

Figure 3.36 shows the isosurface at a constant velocity of 0.04 m/s within the test volume. At this constant velocity, the core of the (A) top recirculating vortex, (B) rear arch vortex and a portion of the (C) trumpet horseshoe vortex are fully developed and easily visible.

Figure 3.37 shows a closer view from the rear of the cube, where the separation between the (A) top recirculating vortex and the top of the cube is visible as well as (B) the core of the rear arch vortex. From Figure 3.37 it can be seen that the core of the top recirculating vortex in fact attaches to the top of the cube and is not connected to the side vortex as previously seen in Figure 3.28.

With a free stream velocity of $0.75 \frac{m}{sec}$ and image collection frequency of 5 Hz , the resulting temporal resolution was 0.2 seconds between image pairs. Therefore, inside the free stream, a particle would travel 150 mm between image pairs and not be captured in two consecutive image pairs, rendering the system in its current configuration, unable to track structures as they move through the field of view inside the free stream.

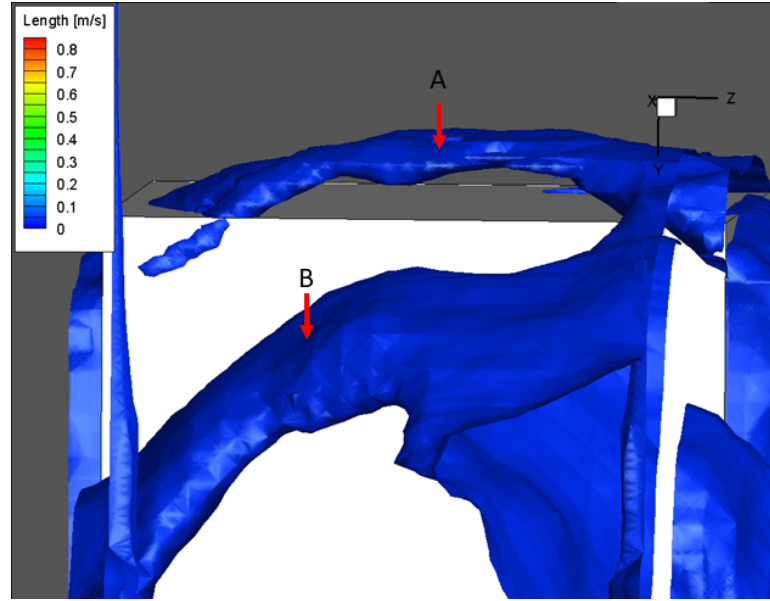


Figure 3.37: Zoomed in view of iso surface of the flow at $0.04 \frac{m}{sec}$ showing A) top recirculating vortex and B) rear arch vortex

3.5 Summary

The University of North Carolina at Charlotte (UNCC) Motorsports Research Lab SPIV system was updated to a TomoPIV system to increase the lab's capabilities to capture volumetric velocity data inside the water channel. The updated system also required minor modifications to the water channel.

Additional experiments were conducted to determine model pre-processing requirements and flow seeding to attain the most reliable results. It was determined that applying Rhodamine 6G or florescent pink paint in conjunction with a low-pass filter on the camera mitigated surface reflections which increased the signal to noise ration in the processing and improved the PIV system's ability to process accurate vector maps. Two different flow seeding particles were tested. The $50 \mu m$ PSP-50 seeding particles produced a larger test area and deeper depth of field and were utilized throughout this study.

With the increased flow measuring capabilities, it was determined that the flow

characteristics of the water channel were non-uniform. A series of flow smoothing screens and an anti-cavitation plate were installed in the water channel to reduce the velocity difference across the channel to less than 10% inside the test volume.

After numerous upgrades and improvements to the equipment and instrumentation, it is possible to gather data and get volumetric representation of the flow around a bluff body, which historically has been mostly qualitative, or limited to a very small volume or plane. With the confirmation of the system capability to acquire and measure the velocities, vector maps were produced, which when averaged allowed for the recognition of flow structures. When compared to Martinuzzi and Tropea, all of the structures match for the experimental Reynolds number 57,100. This capability allowed for the determination of the velocities inside the core of the vortex at a specific free stream velocity and model dimensions. It also allowed for the visualization and confirmation of a variety of flow phenomenon, such as the reverse direction flow off of the rear arch vortex that proceeds up the rear face of the model to feed the top vortex. The results of this study provide detailed, numerical data of the velocities inside the volume near and in the wake of the bluff body not previously possible.

3.5.1 Future Work

Although work was conducted to smooth out the flow and decreased the overall velocity gradient across the test chamber, which improved the testing capabilities, it also reduced the water channel velocity. Additional upgrades to the water channel such as an active flow monitoring system and control system to maintain steady uniform flow would greatly improve the results while maintaining the channel's velocity capabilities.

To improve the system and track flow structures in time, a higher frequency system of 1,000 Hz or greater is required at the current velocity and Reynolds number. Beyond additional equipment and improvements, testing other geometries at various

velocities will greatly increase the basic understandings of flow physics.

CHAPTER 4: STUDY OF TURBULENT STRUCTURES AND PRESSURE CORRELATIONS UTILIZING PARTICLE IMAGE VELOCIMETRY IN AN EIFFEL WIND TUNNEL

To gather flow visualization data in the wake region of a bluff body, the UNCC Eiffel wind tunnel was modified. A 2D PIV system was installed along with a series of pressure sensors to gather velocity and pressure data on the bluff body as well as in the wake region.

The results of the PIV portion of the study provided a series of planes, which when stitched together formed a volume of comparable size to Chapter 3. Flow structures around the cube were identified and compared to the Martinuzzi and Tropea benchmark schematic as well as the results of Chapter 3, which demonstrated the improved capabilities of the TomoPIV system.

A cross-correlation of the pressure data was then conducted. The results showed only minor correlation between the front sensors at a time lag equivalent to half of the free stream velocity in the boundary layer. The rear and side sensors on the cube, all of which are located inside of recirculation regions also showed faint correlations at numerous time steps. The wake region sensors showed strong correlations with the two closest sensors. The time step of the correlations increased from less than half the free stream velocity near the cube to free stream velocity three cube lengths behind the body. These far field readings had the strongest correlation and show the reattachment location of the flow to be between two and half and three cube lengths behind the body, much farther than originally believed.

The combination of the PIV data with the pressure correlations can be used

to expand the understanding of the flow behind a bluff body and validate existing computational models.

4.1 Wind Tunnel

The UNC Charlotte wind tunnel is an Eiffel wind tunnel with a 0.3 m^2 by 0.7 m long test section enclosed in a 2.5 m box as seen in Figure 4.1. The wind tunnel walls, encased inside the box, were adjustable to allow for different size models while minimizing blockage effects [69]. The wind tunnel has an 8:1 inlet contraction section with a nylon screen to condition the flow and is powered by a 15 hp motor with a frequency drive which is capable of speeds ranging from $9.8 \frac{\text{m}}{\text{sec}}$ to $45.5 \frac{\text{m}}{\text{sec}}$. The interior walls were constructed out of thin wood slats which were glued to adjustment rails situated outside of the tunnel. These slats were prone to separation which caused disturbances in the air flow. As seen in Figure 4.1, only a small access window in the side wall allowed for observation of the test section and made flow visualization methods nearly impossible.

Utilizing this open return, suction driven wind tunnel with flexible walls, the flow can be brought to a steady, uniform condition by altering the walls while monitoring the pressure at 10 cm intervals along the length of the tunnel. The tunnel walls can diverge or converge to compensate for the blockage due to either the model, the boundary layer growth or both. By adjusting the walls, a 0 pressure gradient can be obtained from upstream of the model to downstream of the wake, or can give the pressure gradient required to calculate correction factors [143].

The tunnel was updated by removing the external box and replacing the far side interior wood slat wall and roof with a polycarbonate wall and roof as seen in Figure 4.2 to allow for flow visualization. The roof section was separated into three sections. The roof sections near the intake and exit were attached directly to roof adjustment rails to maintain the ability to expand the test section while the center



Figure 4.1: Original configuration of UNC Charlotte Motor Sports Research Lab scale wind tunnel

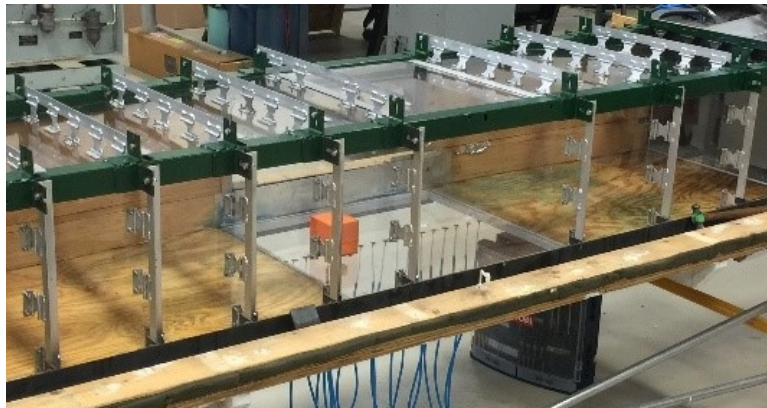


Figure 4.2: Wind tunnel after wall replacement

piece was attached to the two outside sections using "H" cross section aluminum slots. This allows for easy removal and insertion of the center section depending on instrumentation requirements for the experiments as seen in Figure 4.3.

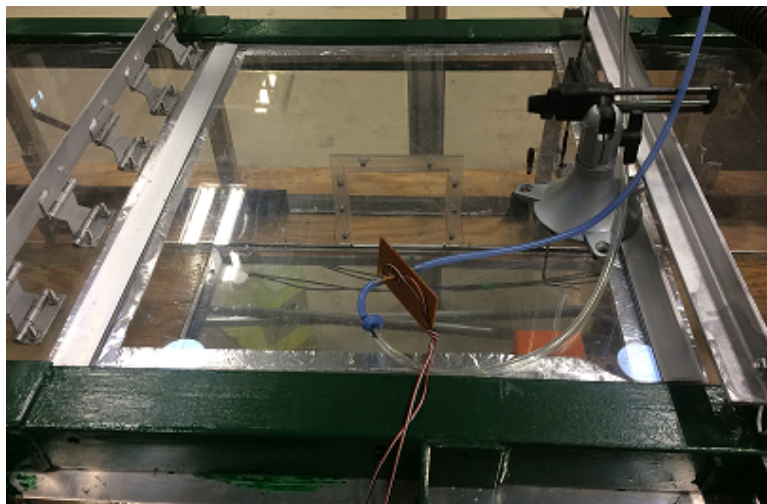


Figure 4.3: Wind tunnel roof center section with pitot tube installed

The wind tunnel originally had a solid wooden floor which made changes in experimental setups difficult. To improve this situation, the floor was divided into three sections. The sections near the intake and exit remained the original floor while the center section was removed and replaced with an aluminum frame. The aluminum frame makes the test section modular so that an experiment can be set up outside of the wind tunnel and then bolted into the aluminum frame. This allows for rapid and easy replacement of experimental set up and instrumentation and minimizes tunnel down time. Two initial test sections were built. The first was a flat plate with a bluff body cube attached as seen in Figure 4.4A and used in this body of work. With the cube installed in the test section, the blockage ratio was calculated to be 3.8%, which is less than the 5% as specified by Maskell [73], so no corrections are required. The second test section was a rolling road as seen in Figure 4.4B which was designed, implemented and tested during the tunnel upgrades. This test section has been used in scaled tire testing [68] and with the addition of the updated PIV system, wake research behind a rolling tire. Similar rolling road devices have been utilized for various types of vehicle aerodynamic testing[14, 15].

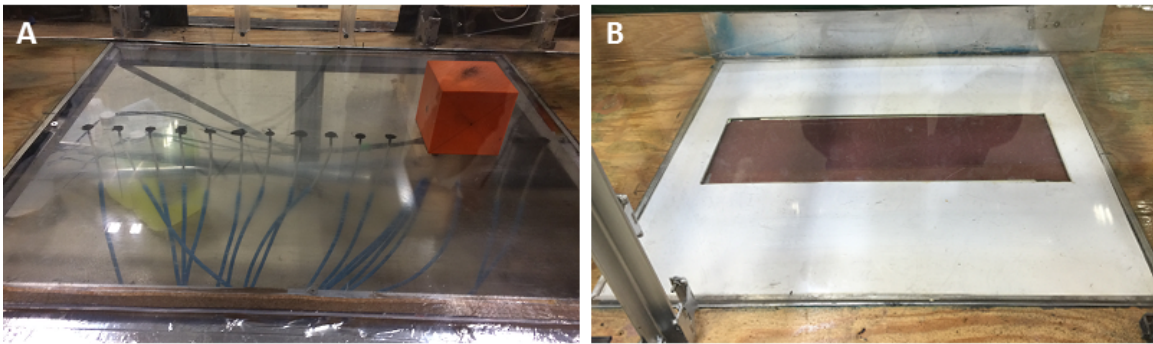


Figure 4.4: Modular test section floor with A) cube and pressure sensors and B) rolling road

To improve overall flow quality and seeding uniformity, a 128 cm^3 settling chamber was added to the wind tunnel intake. A 50 mm thick honeycomb with 6.35 mm cells was placed at the inlet to the settling chamber to straighten the flow. The settling

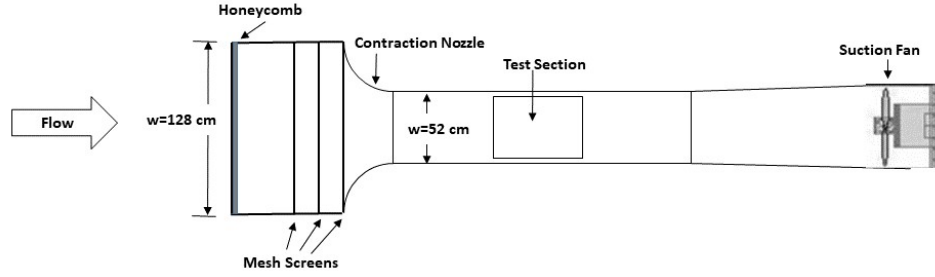


Figure 4.5: Schematic of Eiffel wind tunnel with settling chamber

chamber contains three sets of 0.003 mm wire diameter, 1 mm square mesh spaced 200 mm apart. Figure 4.5 shows a schematic of the wind tunnel and settling chamber.

4.2 Particle Image Velocimetry

The 2D PIV system used in the wind tunnel is comprised of a 532 nm laser and a single high-speed dual frame CMOS camera. The camera and the laser were attached to an isolated frame on rails to allow for the two to move in tandem and maintain calibration through each plane of data acquisition as seen in Figure 4.6.

4.2.1 Camera

The camera is a FlowSense[®] CM 12M-70 dual-framing CMOS camera which is capable of capturing dual frame pictures at 12 Megapixels at 35 Hz. The camera was equipped with a Nikon[®] AF Nikkor 50 mm lens and narrow band 532 nm filter. The aperture setting and time step between first and second image are reported for each iteration of the study since these parameters are dependent on the type of seeding and light conditions.

4.2.2 Laser

The laser used in the wind tunnel is a LPY704-100 PIV Class IV Litron[®] DualPower, dual cavity, Nd:YAG with 12 ns pulse width at 100 Hz. The laser has a

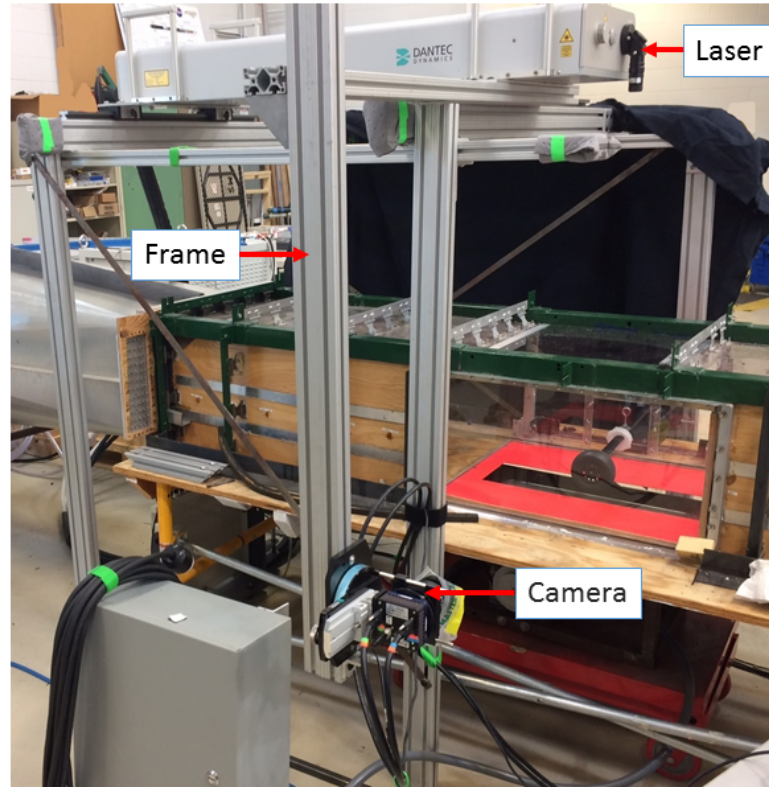


Figure 4.6: Laser and camera attached to isolated frame

pulse capability of 100 mJ per pulse at 532 nm wavelength. It is equipped with a planar illumination optic which produces an approximately 2 mm thick sheet of laser light to the test area.

4.2.3 Calibration

The PIV system was calibrated using the pixel scaling factor available in the PIV software. This process utilized a $300 \text{ mm} \times 300 \text{ mm}$ calibration target consisting of a known grid of dots. The target was placed perpendicular to camera lens, in the center of the test area 660 mm from the surface of the lens and a single image captured. The distance markers, A and B were placed on two dots on the outside edge of the grid along the same vertical line and the known distance between those two dots were entered into the program as seen in Figure 4.7.

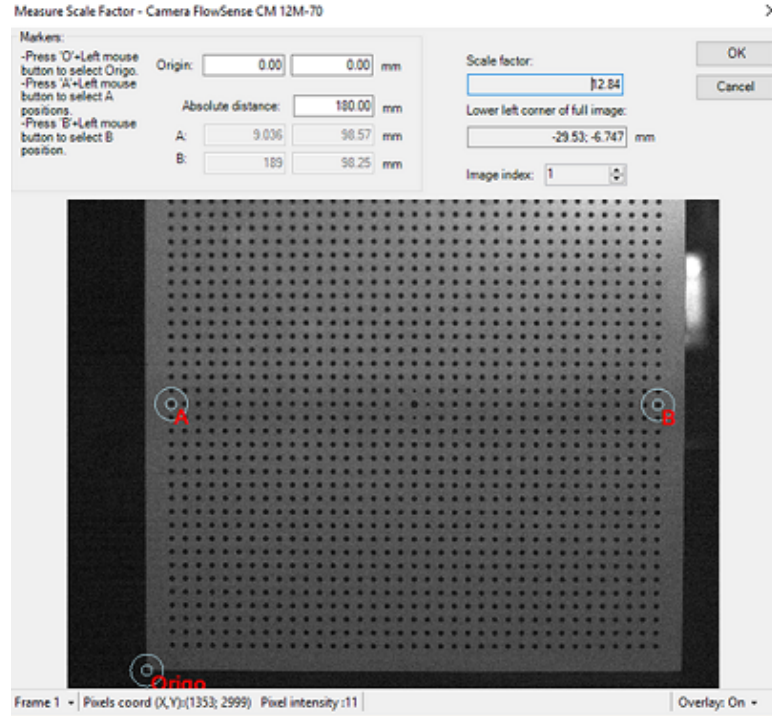


Figure 4.7: PIV Measure Scale Factor window showing location markers, absolute distance and computed scale factor

4.2.4 Seeding Particles

Wind tunnel seeding is instrumental in gathering reliable and accurate data[144]. There are several different methods to seed an open return wind tunnel with uniform particles to include smoke, hydrogen bubbles and olive oil mist. These three different seeding methods were used in an empty tunnel to determine which produced the best results for the experimental setup and PIV processing. For the first wind tunnel experiment, a Rosco[®] Vapour Fog generator with Rosco[®] fog fluid was used at the minimum setting to deliver smoke particles with a nominal diameter of $1\ \mu m$. The second iteration of experiments utilized a Dantec Dynamics 10F03 seeding generator, supplied with 103 *kPa* of compressed air which produced neutrally buoyant olive oil particles with a nominal diameter of $5\ \mu m$. The third iteration used a SAI[®] Model 5, Helium Filled Soap Bubble (HFSB) Generator system which produced neutrally buoyant particles with a nominal diameter of $1\ mm$. The results of these tests are

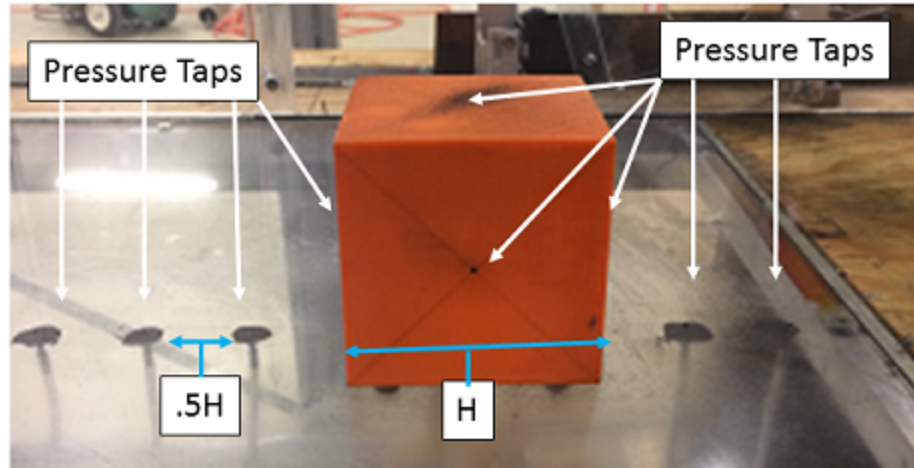


Figure 4.8: Placement of pressure sensor taps along floor and walls of cube

located in Section 4.4.2.

4.3 Sensors and Program

There are a number of existing methods to measure pressure inside the flow field, to include pressure sensors, pressure sensitive paint and PIV velocity data. The traditional pressure tap measurements are limited by their size and location inside the flow[35], but are simpler to set up and manage than the processing required to get the pressure fields from the PIV data. The sensors utilized in this experiment to measure the pressure on the surfaces of the cube and along a straight line in front of and behind the cube were Silicon Microstructures[®] SM5600 Series OEM differential pressure sensors. These sensors have the ability to measure up to 1000 Pa and have a zero offset calibration and temperature compensation. The sensors have a 0.05 % full scale repeatability as well as linearity. The sensors were connected to the model and the plate with 50 cm lengths of tubing. Pressure taps were inserted into the center of each face of the cube and were spaced in increments of $0.5H$ (half the width of the cube) in front of and behind the cube for a total of two taps in front of the cube and 8 behind the cube as seen in Figure 4.8. An additional sensor monitored the ambient pressure conditions outside of the tunnel.

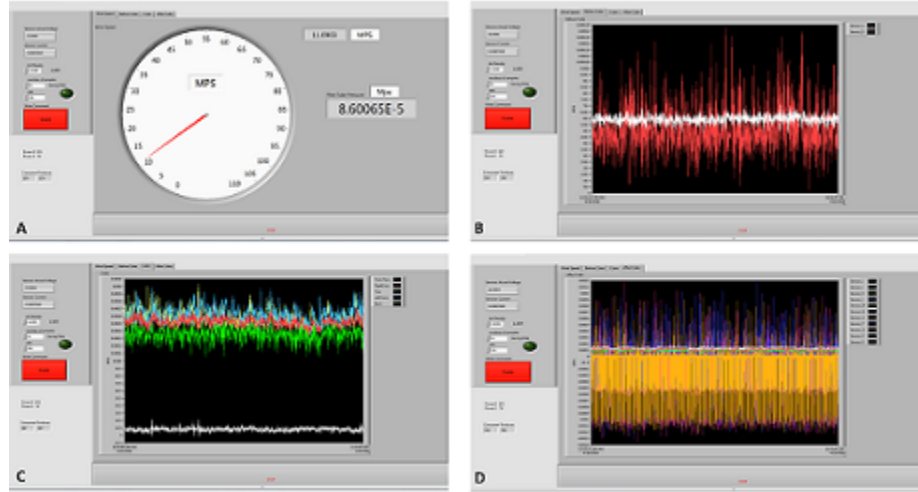


Figure 4.9: Front screen of wind tunnel pressure and airspeed LabView[®] program A) airspeed, B) pressure before cube, C) pressure on the cube and D) pressure after the cube.

The pressure sensors were wired to a circuit board and attached to a National Instruments[®] NIUSB-6343 which was capable of gathering data at 1,000 Hz for each channel. During the tunnel upgrades, a National Instruments[®] PXIe-1071 data acquisition system replaced the NIUSB-6343. The LabView[®] program was also updated, which allowed for data acquisition up to 50,000 Hz per channel.

During testing, the air density based on the current lab conditions was manually inserted into the program front panel. The front panel consists of four tabs which present data based on the type and location of the sensors as seen in Figure 4.9. The first tab (Figure 4.9A) displays the wind speed in the tunnel in the free stream directly above the cube. The second tab (Figure 4.9B) shows the real time pressure readings of the two taps in front of the cube. The third tab (Figure 4.9C) displays the real time pressure readings of the five taps on the cube while the final tab (Figure 4.9D) displays the readings from the taps situated behind the cube. Figure 4.10 shows schematically the sensor placement and identification used inside the LabView[®] program.

When the program is initiated and the tunnel at steady state speed, the wind velocity was calculated utilizing Equation 4.1 with pressure data gathered by the

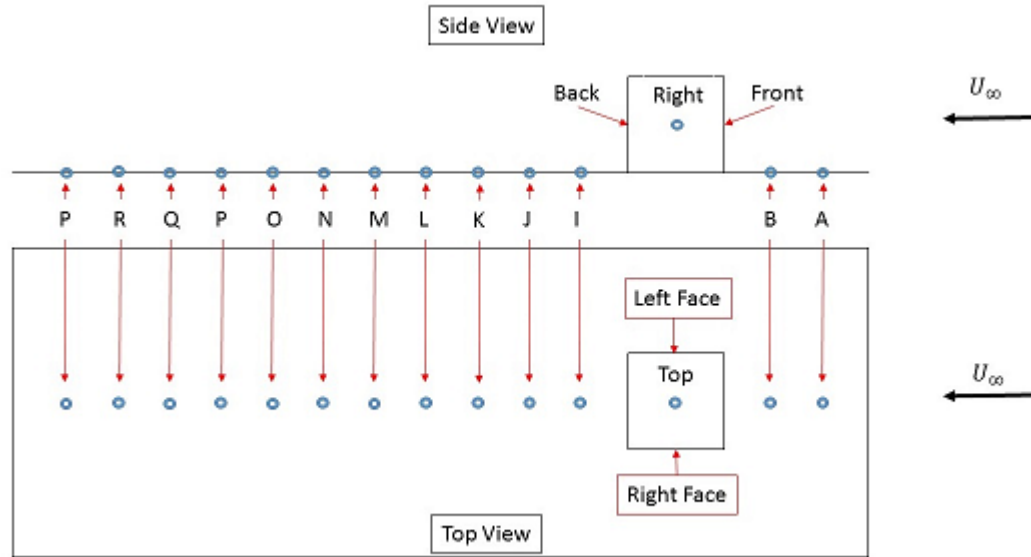


Figure 4.10: Schematic of wind tunnel test section with placement and identification of sensors

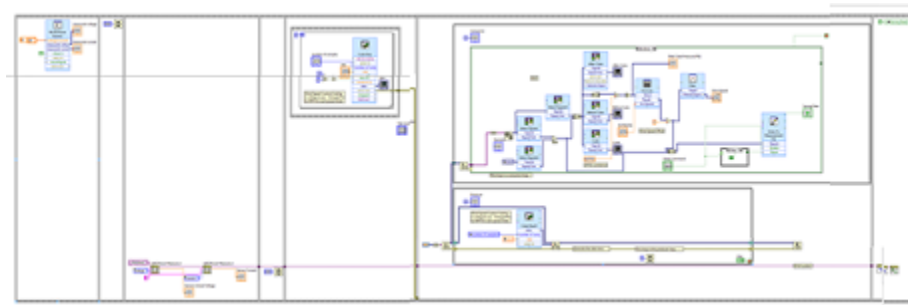


Figure 4.11: Back panel of wind tunnel pressure and airspeed LabView® program

pitot tube inserted into the free stream flow above the model.

$$v_A = \sqrt{2 * \frac{\Delta P * 6894.76}{\rho}} \quad (4.1)$$

Where v_A is the velocity of the air in meters per second, ΔP is the pressure difference in pounds per square inch (PSI), ρ is the air density in $\frac{kg}{m^3}$ and 6894.76 is a conversion constant from *psi* to *Pa*.

Figure 4.11 shows the back panel of the data acquisition program. Detailed views of the LabVIEW® code can be found in Appendix A.1.

4.4 Turbulent Structures and Pressure Correlations

4.4.1 Experimental Set Up and Processing

A group of tests were conducted to characterize the empty tunnel and determine the seeding requirements. To closely match the water channel Reynolds number, the wind tunnel was operated at $11.1 \pm 0.10 \frac{m}{sec}$ with an empty test section. A pitot tube and LabVIEW[®] program was utilized to gather velocity data from the floor of the wind tunnel to the roof in 5 mm steps to determine the velocity profile at the entrance of the test section.

With the wind tunnel disengaged and no flow present in the tunnel, the calibration target was lowered into the test section. The Dantec[®] Dynamic Studio software was set on "free run" and focused on the calibration target. External lighting was provided with a high intensity halogen light shining directly on the calibration target. The PIV system was then calibrated as outlined in section 4.2.3. Once the calibration was complete, the calibration target was removed from the test section. The calibration resulted in a scale factor of $12.88 \frac{pixels}{mm}$.

The wind tunnel was seeded as outlined in section 4.2.4. The camera and laser were controlled from the Dantec[®] Dynamic Studio v2016a. The free stream flow velocity (U_∞) was recorded at $11.1 \pm 0.35 \frac{m}{sec}$. To minimize surface reflections, the wall and floor of the wind tunnel were coated with florescent pink paint.

Once the empty channel results were gathered for all three seeding types, the results were processed to determine the best seeding type and processing steps. The flat floor plate was removed from the test section, and the plate containing the cube and pressure sensors were affixed inside the test section. The PIV system was then re-calibrated using the $300 mm \times 300 mm$ calibration target and returned a scale factor of $12.84 \frac{pixels}{mm}$.

After calibration was completed, the wind tunnel was activated at $11.1 \pm 0.35 \frac{m}{sec}$ and allowed to run for one minute to reach steady state flow. The wind tunnel stayed active during the entire experiment. The test section was seeded using olive oil as determined by the results of the empty tunnel experiment. The test was conducted over 11 planes resulting in a test area depth of 110 *mm*.

For all of the PIV tests executed in the wind tunnel, the data acquisition and processing was controlled by Dantec Dynamics' Dynamic Studio 6.0.3. The software maintained timing and triggered the camera and laser simultaneously. The data acquisition, when triggered from the PIV software, fired the laser at 100 Hz and operated the camera at 25 Hz for 10 seconds to give 250 double-frame images. The double-frame images were captured with 30 μs between frames.

The LabVIEW[®] program was triggered simultaneously with the PIV system and gathered data from the 15 sensors (2 in front of model, 5 on model and 8 behind the model) for the same duration as the image collection resulting in 100,000 samples. Once the data was gathered for all 11 planes, the wind tunnel and olive oil seeding generator were deactivated.

The images were then post processed. Due to the minor differences in each iteration, the exact post processing steps for each will be outlined in the results section. For each iteration except the -10 *mm* plane, an image mask was utilized similar to the masking procedures outlined in Section 3.2.7. Vector maps of the image pairs were created using the adaptive PIV algorithm, which deforms or alters the interrogation window grid size between frames in order to optimize for local seeding density and velocity gradients [145]. Wall windowing was used to mask the location of the wall and mitigate wall bias. Once the vector maps were completed, the vector maps were averaged to observe the flow structure within the interrogated plane. For each iteration of the experiment, the built in "peak ratio" uncertainty analysis method developed by Charonko and Vlachos[132] was utilized.

The pressure data was then averaged over the eleven iterations and processed. The raw averaged data was autocorrelated as well as cross correlated with the other pressure tap locations. The averaged data was then smoothed using a Butterworth low-pass filter (Appendix A.2) to remove the noise. The program was modified for all three regions of the sensors; i) upstream, ii) cube body and iii) wake.

4.4.2 Empty Tunnel Results

To determine the estimated boundary layer thickness at the model location, a 3 *mm* diameter pitot tube with a single 1 *mm* orifice was inserted through the roof of the tunnel and velocity values were gathered using the velocity function of the LabVIEW® program described in Section 4.3. The pitot tube was placed on the floor of the tunnel, 120 *mm* from the floor transition (location of the front face of the cube) with the cube removed. The pitot tube was raised in 5 *mm* steps from the floor of the tunnel to the roof. The velocity data was gathered for 10 seconds at each step and then averaged.

Figure 4.12 shows the mean velocity profile inside the empty test section. The boundary layer thickness at the cube mounting location, 120 *mm* from the floor transition with the cube removed where the flow has returned to 90% U_∞ is shown in Figure 4.13 to be $z/h=0.20$.

To determine the best seeding available for the existing PIV system and experimental set up, three different seeding types were tested.

Smoke

Smoke was the first seeding type tested. The FlowSense® CM 12M-70 dual-framing CMOS camera was set to 25 Hz with the aperture set at f/8. Due to the capabilities of the smoke generator, the smoke was concentrated near the floor of the test section as seen in Figure 4.14 to gather the most relevant information. Based

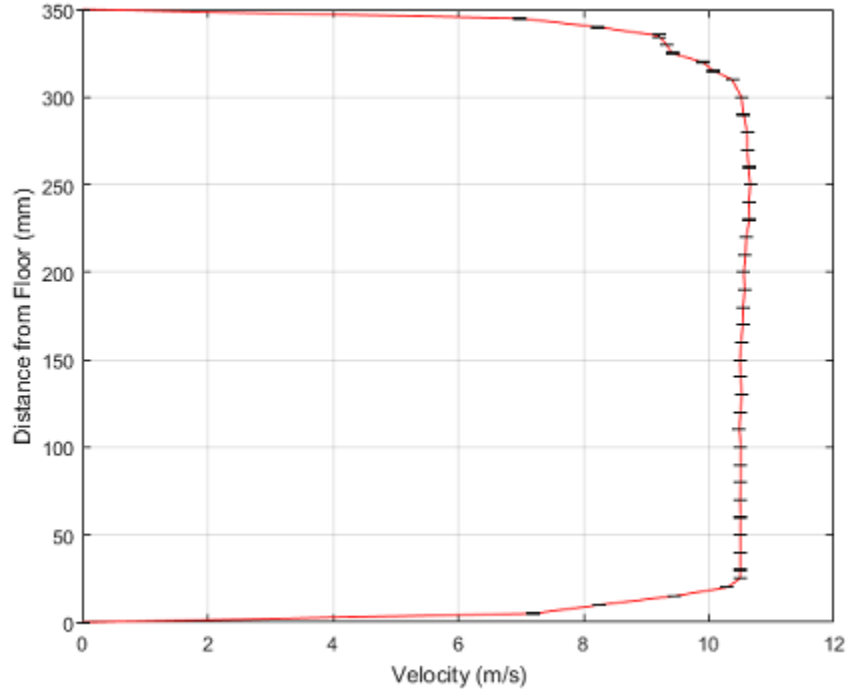


Figure 4.12: Velocity profile at the cube location with the cube removed

on the tunnel configuration, the laser cannot reach the entire FOV of the camera and some of the flow information is lost in the downstream area of the image. Once the images were gathered, they were processed using the adaptive PIV function of Dynamic Studio. The seeding density for smoke inside the test section was determined to be 0.036 particles per pixel with a mean particle diameter of 1.3 pixels.

The adaptive PIV algorithm used a grid step size of 16 by 16 pixels with a minimum interrogation size of 32 by 32 pixels and a maximum interrogation size of 64 by 64 pixels. The adaptive PIV processing produced vector maps with an average of 27,390 vectors, 1564 rejected vectors and 2553 substituted vectors. Figure 4.15 shows one of the 250 processed vector maps. From the processed vector map, gaps in the smoke can be seen as well as some vorticity in the flow.

Once the vector maps were completed, the vector statistics were calculated to produce an average vector field map to observe the flow within the interrogated plane as seen in Figure 4.16 which showed a minimum average velocity of $0.0016 \frac{m}{sec}$ near

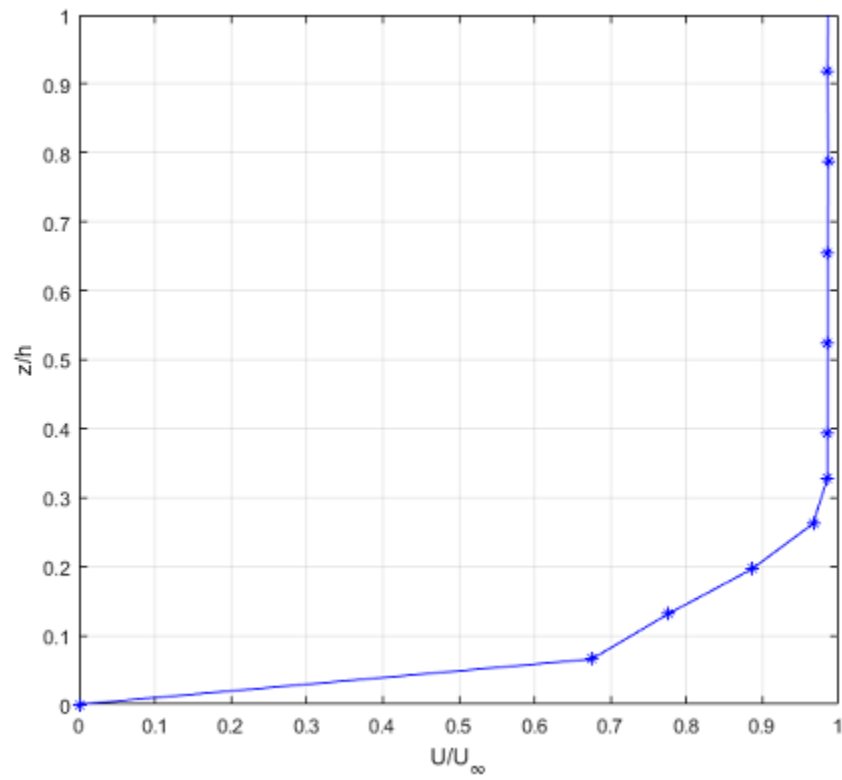


Figure 4.13: Boundary layer mean profile at the cube location with the cube removed

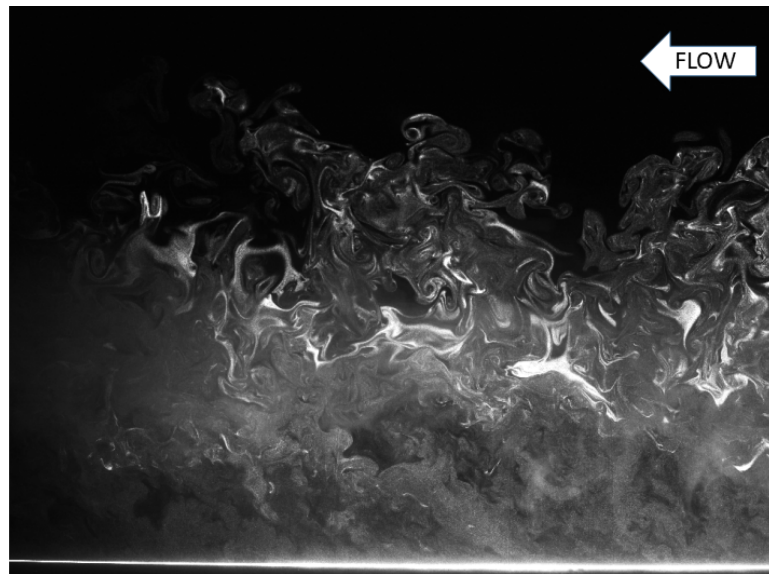


Figure 4.14: Raw data image of empty tunnel smoke test

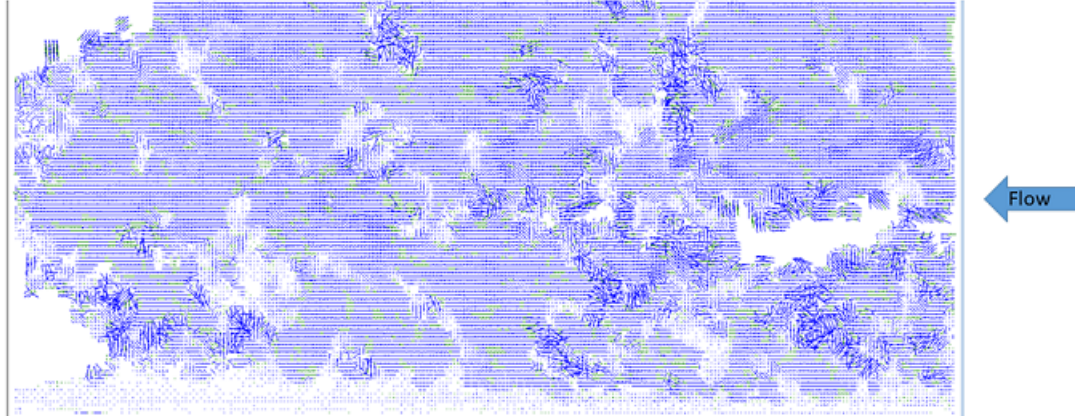


Figure 4.15: Processed vector map of empty tunnel smoke test

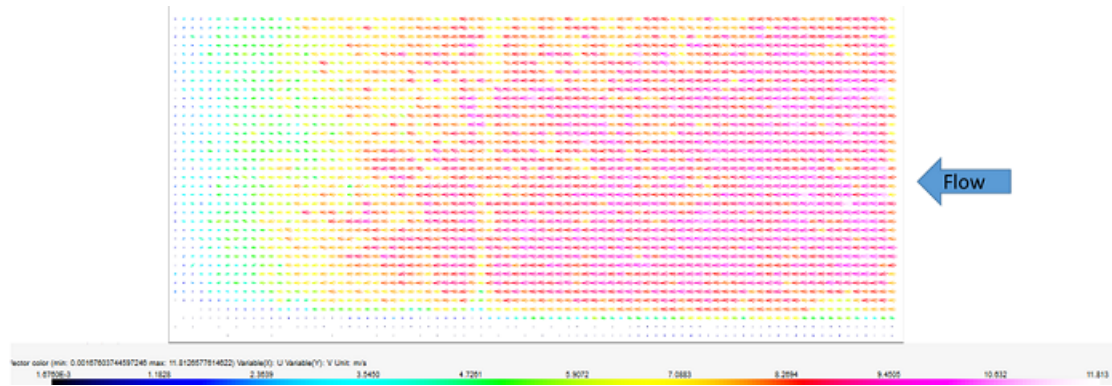


Figure 4.16: Processed vector statistics map of empty tunnel smoke test

the floor and a maximum average velocity of $11.51 \frac{m}{sec}$.

The slower velocities shown at the downstream edge of the test area in Figure 4.16 is due to the number of zero velocity vectors created in the region where there are large gaps in the smoke coverage and laser light blockage due to tunnel configuration. Additionally, a distinct boundary layer approximately 20 *mm* thick can be seen growing along the bottom of the vector map as shown in Figure 4.17.

Olive Oil

Olive oil was the second seeding type tested. The FlowSense[®] CM 12M-70 dual-framing CMOS camera was set to 25 Hz with the aperture set at f/2.5. The olive oil mist particles were not as visible to the naked eye as the smoke was, however it did

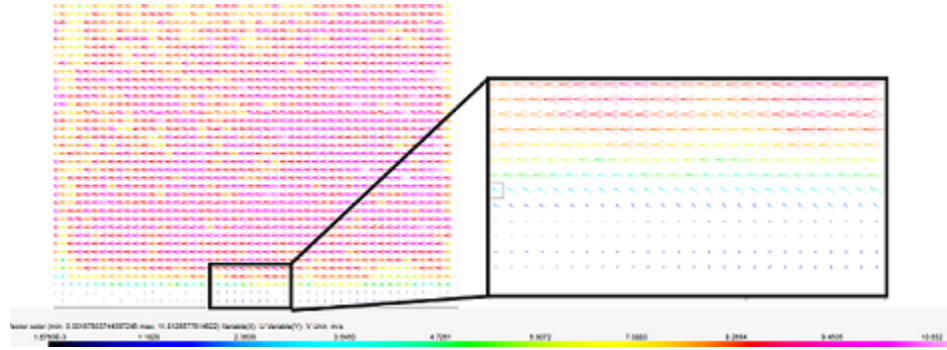


Figure 4.17: Processed vector statistics map of smoke test with expanded view of boundary layer

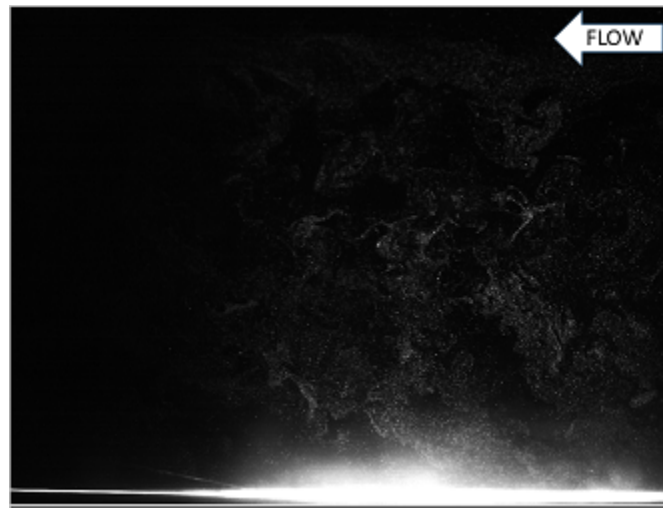


Figure 4.18: Raw data image of empty tunnel olive oil test

fill the test chamber more uniformly as seen in Figure 4.18 to give a larger number of data points in the vertical plane for PIV processing.

As with the smoke, some of the flow information is lost in the downstream area due to tunnel configuration. Once the images were gathered, they were processed using the adaptive PIV function of Dynamic Studio. The seeding density for olive oil inside the test section was determined to be 0.044 particles per pixel with a mean particle diameter of 2.0 pixels.

The adaptive PIV algorithm used a grid step size of 16 by 16 pixels with a minimum interrogation size of 32 by 32 pixels and a maximum interrogation size of 64 by 64 pixels. The adaptive PIV processing produced vector maps with an average of

46,314 vectors, 3976 rejected vectors and 6177 substituted vectors. Figure 4.19 shows one of the 250 processed vector maps. From the processed vector map it was determined that the olive oil produced larger velocity fluctuations and a higher percentage of substituted vectors. The image also shows that there are fewer gaps in the data than were visible in the smoke.

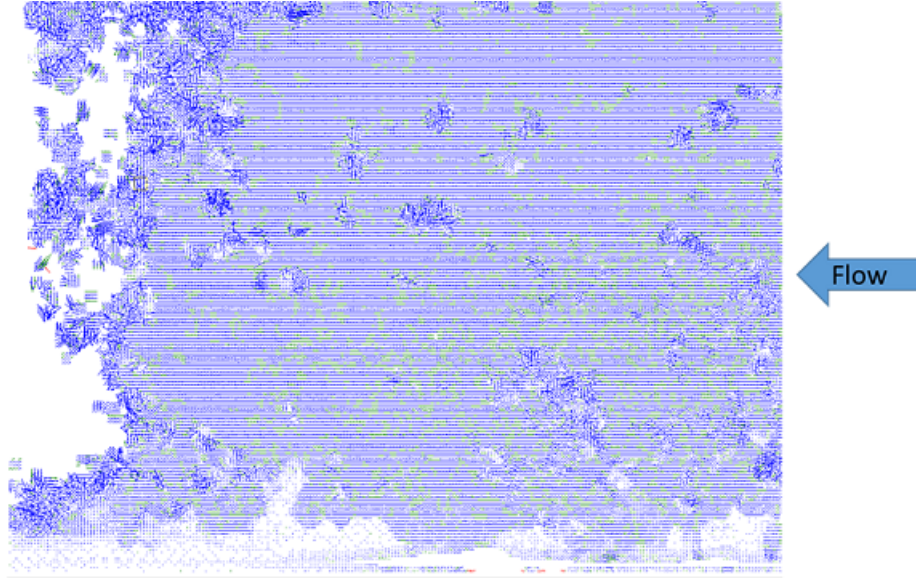


Figure 4.19: Processed vector map of empty tunnel olive oil test

Once the vector maps were completed, the vector statistics were calculated to produce an average vector field map to observe the flow within the interrogated plane as seen in Figure 4.20 which showed a minimum average velocity of $0.0024 \frac{m}{sec}$ near the floor and a maximum average velocity of $11.75 \frac{m}{sec}$. As with the smoke test, the slower velocities shown at the downstream edge of the test area are due to gaps in the laser light caused by the tunnel configuration.

The boundary layer is still visible as seen in Figure 4.21, but fluctuates between 20 and 25 *mm* thick and shows several high value vectors close to the floor. The noticeable differences between the smoke and the olive oil in the boundary layer area is due to the PIV systems ability to track the larger, more defined olive oil particles.

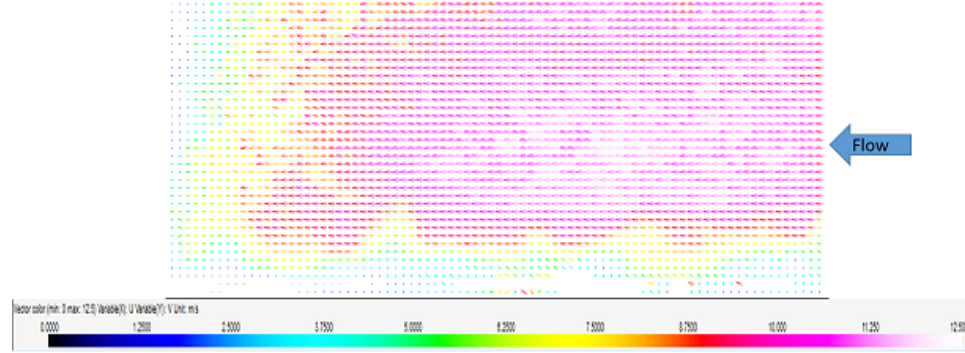


Figure 4.20: Processed vector statistics map of empty tunnel olive oil test

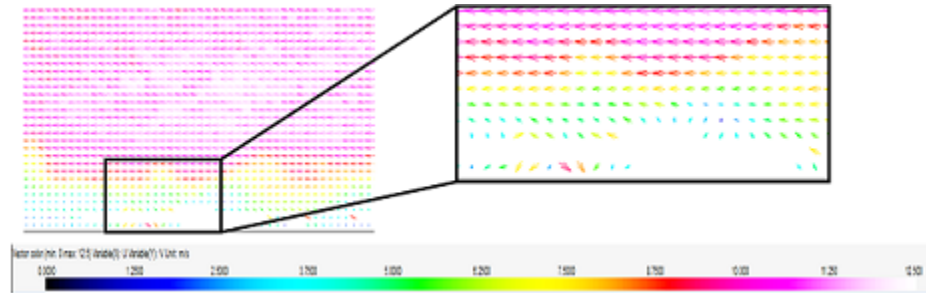


Figure 4.21: Processed vector statistics map of olive oil test with expanded view of boundary layer

Helium Filled Soap Bubbles

HFSB was the final seeding type tested. The FlowSense® CM 12M-70 dual-framing CMOS camera was set to 25 Hz with the aperture set at f/2.5. The HFSB generator was only capable of producing a limited number of neutrally buoyant HFSB at a time. This resulted in less than 10 bubbles visible at any given point in time inside the FOV as seen in Figure 4.14. Due to the limited number of particles in the test section, the system was not able to capture enough data for the entire test area under the same conditions as the previous two seeding options.

To increase the amount of data, 400 images pairs were gathered and processed instead of 250. Various methods were utilized to increase the HFSB concentration inside the test chamber without altering the flow physics. This included moving the delivery system inside of the settling chamber. These changes only slightly increased

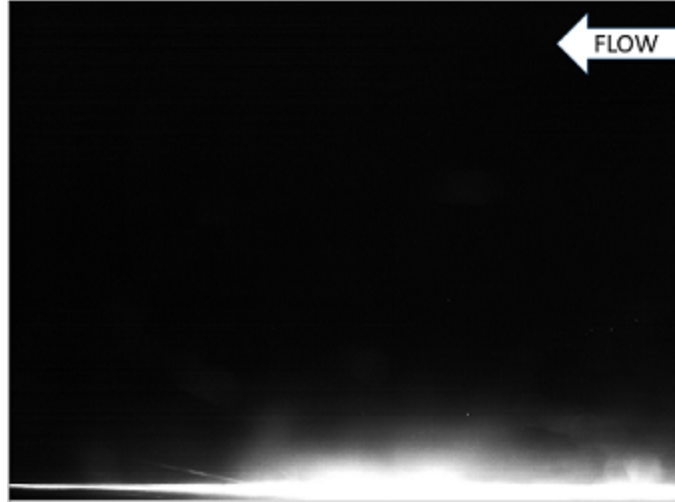


Figure 4.22: Raw data image of empty tunnel helium filled soap bubble test

the number of bubbles visible. Camera aperture settings and time step between images in the image pairs were also modified to determine best combination to increase usable data. Once the images were gathered, they were processed using the adaptive PIV function of Dynamic Studio. The seeding density for HFSB inside the test section was determined to be 0.000 particles per pixel for a majority of the area with 0.001 particles per pixel at locations where HFSB that were visible. The visible HSFB had a mean particle diameter of 3.1 pixels.

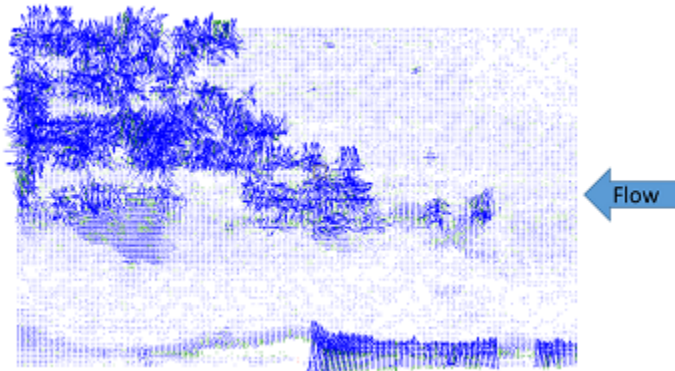


Figure 4.23: Processed vector map of empty tunnel helium filled soap bubble test

The variables in the adaptive PIV algorithm were altered several times to determine the best possible processing methods to generate vector maps, to include various interrogation area values as well as filters and image post processing methods. The

final algorithm used a grid step size of 16 by 16 pixels with a minimum interrogation size of 64 by 64 pixels and a maximum interrogation size of 256 by 256 pixels. This resulted in the best vector map possible with the given data sets with an average of 20,424 vectors, 205 rejected vectors and 2122 substituted vectors. Figure 4.23 shows one of the 250 processed vector maps. From the processed vector map it can be seen that a majority of the test area has either 0 velocity vectors, or vectors that exaggerate any movement and are significantly larger than possible for the test conditions due to the lack of usable raw data.

Seeding Determination

The three empty tunnel tests showed that the helium filled soap bubbles, although large and easy to see, produced a very sparse seeding field, which made it an unusable option for the current wind tunnel and test configuration.

The smoke generator supplied an adequate amount of seeding overall, which when processed, produced reliable results within the lower portion of the test chamber. Due to the particles' small size, the system could not track individual particles. A final problem with the smoke generator was its inability to produce a uniform and steady supply of seeding to the entire test section, which resulted in only a portion of the test section being processed for the test.

The larger particles produced by the olive oil seeding generator produced a higher average seeding density and uniform seeding throughout the test area. This resulted in the system being able to capture data on the entire test section consistently throughout the test.

4.4.3 Flow Visualization Results

The wind tunnel was activated using olive oil as the seeding type. The FlowSense® CM 12M-70 dual-framing CMOS camera was set to 25 Hz with the aperture set at $f/4$.

Once the images were gathered, they were processed using the adaptive PIV function of Dynamic Studio. The seeding density inside the test section was determined to be on average 0.054 particles per pixel with a mean diameter of 1.4 pixels. The tested free stream velocity was $11.18 \pm 0.35 \frac{m}{sec}$ which resulted in a Reynolds number of approximately 57,200, which closely matches the previous experimental results in the water channel.

The adaptive PIV algorithm used a grid step size of 16 by 16 pixels with a minimum interrogation size of 32 by 32 pixels and a maximum interrogation size of 64 by 64 pixels. Due to the inconsistencies of the seeding on the outskirts of the image, the image size was reduced from 4000×3000 pixels to 3000×2900 pixels. This also decreased the processing time. No window or filter functions were used to pre-process the data.

For all the planes except the first (near side) plane, a mask was defined and applied over the cube and the tunnel floor as seen in Figure 4.24. Once the mask was defined, the adaptive PIV algorithm allows the "Wall Windowing" function to be chosen under the window/filter settings. The wall windowing applies the mask on the interrogation windows close to a stationary wall and increases the processing accuracy in the regions near the wall. The inaccuracies without the mask arises in the cross-correlation calculations when the geometric center of the interrogation window is different than the center of seeded area. This type of discrepancy is typical when an obstacle is present[146]. The mask only effects the velocity cross-correlation calculations near the boundaries.

The peak validation method can use between zero and three schemes to invalidate vectors. The first is peak height method, which only allows correlation peaks above a certain level to remain. The second is the peak height ratio method which takes the ratio of the two highest correlation peaks and compares it to a predetermined value. The final method is the signal to noise ratio which compares the correlation

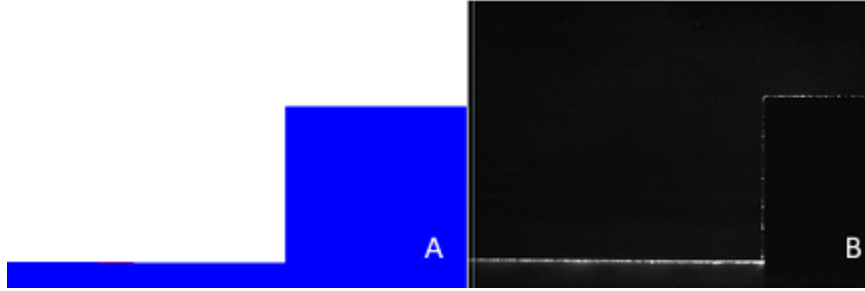


Figure 4.24: Data pre-processing steps; A) define mask and B) apply mask

peak to the noise level and compares this ratio to a predetermined value. If a given vector fails validation, it is rejected. Due to the consistent seeding quality, no peak validation methods were required.

The universal outlier detection detects and substitutes false vectors based on normalized values calculated from neighboring vectors. It was set on a 5×5 pixel neighborhood with a minimum normalization of 0.10 and an acceptance limit of 2.00. After the last iteration, all vectors were validated and substituted vectors added.

The adaptivity of the interrogation area size, which alters the interrogation area based on the number of usable seeding particles inside the area was set to a particle detection limit of 5 with 10 particles desired per interrogation area with a convergence limit of 0.01 pixels for a maximum of 15 iterations.

Each of the test planes ($\Delta x = 10 \text{ mm}$ between planes) produced vector maps with a different number of rejected and substituted vectors. Once the vector maps were completed, they were averaged. The built in "peak ratio" uncertainty analysis method developed by Charonko and Vlachos[132] was utilized to analyze PIV results. This method provides uncertainty for each individual vector. All 250 vector maps were averaged to determine the average error per vector for each plane. Through all eleven planes, the highest uncertainty occurred along the edges of the processed area with an uncertainty of $\pm 0.693 \frac{m}{sec}$. For the processed areas of each plane, the average uncertainty was between $0.146 \frac{m}{sec}$ and $0.310 \frac{m}{sec}$. The average number of vectors for all of the processed planes was 26,384. Table 4.1 shows the number of rejected and

Table 4.1: Vector Map Statistics

Plane Position	Number of Rejected Vectors	Number of Substituted Vectors
-10mm	588	3,292
0mm/ Near Face	1,847	3,246
10mm	2,382	3,229
20mm	2,366	2,788
30mm	2,064	3,445
40mm	1,578	3,520
50mm	2,111	3,242
60mm	1,665	3,409
70mm	2,145	3,328
80mm/ Far Face	2,307	3,414
90mm	3,499	3,361

substituted vectors by plane locations.

Figure 4.25 shows the averaged vector statics map for the near side plane, 10 *mm* away from the side of cube. The cube, which is outlined with the black box is behind the flow, but visible.

The second plane was position at 0 *mm*/near face of the cube. Figure 4.26 shows one of the 250 processed vector maps.

Figure 4.27 shows the averaged vector statics map. From Figure 4.27, the edges of known flow structures/ phenomena such as the (B) top recirculating vortex, (D) rear arch vortex and (C) flow moving up the rear face of the cube are visible. All of these structures were discussed in Chapter 3 of this document. Two additional items of interest is (E) a group of erroneous vectors near the floor and a (A) visible gap in data above the cube. The erroneous vectors on the floor are due to a reflection off the floor which was visible because the camera was not perfectly parallel to the floor. It was later determined that the gap in the data at point (A) was due to mounting hardware on the wall of the wind tunnel reflecting the laser light. This gap in the data is present in all of the vector maps.

The next plane was positioned at 10 *mm* inside the near face of the cube. Figure

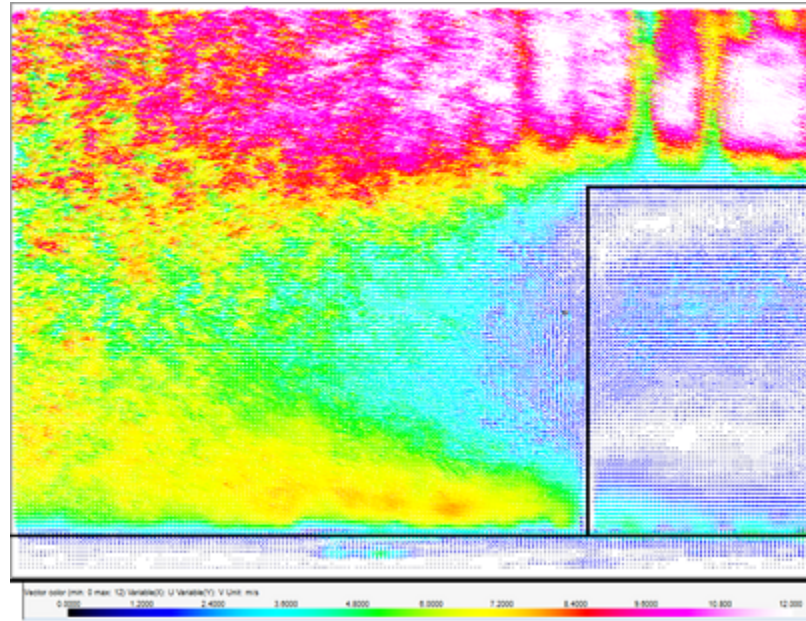


Figure 4.25: Full combined vector map of -10 mm (near side) plane

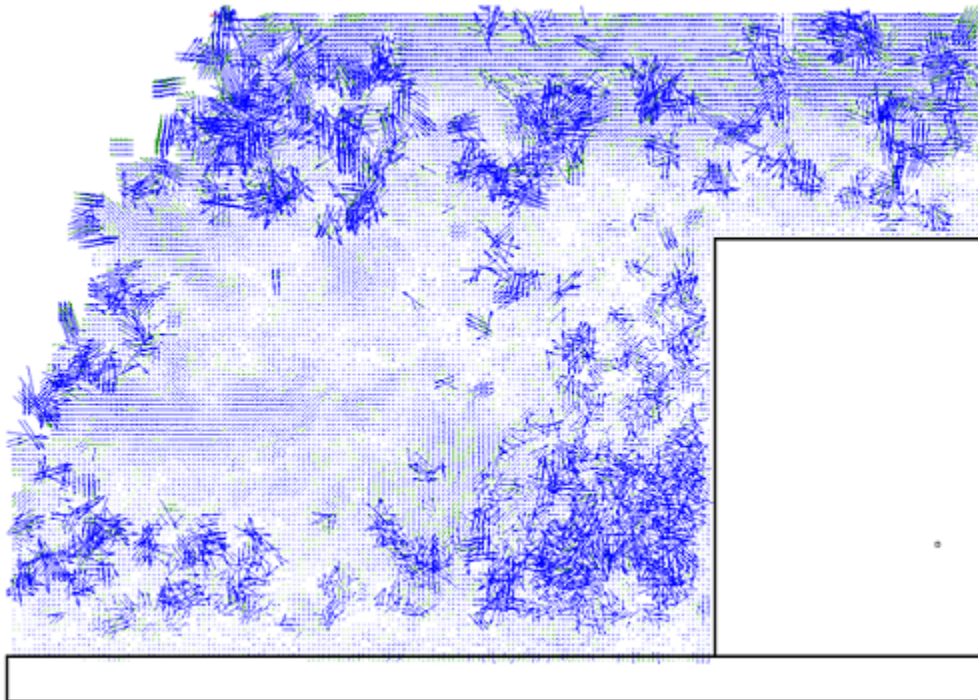


Figure 4.26: Single processed vector map of the 0 mm /near face plane

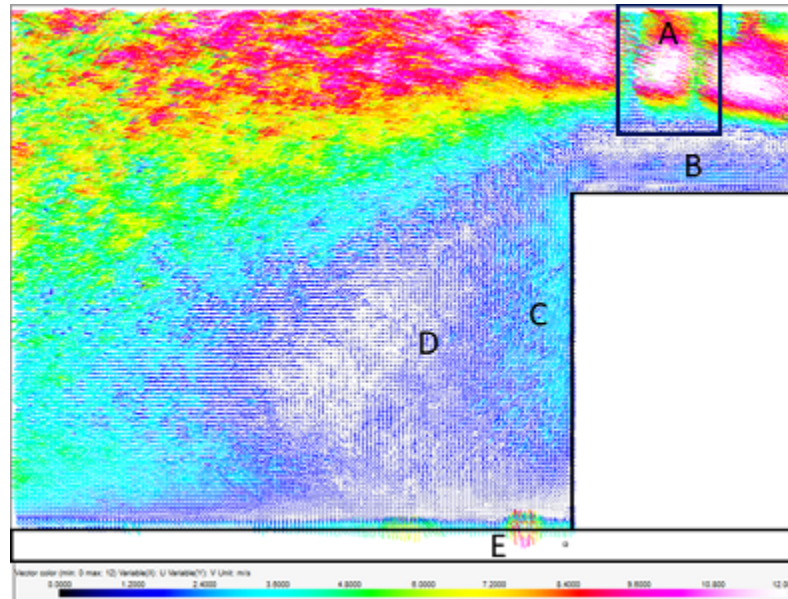


Figure 4.27: Full combined vector map of 0 *mm*/near face showing A) gap in data, B) area of top recirculating vortex, C) flow moving up the rear face of the cube, D) area of rear arch vortex and E) erroneous vectors near floor

4.28 shows the averaged vector statics map of the 250 vector maps produced by the adaptive PIV. Figure 4.28 shows the same known flow structures/ phenomena and items of interest that were present in Figure 4.27.

The fourth plane was positioned at 20 *mm* inside the near face of the cube. Figure 4.29 begins to show a more distinct reverse flow at point (A) and A growing flow separation at point (B). These areas will become more pronounced as the planes approach the center of the cube. The width of the reverse flow region also increases at point (C) as well as the development of a more defined core of the rear horseshoe vortex at point (D).

The next plane was positioned at 30 *mm* inside the near face of the cube. Figure 4.30 shows the same known flow structures/ phenomena and items of interest that were present in previous figures. The reverse flow at point (A) and flow separation at point (B) are well defined. The width of the reverse flow region also increases at point (C) as well as the development of the more pronounced core of the rear horseshoe vortex at point (D). The center point of the cube falls between this plane and the

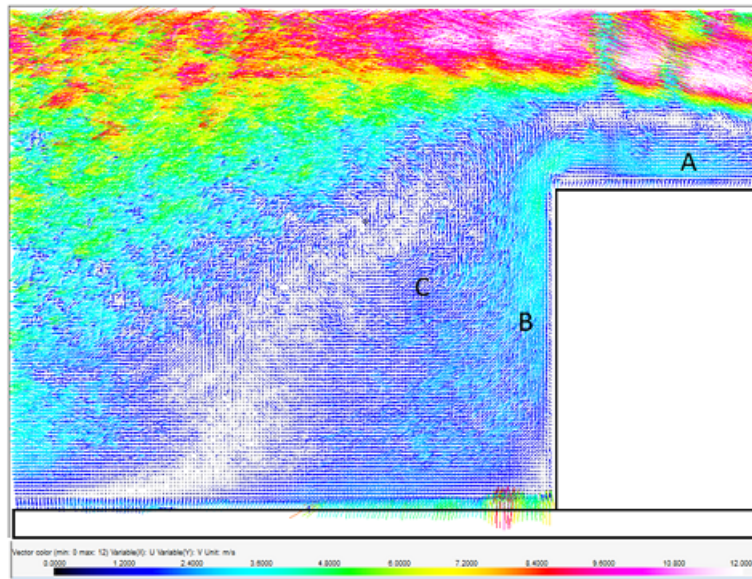


Figure 4.28: Full combined vector map of 10 *mm* from the close edge of the cube showing A) the top recirculating vortex, B) flow moving up the rear face of the cube and C) the rear arch vortex

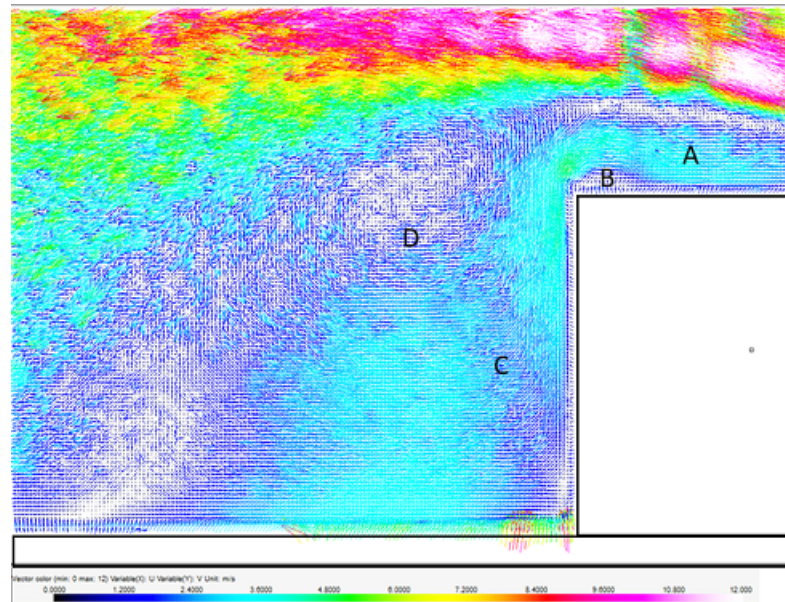


Figure 4.29: Full combined vector map of 20 *mm* from the close edge of the cube showing A) the top recirculating vortex, B) separation region on top rear corner, C) wide area of flow moving up the rear face of the cube and D) core of the rear arch vortex

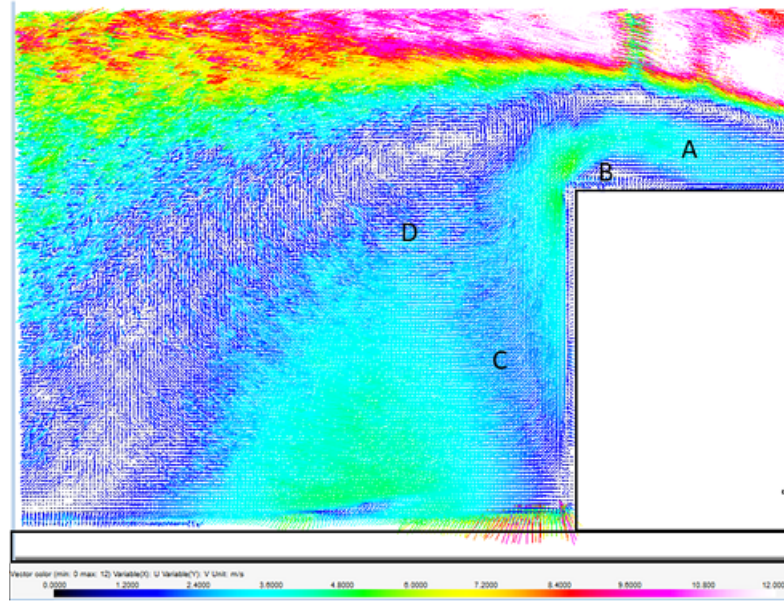


Figure 4.30: Full combined vector map of 30 *mm* from the close edge of the cube showing A) the top recirculating vortex, B) separation region on top rear corner, C) wide area of flow moving up the rear face of the cube and D) core of the rear arch vortex

next plane.

The next plane was positioned at 40 *mm* inside the rear face of the cube. Figure 4.31 is nearly the same as Figure 4.30 due to symmetry around the center point of the cube. Two flow separation points, point (B) on the top rear corner and point (C) on the rear lower face of the cube display a near 0 $\frac{m}{sec}$ velocity. The core/center of the rear horseshoe vortex at point (D) is also near 0 $\frac{m}{sec}$ velocity and like the water channel results is distanced approximately .5H behind the cube.

The seventh plane was positioned at 50 *mm* inside the rear face of the cube. Figure 4.32 is nearly the same as Figure 4.29 due to symmetry around the center point of the cube. The differences exist at point (A) and point (B), where the vectors have a higher density in Figure 4.32 than in Figure 4.29, due to minor fluctuations in the seeding uniformity during the tests.

The next plane was positioned at 60 *mm* inside the rear face of the cube. Figure 4.33 is nearly the same as Figure 4.28 due to its symmetry around the center point

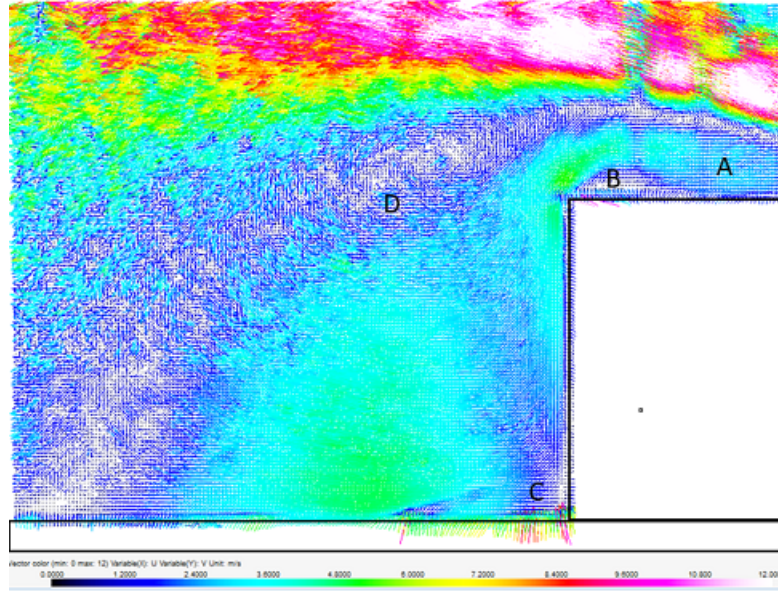


Figure 4.31: Full combined vector map of 40 *mm* from the close edge of the cube showing A) the top recirculating vortex, B) separation region on top rear corner, C) near 0 velocity area at base of cube and D) center of the core of the rear arch vortex

of the cube with the same differences in vector density at point (A) and point (B). As the planes move across the cube, it can also be seen that the wall windowing algorithm appears to be having more difficulty near the surface of the floor and the cube, due to the camera being slightly off level during data acquisition.

The ninth plane was positioned at 70 *mm* inside the near face of the cube. Figure 4.34 is similar to Figure 4.28. There are minor differences in vector density at point A) and point B) as well as a low velocity region spanning from point (b) to the right rear corner of the cube where a group of erroneous vectors are visible.

The next plane was positioned at 80 *mm*, which is the far face of the cube. Figure 4.35 is similar to Figure 4.27 due to symmetry around the center point of the cube with the same differences in vector density illustrated in previous images. The extreme far edge of the (A) top recirculating vortex and decreased intensity leg of the (C) rear arch vortex can also be seen.

The final plane was positioned at 90 *mm* or 10 *mm* beyond the far face of the cube. Figure 4.36 shows the A) separation around the top and rear of the cube on

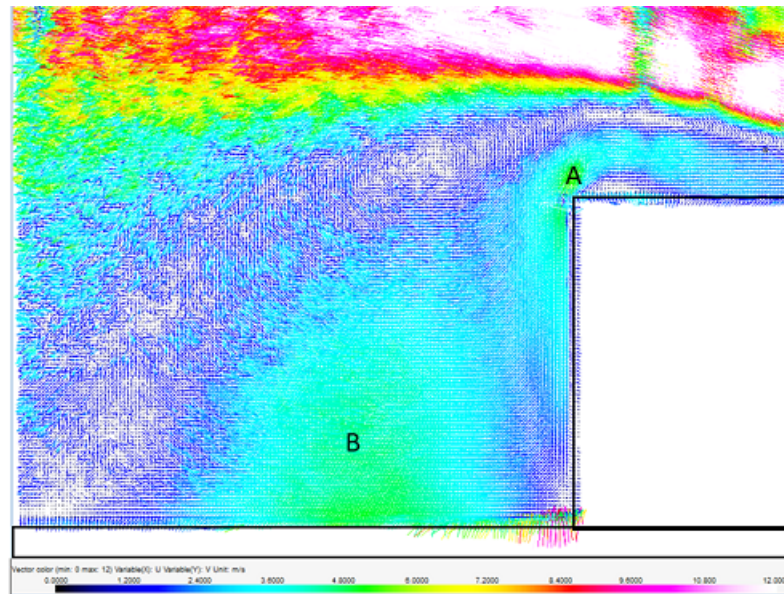


Figure 4.32: Full combined vector map of 50 *mm* from the close edge of the cube showing higher vector concentrations at the A) flow separation point on top edge and B) in the rear horseshoe vortex

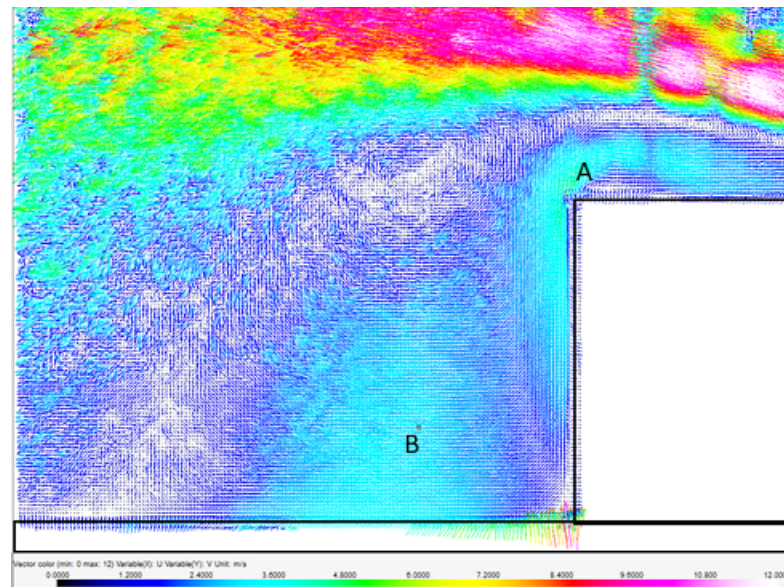


Figure 4.33: Full combined vector map of 60 *mm* from the close edge of the cube showing higher vector concentrations at the A) flow separation point on top edge and B) in the rear horseshoe vortex

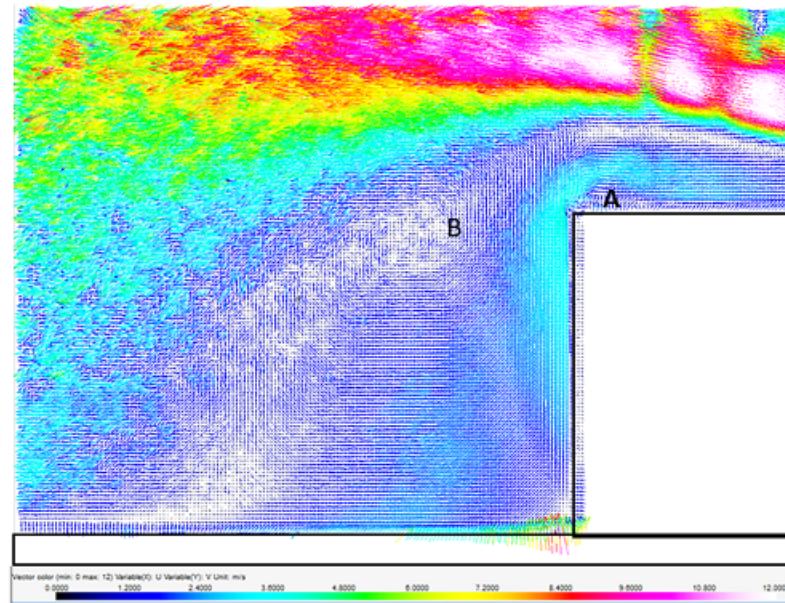


Figure 4.34: Full combined vector map of 70 *mm* from the close edge of the cube showing higher vector concentrations at the A) flow separation point on top edge and B) in the rear arch vortex

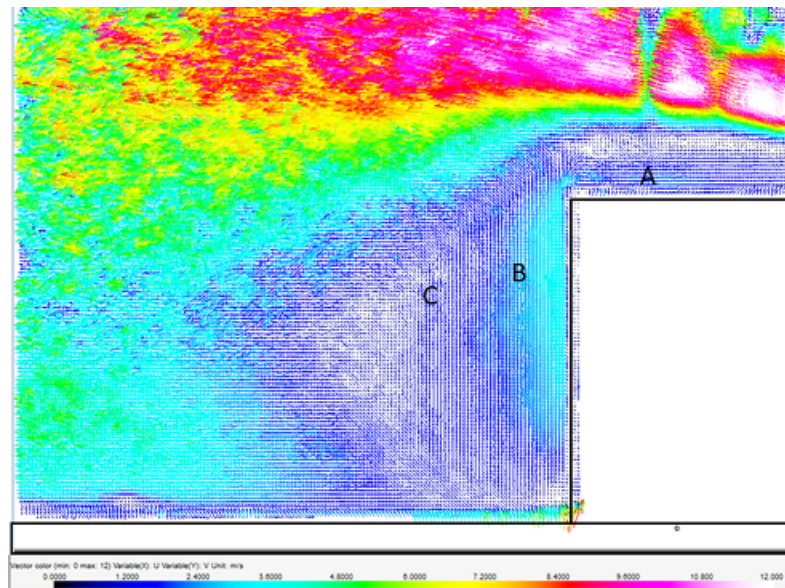


Figure 4.35: Full combined vector map of 80 *mm*/far face showing A) area of top recirculating vortex, B) flow moving up the rear face of the cube and C) area of rear arch vortex

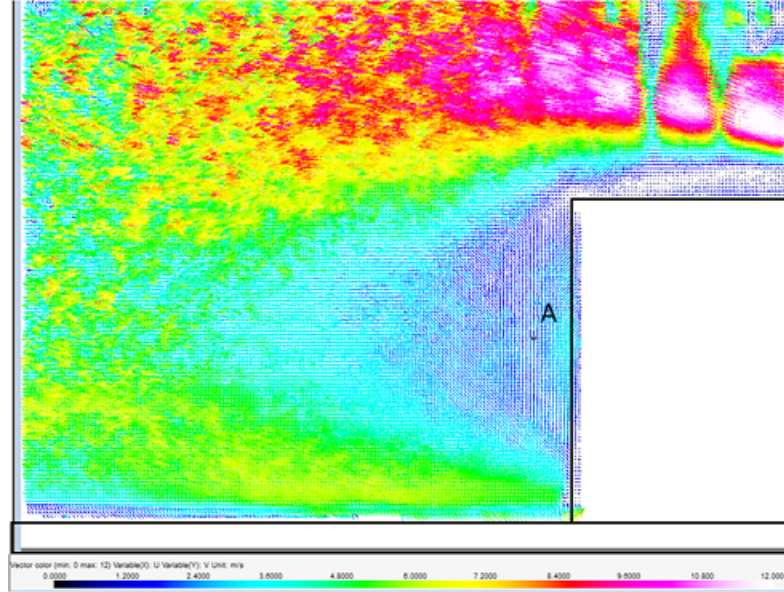


Figure 4.36: Full combined vector map of 90 *mm* with A) separation area along top and rear of cube

the far side.

To make the vector direction and magnitude more easily identifiable from Figures 4.25 to 4.36, the number of vectors in each vector map was decreased by selecting to leave every third vector visible. The vector head size was also increased .5 and the vector length increased to 2.5. Figure 4.37 shows the reduced vector density map for the plane 10 *mm* off the near side of the cube.

Figure 4.38 shows a reduced vector map of the 40 *mm* near center plane. With the number of vectors reduced, key structures are more easily identifiable such as A) the rotating core of the rear horseshoe vortex and (B) the reverse flow moving up the rear face of the cube. From this scale and magnification, the circular flow at point (A) can be seen and approximately $0.10U_{\infty}$ which is the same value reported in the water channel tests. The reverse flow up the rear face of the cube in area (B) feeds the recirculation vortex on the top of the cube. The velocity here is between $0.30U_{\infty}$ and $0.50U_{\infty}$, which is slightly higher than the measurements reported in the water channel tests.

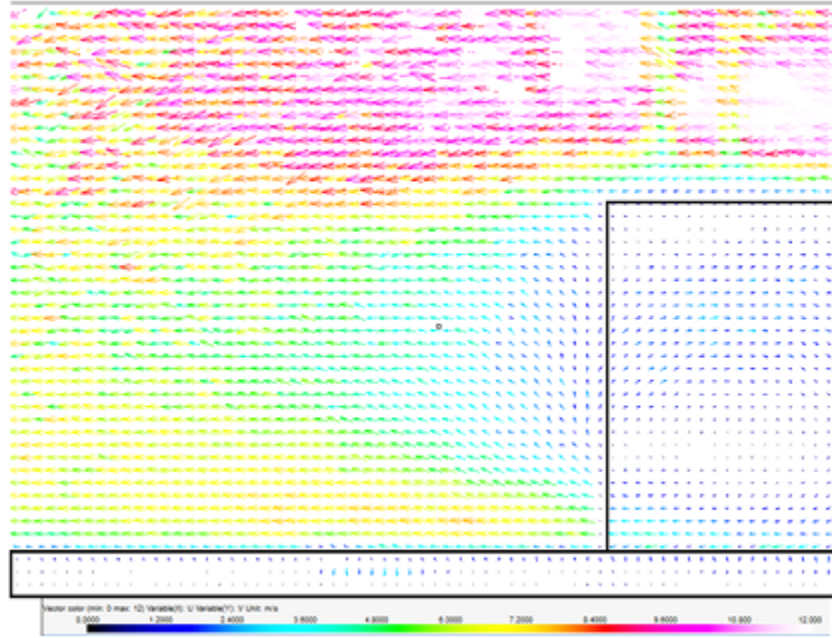


Figure 4.37: Reduced density combined vector map of -10 mm (near side) plane

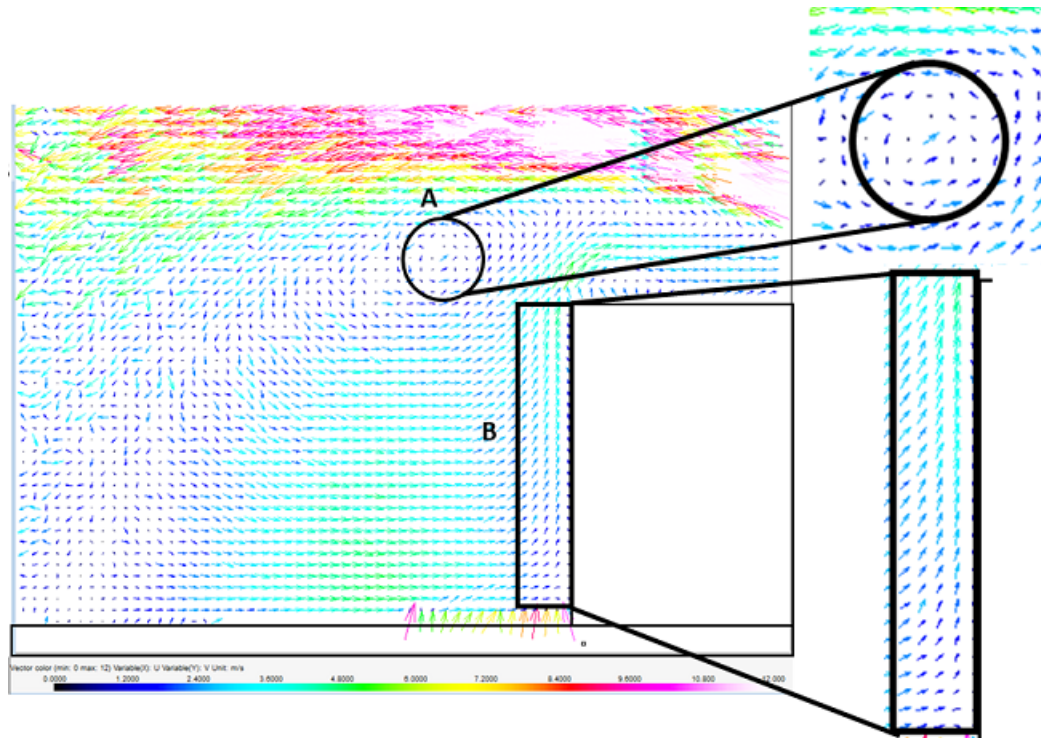


Figure 4.38: Reduced density combined vector map of 40 mm plane showing A) core of rear horseshoe vortex and B) reverse flow region along rear of cube

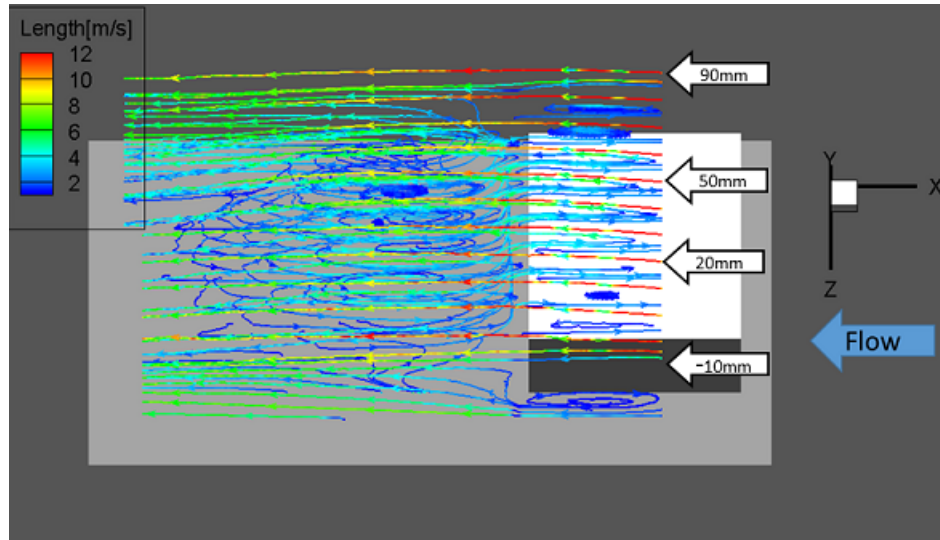


Figure 4.39: Tecplot image with eleven planes inserted

All of the individual vector maps were then imported into Tecplot to produce a volume from the combined planes as seen in Figure 4.39. The locations of the near side (-10 mm), far side (90 mm) and two middle (20 mm and 50 mm) planes are identified. Although not as smooth and continuous as those images presented in Section 3.4 which were imported as a single volume, the images with imported planes can be used to easily identify flow structures, directions and magnitudes. Figure 4.39 makes it appear as though streamlines are moving between planes, which is an not possible and is a byproduct of the angle of the image.

Figure 4.40 shows the complete volume of the eleven PIV tests as seen from above. From this combined view, three primary structures are visible, (A) the top recirculating vortex, (B) the side recirculating vortex and (C) the rear arch vortex.

Figure 4.41 shows the complete volume of the eleven PIV tests as seen from the near side of the cube. From this view, the size of the rear arch vortex (C) is determined to be approximately one cube length wide and spans the region starting slightly off the rear face of the cube. The reverse flow of the rear face of the cube separates the rear horseshoe vortex from the cube. The height of the rear horseshoe vortex is approximately $1.3H$ in the wind tunnel where it was only slightly above height of $1H$

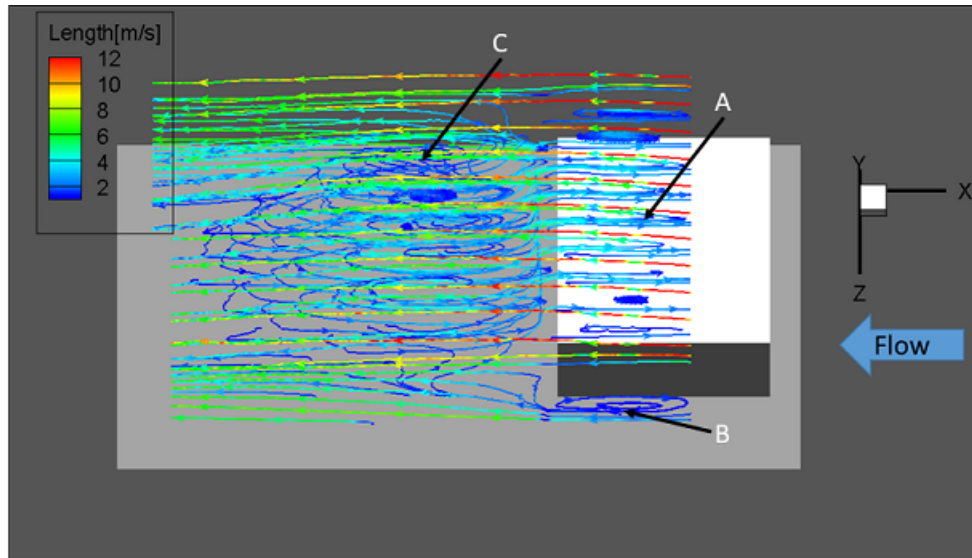


Figure 4.40: Flow of combined vector planes as seen from the top showing A) top recirculating vortex, B) side recirculating vortex and C) rear arch vortex

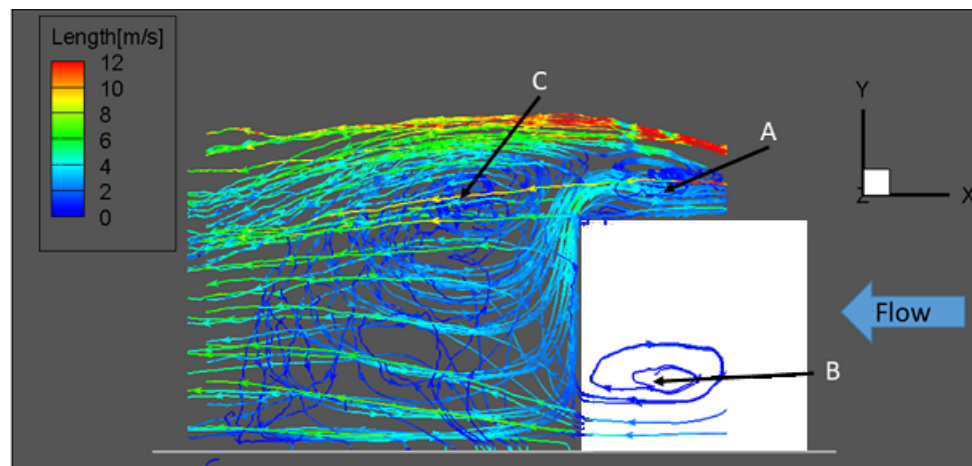


Figure 4.41: Flow of combined vector planes as seen from the top showing A) top recirculating vortex, B) side recirculating vortex and C) rear arch vortex

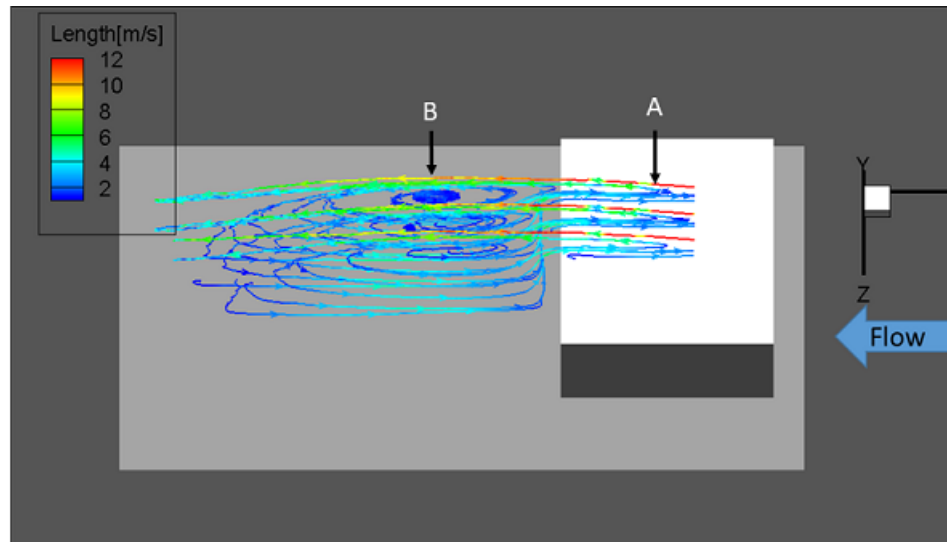


Figure 4.42: Flow of combined center three vector planes as seen from the top showing A) top recirculating vortex and B) rear arch vortex

in the water channel. A large reverse flow region up the rear face of the cube feeds the top recirculating vortex (A). The side recirculating vortex (B) is visible but does not provide much detail due to its close proximity to the edge of the tested region. Figure 4.41 also shows that the free stream velocity is maintained at a distance of approximately $0.5H$ above the cube.

By removing specific planes from Figure 4.40, it is possible to get a clearer view of specific regions or planes of interest as seen in Figure 4.42. Figure 4.42 shows the location of the core of the (A) top recirculating vortex and the (B) rear horseshoe vortex along the center of the cube. The cores of the formations appear to be in the nearly identical locations as those observed in the water channel.

Figure 4.43 shows the center three planes from the side. The reverse flow around the corner of the (A) top recirculating vortex is visible. The core itself is positioned farther to the rear of the cube than was observed in the water channel. The largest difference between the flow structures present in the water channel and the wind tunnel is visible at point (B). At this location the reverse flow up the rear face of the cube completely separates from the cube and leaves a large area that appears to

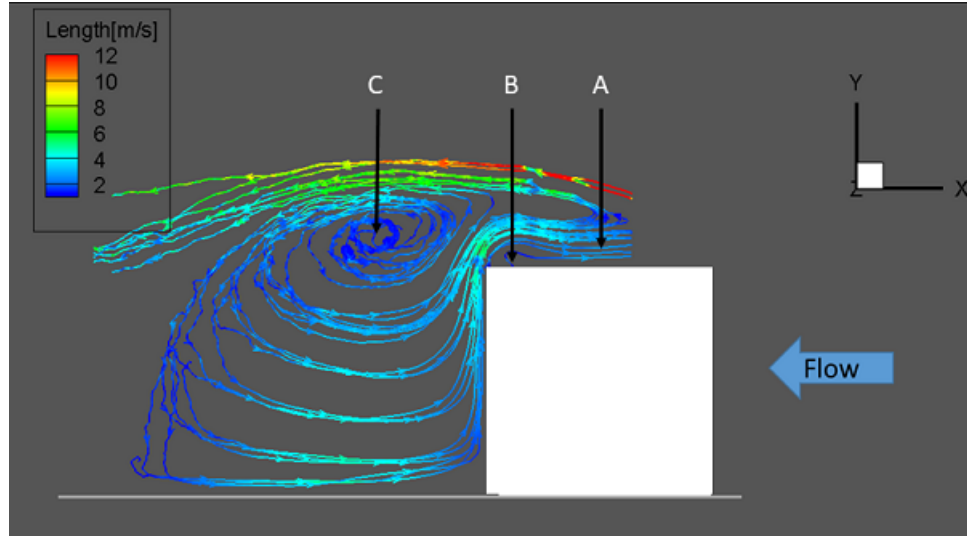


Figure 4.43: Flow of combined center three vector planes as seen from the side showing A) top recirculating vortex B) separation zone and C) rear arch vortex

be void of movement. In the water channel there was insignificant separation in this area. Another difference as described earlier is that the core of the (C) rear horseshoe vortex is higher into the flow than witnessed in the water channel. Additionally, the structure itself is much wider and does not hold the same symmetry. The velocities inside the core of the two structures visible is less than $0.15U_{\infty}$ which is slightly higher than the values seen in the water channel. The reverse flow up the rear face of the cube is approximately $0.35U_{\infty}$ which is again, slightly higher than those values observed in the water channel.

4.4.4 Comparison between water channel and wind tunnel results

A brief side by side comparison was conducted to show the differences between first the images produced by the two PIV options used and second the differences between the two median used. Some minor differences in the images may be attributed to the data transfer and model placement in Tecplot.

Figure 4.44 shows the wind tunnel (top) and the water channel (bottom) streamline maps from the side of the cube. The axis between the two images vary due to

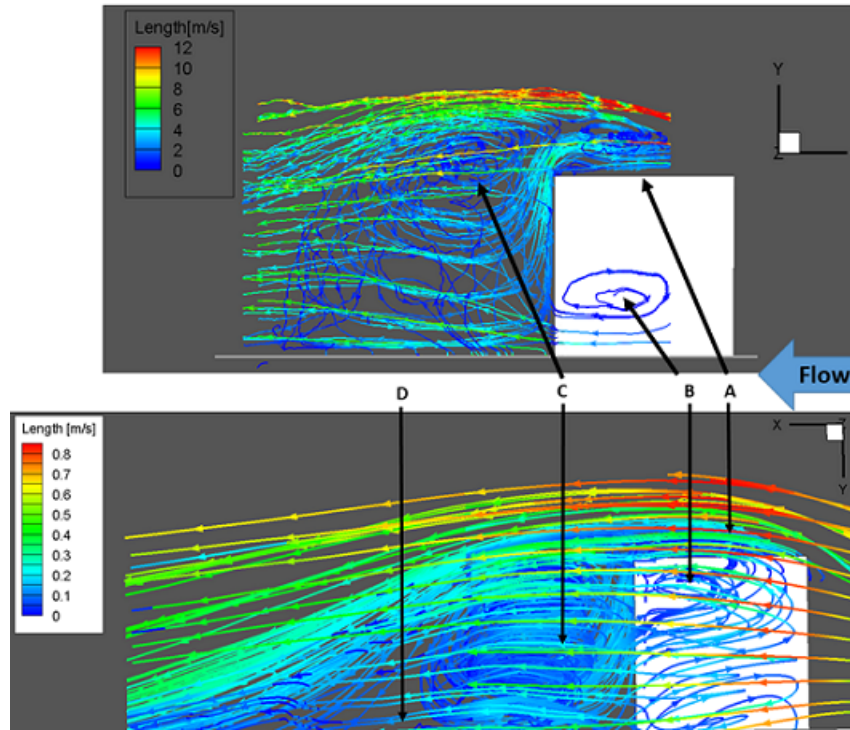


Figure 4.44: Comparison of wind tunnel (top) and water channel (bottom) combined streamline maps showing A) top recirculating vortex B) side recirculating vortex, C) rear arch vortex and D) trumpet (horseshoe) vortex

their orientation during testing (water channel model was hung upside down in the flow as detailed in Chapter 3) and the velocities vary to achieve similar Reynolds numbers. The water channel processed maps produced a larger overall test volume in both length and width. To increase the length of the water channel test volume seen in Figure 4.44, a second downstream volume was stitched into the original results beyond the rear horseshoe vortex (Where the point (D) is identified) to show the downstream reattachment region. Each individual plane was added for the wind tunnel to produce the volume shown. The individual planes were not stitched together and do not produce a complete smooth image of the volume like the water channel results.

When comparing the results presented in Figure 4.44, the top recirculating vortex (A) is visible in both images. The first major difference between the two images is the ease of recognizing the position of the vortex in the wind tunnel image. Because

the water channel was processed as a volume, the outside flow and top of the side circulating vortex from this orientation mask some of the top circulating vortex shape and magnitude. The free stream flow in both images is at approximately $0.3H$ above the cube and is the upper boundary of the test volume.

The side recirculating vortex (B) is clearly visible in the water channel (bottom) image, but only a single circulation on the lower half of the cube is visible in the wind channel (top) image. This is due to only a single plane tested on the outside $10mm$ edge of the wind tunnel cube while the water channel test volume extended nearly $20mm$ past the edge of the cube. Despite this difference, the structure in the wind tunnel image is consistent in size, location and direction with the structure visible at the same height in the water channel image.

The rear arch vortex (C) is easily recognizable in the water channel image. It is also visible in the wind tunnel image, just not as well defined. The location and the height of this structure also differs between the two images. The structure in the water channel image is approximately the same height as the cube and its core is located $0.5H$ behind the cube. The top of the structure is contained by the free stream flow, which separated at the front face of the cube and moves downward to reattach to the floor downstream of the cube. In the wind tunnel test, the separation over the cube continues to grow and does not return to reattach as quickly as it does in the water channel image. This extended separation region allows for the core of the horseshoe vortex to be $1.25H$ tall. The structure also appears to be slightly wider in the wind tunnel.

The trumpet arch (D) is only barely visible in the water channel image on the bottom.

To better visualize the top recirculating region (A), the rear reverse flow region (B) and the cube width portion of the rear arch vortex (C), the near side plane was removed from the wind tunnel image and the vectors outside of the width of the cube

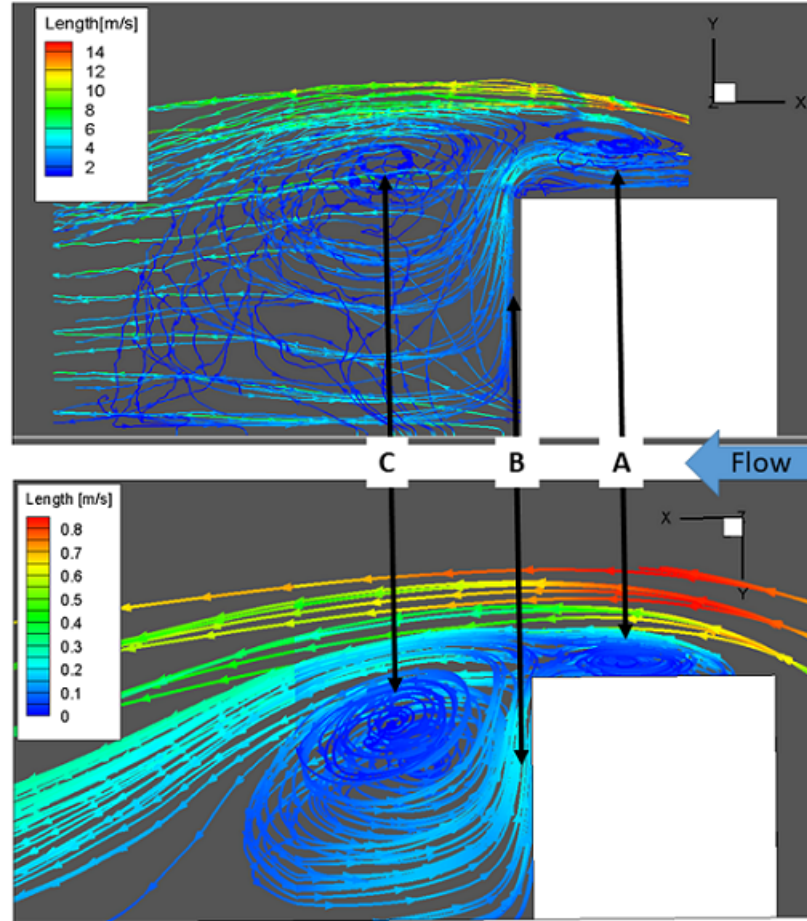


Figure 4.45: Comparison of wind tunnel (top) and water channel (bottom) combined streamline maps (cube width) showing A) top recirculating region B) reverse flow region and C) rear arch vortex

were hidden in the water channel image. Figure 4.45 shows the reduced volume and again shows that the TomoPIV volume produced more uniform streamlines than the combined planes did with the 2D PIV system, particularly in the rear arch vortex area. The locations of the rear arch vortex (C) and top recirculating vortex are (A) clearly defined. The direction of the flow up the rear face of the cube is also more easily traceable.

Figure 4.46 shows a close up view of the top recirculating vortex for the wind tunnel (top) and water channel (bottom). Although both images show the core of the vortex has a velocity of $< 0.15U_\infty$, the position of the core with respect to the

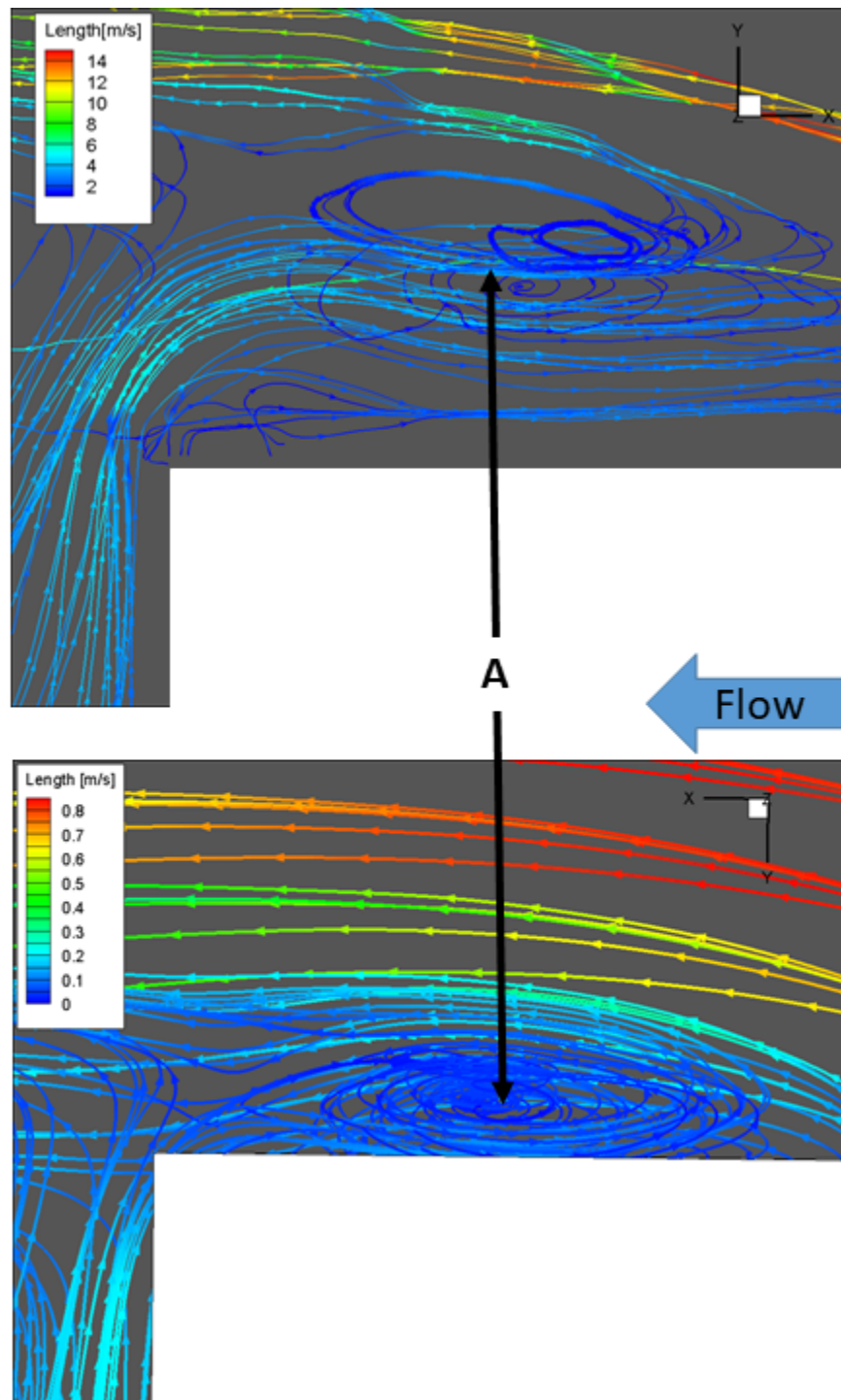


Figure 4.46: Comparison of wind tunnel (top) and water channel (bottom) combined streamline maps showing the top recirculating region

height above the cube is different. The vortex appears to be centered on the width of the cube and slightly behind the center of the top face in both images.

The wind tunnel image on the top shows the reverse flow traveling up the rear face of the cube at approximately $0.35U_\infty$ and separating sharply at the top rear corner of the cube. The flow does not approach the top face until nearly the center of the cube. The flow from the front face of the cube also separates sharply outside the test volume. This separation region is visible as the higher velocity stream lines towards the top of the image. The core of the top recirculating vortex is directly above the rear separated reverse circulation flow. This puts the core of the top recirculating vortex approximately $0.25H$ above the cube.

The water channel image on the bottom shows the reverse flow moving up the rear face of the cube at approximately $0.35U_\infty$. The major difference here is the reverse flow stays closer to the cube with little or no separation as it approaches the top rear face of the cube. The separation from the front top edge of the cube (not visible in image) produces a more pronounced, compact set of stream lines which are easily traceable from the upstream side of the image. The core of the top recirculating vortex appears to be compressed against the top face of the cube by the front separated flow. This puts the core approximately $0.125H$ above the cube.

Figure 4.47 shows a close up view of the rear arch vortex for the wind tunnel (top) and water channel (bottom). As with previous images, there are many general similarities and a couple differences. The core of the rear arch vortex is visible in both images and appears to be circulating at $< 0.15U_\infty$. The position of the core with respect to the height of the cube is different as is the total width of the structure.

The wind tunnel image on the top shows a complete view of the reverse flow traveling up the rear face of the cube at between $0.15U_\infty$ and $0.35U_\infty$. The arch vortex is visible, but chaotic due to large out plane motions not captured by the PIV system. The core of the arch vortex is $0.5H$ directly behind the cube and slightly

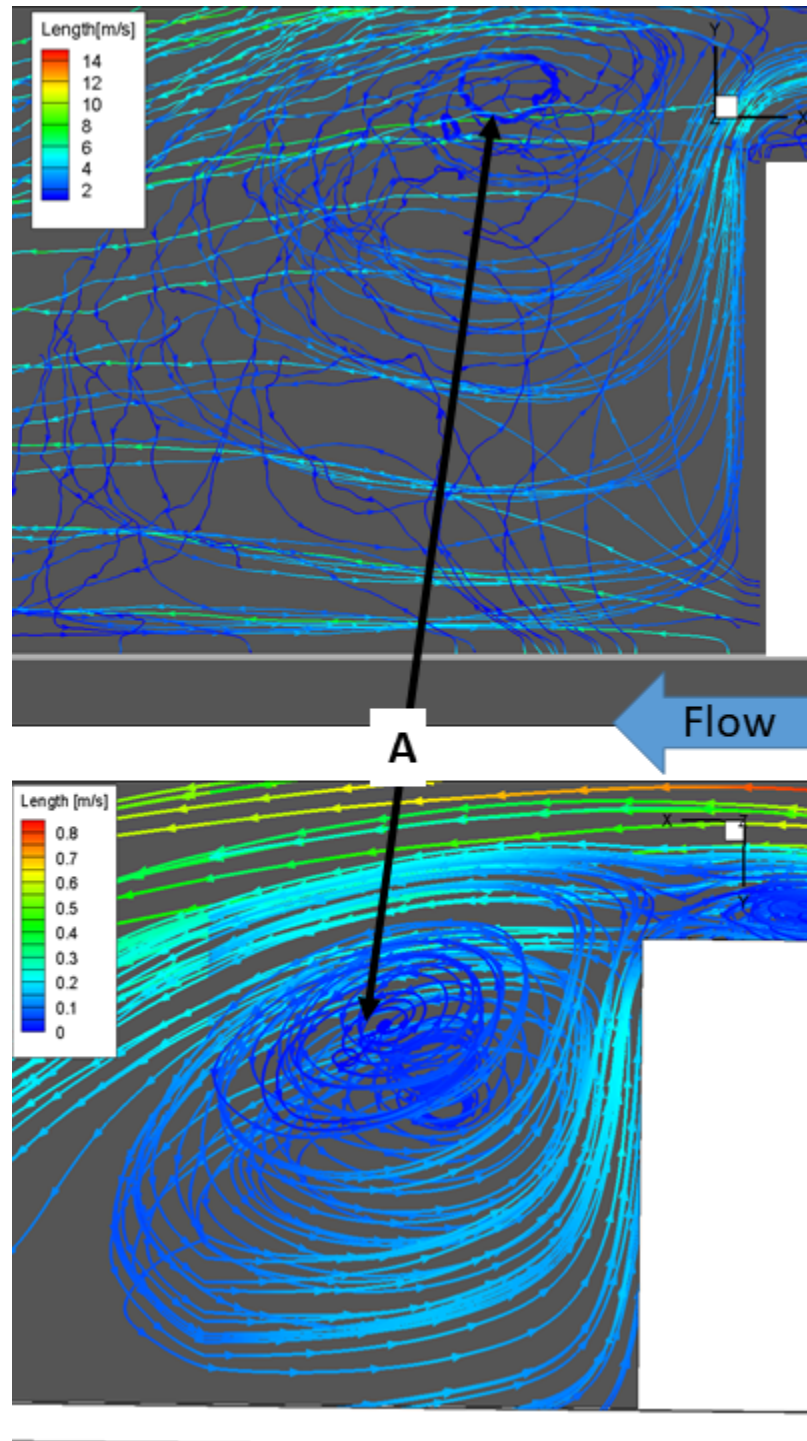


Figure 4.47: Comparison of wind tunnel (top) and water channel (bottom) combined streamline maps showing the rear arch vortex

above the top face of the cube. The overall width of the structure is slightly larger than the width of the cube.

The water channel image on the bottom shows the same reverse flow moving up the rear face seen in previous figures. The core of the vortex is better defined and individual streamlines can be traced through the recirculation. The change in velocity from the core can also easily be traced as it increases from $< 0.15U_\infty$ at the core to approximately $0.35U_\infty$ as it proceeds up the rear face of the cube. The streamlines closest to the cube separate slightly and join the top recirculating vortex where the ones farther away from the cube either remain in the rear arch vortex or join the flow just under the free stream and proceed downstream.

4.4.5 Pressure and Correlation Results

Raw Pressure Data

The raw pressure data was separated into three regions for processing, i) upstream in front of the cube, ii) cube walls and iii) wake region behind the cube. The pressures depicted are the differential pressures, which are the difference between the pressure at that location and the ambient pressures (101.325 kPa). Figure 4.48 shows the raw data for the region in front of the cube for the first 5 seconds of the experiment. The red line depicts the differential pressures acquired at $1H$ in front of the cube and the blue line depicts the pressures acquired at $0.5H$ in front of the cube.

Figure 4.49 shows the data for the region in front of the cube for the first 5 seconds of the experiment after it was filtered using the MATLAB code in Appendix A.2.

Figure 4.50 shows the raw data for the pressures on the walls of the cube for the first 5 seconds of the experiment. The red line depicts the differential pressures acquired on the front face and blue line shows the rear pressures. The right side is cyan, the top is green and the left side is purple.

Figure 4.51 shows the data for the region in front of the cube for the first 5 seconds of the experiment after it was filtered using the MATLAB code in Appendix

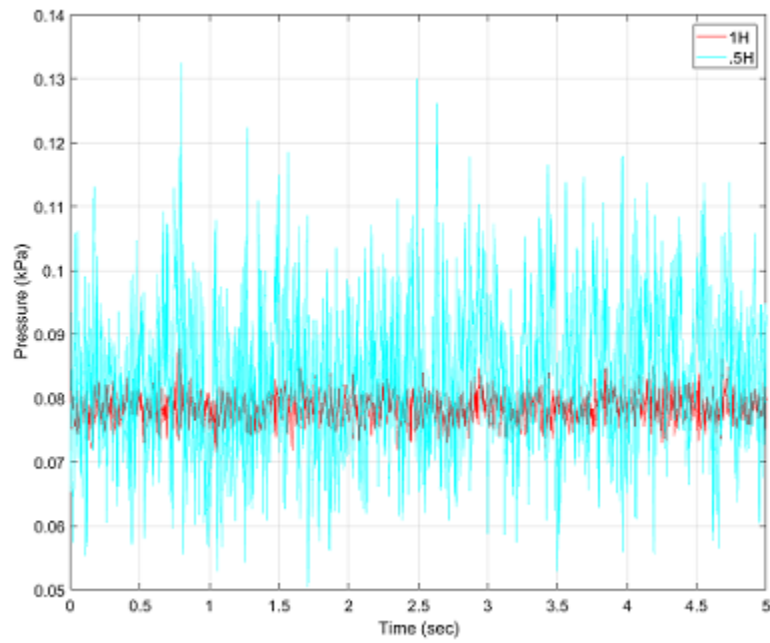


Figure 4.48: Raw pressure data in region upstream in front of the cube

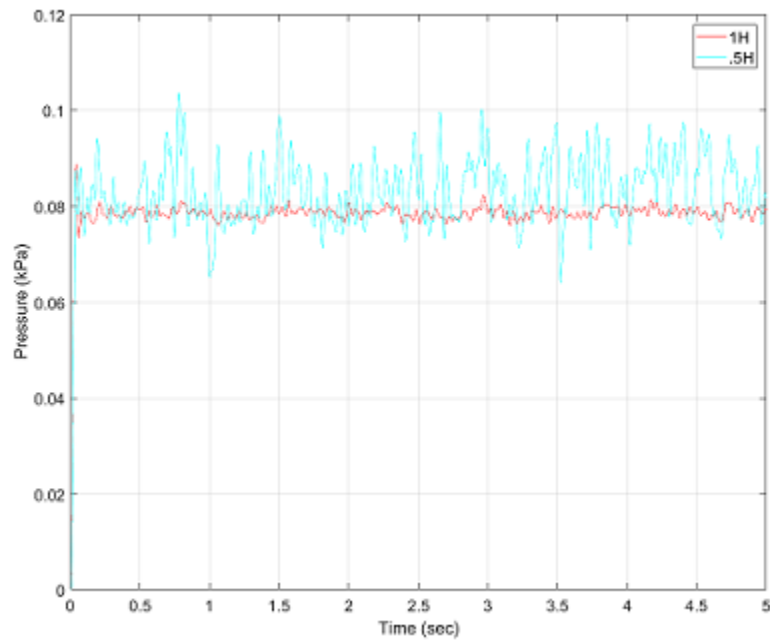


Figure 4.49: Filtered pressure data in region of upstream in front of the cube

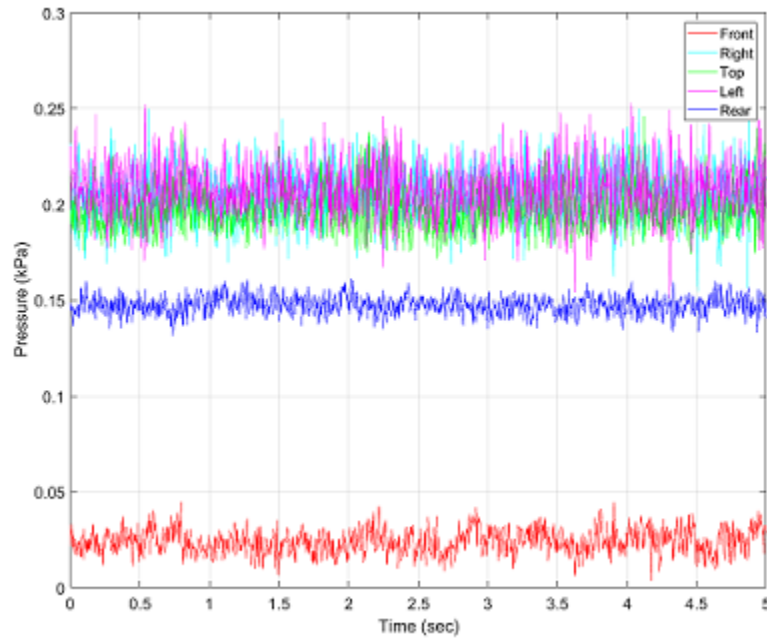


Figure 4.50: Raw pressure data on the walls of the cube

A.2. From Figure 4.51 it can be seen that the front face (red) is near ambient, or the lowest overall pressure difference. It also shows that the sides and top are all near the same value.

Figure 4.52 shows the raw data for the pressures in the wake region behind the cube for the first 5 seconds of the experiment. The red solid line shows the differential pressures acquired at $0.5H$ behind the cube. The legend on Figure 4.52 shows the different colors for each Δx from $0.5H$ to $4H$ behind the cube.

Figure 4.53 shows the data for the region in the wake region behind the cube for the first 5 seconds of the experiment after it was filtered using the MATLAB code in Appendix A.2. From Figure 4.53 it can be seen the pressure differences is greatest at the location closest to the cube (red solid line) and that the pressure difference becomes less the farther away from the cube the sensor is placed. From a distance of $2H$ (pink solid line) to $4H$ (red dashed line) the pressure differences are nearly identical for each distance at approximately 0.12 kPa .

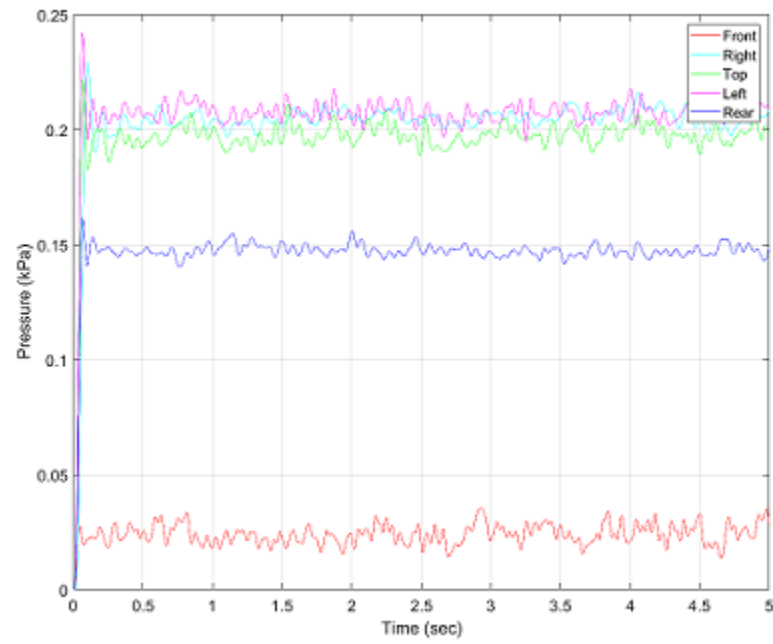


Figure 4.51: Filtered pressure data on the walls of the cube

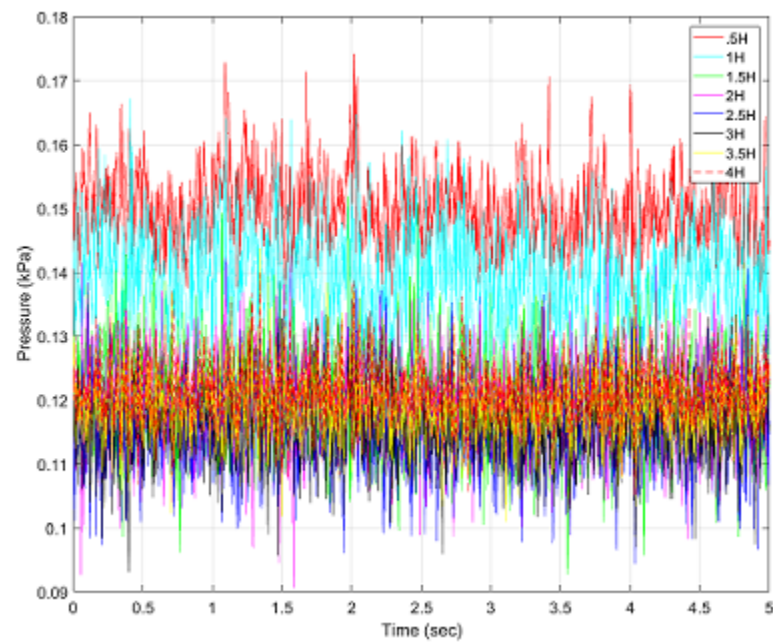


Figure 4.52: Raw pressure data in wake region of cube from 0.5H to 4H

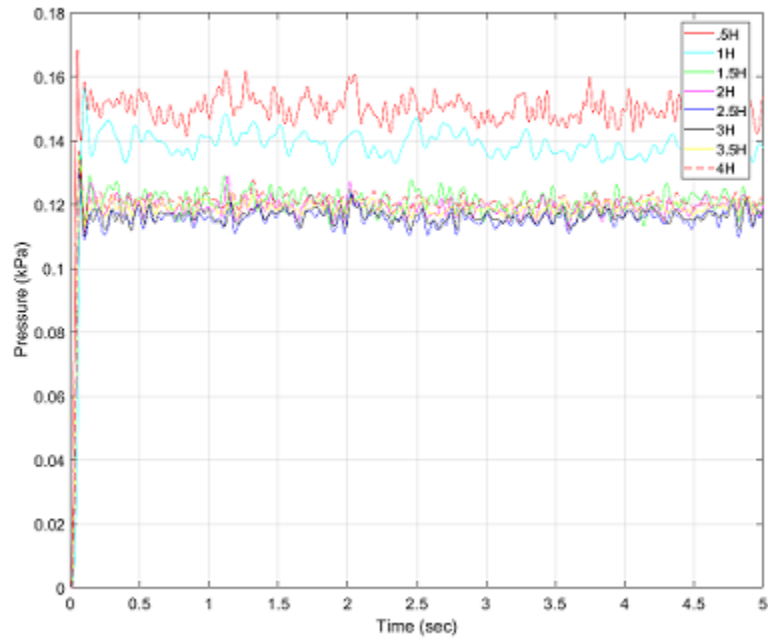


Figure 4.53: Filtered pressure data in wake region of cube from 0.5H to 4H

Sensor Location	Magnitude	Number of Lags
A	0.5535	124
B	0.3825	128
Top	0.4261	153
Rear	0.5119	137
Front	0.4081	134
Right	0.4155	134
Left	0.4036	134
H	0.4740	114
I	0.3390	125
J	0.3125	127
K	0.3088	128
L	0.3524	125
M	0.4030	125
N	0.3621	126
O	0.4223	117

Autocorrelation

All of the pressure sensor data was first autocorrelated using a built in autocorrelation function in MATLAB[®] to determine if there was any oscillatory behavior in the data and determine the duration of that behavior. A magnitude of 1 would signify a perfect or oscillatory reading while a magnitude of 0 would indicate no correlation or repeatable behavior. The number of lags is the amount of time between the repetitions. Table 4.2 shows the results of the autocorrelation. The horizontal lines across the table separate the regions in the test section with sensor A and B in front of the cube and sensors H-O behind the cube. In the region in front of the cube, the magnitude of the correlation decreases and the time step (number of lags) increases the closer to the cube the sensor is. The region behind the cube starts with a high magnitude of correlation and decreases as the sensor distance increases from the cube out to $2H$. The front, right, left and top of the cube all have similar magnitude values while the rear is significantly larger.

Figure 4.54 shows a graph of the number of lags by location of the autocorrelation. As stated previously, the number of lags increases slightly as the sensors approach the cube from the front. As the sensor position increases in distance away from the cube on the rear side, the number of lags increase up to a distance of $2H$. On the cube, the front, right and left sides all have identical values while the rear is slightly higher and the top sensor has the highest number of lags.

Pre and Post Cube Cross-Correlations

All of the pressure sensor data was then broken up into regions: i) in front of cube, ii) cube and iii) behind the cube. A cross-correlation was conducted with all of the sensors in the region using a built in cross-correlation function in MATLAB[®]. The cross-correlation measures the similarity between one data point and a time

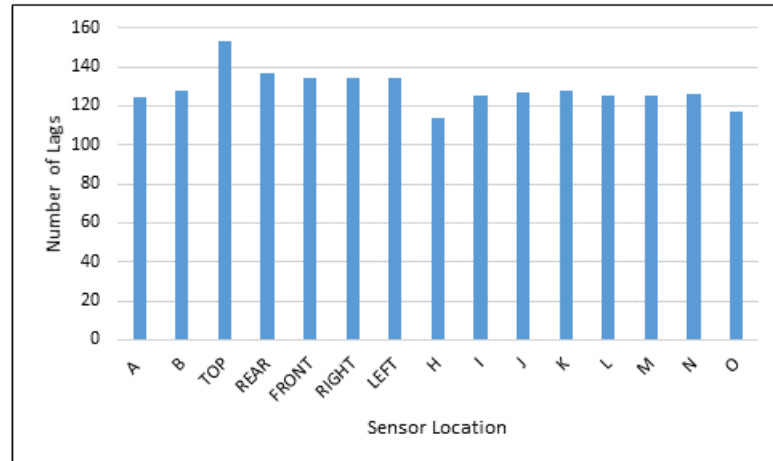


Figure 4.54: Number of lags in autocorrelation based on location for pressure data

shifted data point in a second set of data. Similar to autocorrelation, a magnitude of 1 would signify a perfect correlation while a magnitude of 0 would indicate no correlation. Typically a magnitude of above than 0.8 would be strongly correlated and those magnitudes less than 0.2 would be weakly correlated and values less than 0.1 would not be reported. In the free stream region above the boundary layer, it would take approximatively 0.0034 seconds (34 lags) to travel between the sensors at $11.1 \frac{m}{sec}$. The negative sign that appears on some of the lags are demonstrating a negative time step. The cross-correlation between any two sensors demonstrate symmetry so if one sensor shows a positive lag, the other in the pair would show a negative lag at the same magnitude.

Figure 4.55 is the cross-correlation graph between sensor A and sensor B in front of the cube for the first 30,000 sensor readings. Any peaks on the graph above 0.09 were recorded as seen in Table 4.3. Only one value was above 0.2, which occurred at 59 lags, or 0.0059 seconds ($5.9ms$). This demonstrates that there is a degree of similarity between two sensors, which could represent the movement of a flow structure inside the boundary layer that is traveling at approximately $6.5 \frac{m}{sec}$ as it approaches the cube.

The data for the cross-correlations for the wake region behind the cube are avail-

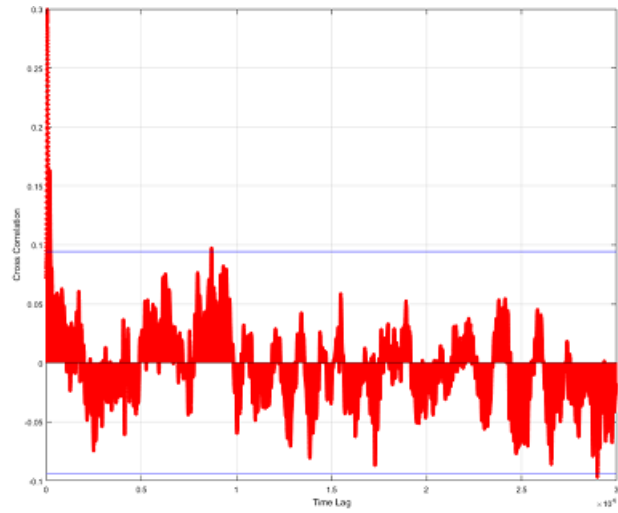


Figure 4.55: Cross-correlation graph between sensors A and B in front of the cube for the first 30,000 data points

Table 4.3: Cross-Correlation between Sensors A and B

Magnitude	Number of Lags
0.2994	59
0.0974	8696
0.0968	28996

able in Appendix A.4. Table A.1 in Appendix A.4 shows all sensors cross-correlation with sensor H (38.1 *mm* behind the cube). This area, as seen in Figure 4.43 is directly under the rear arch vortex and is subjected to reverse flow. This causes almost no correlation between Sensor H and Sensors J,K,L,N. A magnitude reading at 0 lags means that there is a similar reading at the same time. There were several weakly correlated values below 0.1 that are not reported. The largest cross correlation occurs between Sensor H and Sensor I (its closest neighboring sensor), which has a magnitude of over 0.5 and occurs at 57 lags or 5.7*ms*. From Figure 4.43 it shows that the velocity in this area is approximately $5.5 \frac{m}{sec}$ flowing back towards the rear face of the cube.

Table A.2 in Appendix A.4 shows all sensors cross-correlation with sensor I (76.2 *mm* behind the cube). There are numerous weakly correlated values between Sensor I and Sensors K,L and M and no correlation between Sensor I and Sensors N and O due to their distance. As expected, the largest cross correlations occurs between the two closest sensors, Sensor H and Sensor J. This pattern repeats through the remainder of the wake region where the two closest sensors have a cross-correlation value between .4 and .6 and the other sensors have little or no correlation. At the farthest region of the test section (3H or 228 *mm* from the rear face of the cube), the flow becomes more uniform as the flow structures dissipate. The cross-correlation magnitudes increases to over .6 between Sensors M,N,O and the time settles to 39 lags (3.9*ms*), which is near free stream velocity conditions. This shows that the reattachment point lies between 2.5H and 3H behind the cube.

Cube Cross-Correlation

The cross-correlation of the pressure data on the cube varies from the other sensors because of their off center locations in the test section. All of the previous sensors were positioned in a straight line down the center of the test section and embedded

Table 4.4: Cross-Correlation with Front Sensor

Sensor	Magnitude	Number of Lags	Sensor	Magnitude	Number of Lags
Top	0.1252	132	Rear	0.1589	443
	0.1095	3949		0.1603	595
	0.1252	4323		0.1238	723
	0.1025	4198		0.1060	864
	0.1159	4460	Left	0.1312	113
	0.1018	4593		0.1048	233
	0.1064	4994		0.1147	1219
	0.1106	9875		0.1065	9851
	0.1048	10005		0.1049	10238
Right	0.1500	110			
	0.1107	246			
	0.1024	4224			
	0.1245	5053			

into the floor section as seen in Figure 4.10. Each side of the cube has a single sensor positioned in the center to monitor the pressures for that particular region of interest as seen in Figure 4.10. The front sensor sits in the center of the front face of the cube to monitor the pressure in a stagnation region. The top sensor sits in a slow moving recirculation region that experiences reverse flow recirculation that is fed by flow moving up the rear face and both side faces of the cube. The rear sensor experiences continuous slow reverse flow as seen in Figures 4.41 and 4.43. Both the left and right side sensors also experience reverse flow due to the side vortices as seen in Figure 4.41.

Table 4.4 shows numerous cross-correlations between the front face sensor and the other cube sensors, but they are all weakly correlated with a value <0.2 . This is to be expected since the front face of the cube is a stagnation point with high pressure and zero velocity. This forces the flow to separate around the sides and the top of the cube.

Table 4.5 show the same weak cross-correlation values with the front sensor as seen in Table 4.4. Table 4.5 also shows some cross-correlation values between 0.2 and 0.3 for the right, left and rear sensors. The right and left sensors show similar

Table 4.5: Cross-Correlation with Top Sensor

Sensor	Magnitude	Number of Lags	Sensor	Magnitude	Number of Lags
Front	0.1048	-10005	Right	0.1509	-297
	0.1106	-9875		0.2199	-123
	0.1064	-4994		0.2108	-25
	0.1018	-4595		0.2556	97
	0.1159	-4460		0.1051	243
	0.1252	-4323		0.1051	9839
	0.1025	-4198	Left	0.2408	-58
	0.1095	-3949		0.2649	89
	0.1030	-237		0.1877	229
	0.1252	-132	Rear	0.1880	-161
				0.3001	13
				0.2324	138

cross-correlation values between 89 and 97 lags. This shows that both side sensors, inside the recirculating side vortices region show very similar readings at the same time and both are correlated to the reading taken in the top sensor which is also in a recirculating zone. The largest cross-correlation value is between the top and rear sensors at 0.3 with a near instantaneous lag of 1.3 *ms*. This shows that the flow, which is moving up the rear face of the cube produces a similar reading in the top and rear sensor at nearly the same time.

Table 4.6: Cross-Correlation with Rear Sensor

Sensor	Magnitude	Number of Lags	Sensor	Magnitude	Number of Lags
Front	0.1060	-864	Right	0.1637	-247
	0.1238	-723		0.1257	-110
	0.1603	-595		0.2948	15
	0.1589	-443		0.2169	141
Top	0.2324	-138		0.1257	260
	0.3000	13	Left	0.1340	-247
	0.1880	161		0.3097	-111
				0.3457	18
				0.2192	139
				0.1430	260

Table 4.6 show the same weak cross-correlation values with the front sensor as

Table 4.7: Cross-Correlation with Right Sensor

Sensor	Magnitude	Number of Lags	Sensor	Magnitude	Number of Lags
Front	0.1245	-5053	Left	0.1510	-264
	0.1224	-4224		0.2003	-134
	0.1107	-246		0.2227	1
	0.1496	-110		0.1730	128
	0.1115	21		0.1580	241
Top	0.1051	-9839	Rear	0.1189	351
	0.1999	-243		0.1257	-260
	0.2556	-97		0.2169	-141
	0.2108	25		0.2948	-15
	0.2199	123		0.3004	110
	0.1509	297		0.1637	244

seen in Table 4.4 and the same 0.3 cross-correlation at 13 lags as seen in 4.5. The right and left sensors both show similar cross-correlation magnitudes between 0.12 and 0.34 at nearly identical lags with the largest values occurring between 15 and 18 lags. As explained above, the right and left sensors are inside of a reverse flow region feeding the side recirculation vortex. This again shows that the pressures are approximately equal on both sides and that the side readings are related to pressure values seen in the rear reverse flow region between the cube and the rear arch vortex.

Table 4.7 shows the same cross correlation values for front, rear and top sensors with the right sensor as in previous tables. The largest correlation value between the right and left sensors occurs at time lag 1, nearly instantaneous which verifies the result discussed above with respect to the top sensor in that both side sensors, inside the recirculating side vortices region show very similar readings at the same time.

Due to the symmetry in the cross-correlations, all of the data in Table 4.8 is also found in Tables 4.4-4.7.

Table 4.5-Table 4.8 show that there is no strong measurable correlations between the pressure measurements on any face of the cube at the tested Reynolds number. They do however show that the left and right sensors experience similar magnitudes at similar time lags for all of the other sensors. The shape of the bluff body used and

Table 4.8: Cross-Correlation with Left Sensor

Sensor	Magnitude	Number of Lags	Sensor	Magnitude	Number of Lags
Front	0.1049	-10238	Right	0.1189	-351
	0.1065	-9851		0.1580	-241
	0.1147	-1219		0.1730	-128
	0.1048	-233		0.2227	-1
	0.1312	-113		0.2003	134
	0.1090	25		0.1510	264
Rear	0.1430	-260	Top	0.1877	-229
	0.2192	-139		0.2649	-89
	0.3457	-18		0.2408	58
	0.3097	111			
	0.1340	247			

the tested velocity produce sharp separations along the edges of the front face, which leave the left and right sensors in slow moving recirculation zones and the rear and top in slow moving reverse recirculation regions.

4.5 Summary

The University of North Carolina at Charlotte (UNCC) Motorsports Research Lab 0.3 m^3 Eiffel wind tunnel was upgraded to implement flow visualization through the use of a PIV system. The tunnel was also updated with a replaceable test section floor and flow settling chamber.

An initial set of experiments were conducted to determine the best seeding type and conditions to produce the most reliable and repeatable results. Three different flow seeding particles; i) smoke, ii) olive oil and iii) hydrogen filled soap bubbles were tested. It was determined that the olive oil seeding produced the highest average seeding density and maintained uniform seeding throughout the test section.

After numerous upgrades and improvements to the equipment and instrumentation, a series of experiments were conducted to gather flow data around a bluff body. Utilizing the 2D PIV system, eleven planes of data with 10 mm steps between each plane across the width of the cube were gathered. Pressure data for the center

plane was gathered simultaneously. The data was processed and vector maps were produced, which when averaged allowed for the recognition of flow structures in 2D as well as the magnitude of the velocities inside of the flow and structures. The 11 individual planes were then stitched together into a single volume and compared to the water channel results. The comparison shows the same basic flow structures in both media with minor differences around the locations of the vortex cores. The cores in the wind tunnel are farther away from the model due to more drastic flow separation regions around the edges.

The gathered pressure data was processed and filtered. An autocorrelation was conducted on the data to determine if there was a delayed copy of the sensor readings for each sensor. It was determined that each location had a moderate autocorrelation magnitude that occurred between 114 lags and 153 lags depending on where in the test area the sensor was located. The strongest autocorrelation occurred in the reverse flow region on the rear face of the cube.

Then a cross-correlation was conducted which showed that there are strong correlations in the wake region between any specific sensor and its closest two neighboring sensor. The cross-correlation magnitude increases the farther away from the model the readings are taken and the time lags decrease to a value that is near the time it takes the free stream velocity to move a single particle from one sensor to the next. This was used to determine the flow reattachment point to be between $2.5H$ and $3H$. Faint cross-correlations were detected between all of the sensors on the cube with the strongest being between the left and right sensor at near 0 lags. All of the other sensors also showed some faint correlations to the side sensors except the front sensor which showed nearly no correlation with any of the other sensors. The lack of cross-correlation between the sensors on the cube is due to a combination of the air velocity and model shape, which produced sharp separations along the edges of the front face and left the side sensors in slow moving recirculation zones.

4.5.1 Future Work

With the improvements to the wind tunnel, flow visualization became possible. The tunnel still requires additional improvements to smooth out the flow and improve overall flow quality in the test section. Increasing the number, location and resolution of sensors would improve the quality and reliability of the data. The addition of a pre-staging area for the seeding will improve seeding quality and density in the test area and increase the usable size of the test area. Utilizing other methods such as particle tracking would also make HFSB a viable option.

As with the water channel, to improve the system and track flow structures in time, a higher frequency system of 1,000 Hz or greater is required at the current velocity and Reynolds number as well as expanding the testing to other geometries and velocities. Additional supporting information can be gathered with the addition of a hot wire anemometer.

CHAPTER 5: UTILIZING PIV AND VIBRATED GRAIN PILES TO DETERMINE MOLECULAR HYDRODYNAMIC PROPERTIES

A new analog experimental technique was developed to study molecular hydrodynamic properties in dense gases and liquids.¹ This technique uses the macroscopic, single particle and collective particle dynamics of vibrated grain system to indirectly identify the hydrodynamics of the system at single as well as multi-molecule level. The single and collective particle motions are recorded using a high speed camera and PIV. The rigorous statistical mechanics that support this technique were first outlined by Keanini *et al*[96].

Unlike MD simulations and light and neutron scattering methods, this method utilizes a vibrated grain system which allows for a detailed study of molecular hydrodynamic processes within a non-equilibrium, flowing system [85].

This experimental setup and process was first designed and used to apply PIV to the vibrational finishing process by Fleischhauer *et al* [77]. The original data has also been compared to CFD in the vibratory finishing processes [76, 80] and used to study macroscopic liquid-state molecular hydrodynamics[86, 96].

The experimental process is used to gather reliable flow measurements to determine properties of the vibrated grain pile. This chapter outlines the experimental procedure that was developed to study molecular hydrodynamic properties in dense gases and liquids. The process involves several measurements of different types to include basic grain features, mass and size. Utilizing PIV to measure flow field ve-

¹This chapter is partially a collaborative work with Peter Tkacik, Brigid Mullany, Russel Keanini, Eric Fleishhauer, Hossein Shahinian, Farzad Azimi, Jayesh Navare, Spencer Owen, Jodie Sholar, Tony Martin and Tucker Bisel, UNC Charlotte, published in Dahlberg *et al* (2017) An Analog Macroscopic Technique for Studying Molecular Hydrodynamic Processes in Dense Gases and Liquids, J Vis Exp 130.

locities and force sensors to measure impact forces, it is possible to determine the material packing density, effective kinematic viscosity and dynamic viscosity.

It is noted that most models of single-grain motion account for the rotation of the grains which could affect the velocities. Since the grains utilized in these experiments are not spheroidal, but triangular, cylindrical or dumbbell shaped, accounting for the random rotations in and out of frame is not possible. It was assumed by Keanini *et al* that translational and rotational motions of individual grains were statistically independent and the velocities would surface with or without the presence of grain rotation[96] and that the flow could be considered Newtonian.

5.1 Vibrating Grain System

The vibrated gain system is composed of a Raytech AV-75 vibratory finishing system which consists of a 600 *mm* diameter annular polyurethane bowl attached to a single speed unbalanced motor as seen in Figure 5.1. The single-speed motor has an eccentric weight attached to the output shaft which generates the vibrations.

5.1.1 Media

Seven different types of Rösler vibratory polishing media were used to gather data. The results of these experiments were then compared to one another. The media seen in Figure 5.2 varied in shape, material and size, which is specified in Table 5.1.

Prior to conducting any experiments, the media was washed in water and allowed to air dry. The media packing density was determined using a method commonly known as the evacuation method [147]. This method starts by weighing the media ($\pm 5g$) and placing it inside a plastic sack, which was then lowered into a known volume bucket full of water. The sack full of media displaced an unknown volume of water from the bucket. The sack full of media was then carefully removed so as to not displace any additional water. The bucket was then refilled with water utilizing

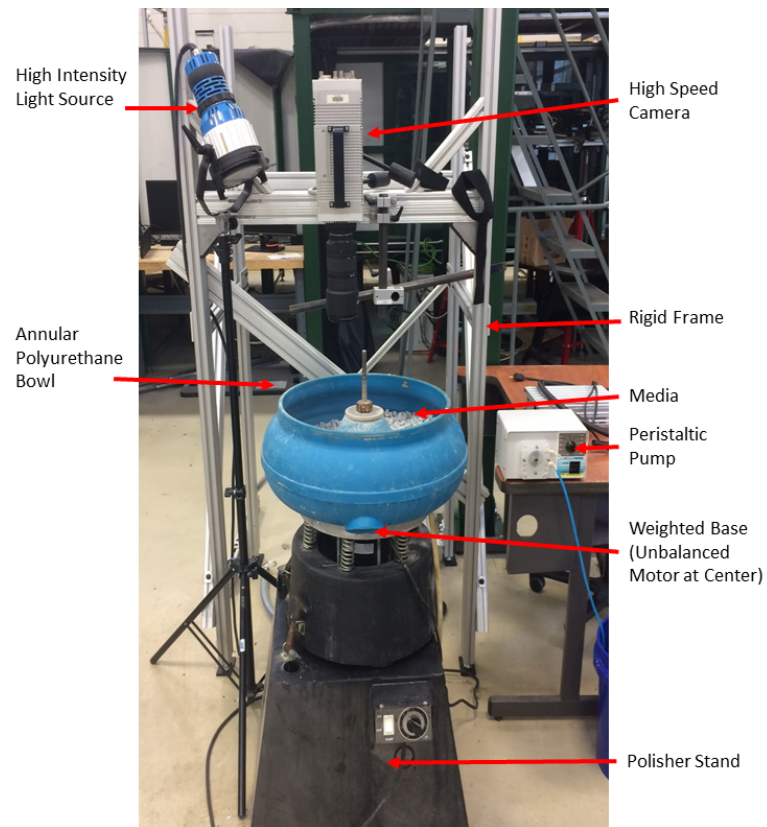


Figure 5.1: Vibratory system experimental set-up with camera and lighting modified from Dahlberg *et al*[85]



Figure 5.2: Seven media types used. A) RS 10/10, B) RS 19K, C) RS 10/22 ZS, D) RDP 09/09, E) 2mm Ball, F) RS 10/10S and G) 2050 40/13 DZ

Table 5.1: Media Dimensions and Characteristics

Rösler Media	Shape	Material	Dimensions (<i>mm</i>)	Surface Area (<i>m</i> ²)
RS 10/10	Triangle	Ceramic	10 x 10 x 10 x 10	0.00038
RS 19K	Conical	Ceramic	19 (d) x 17 (h)	0.00073
RS 10/22 ZS	Cylindrical	Ceramic	10(d) x 20(h)	0.00079
RCP 09/09	Triangle	Ceramic	9 x 9 x 9 x 9	0.00028
2mm Ball	Sphere	Ceramic	2 (d)	0.000013
RS 10/10S	Triangle 30°	Ceramic	10 x 10 x 10 x 10	0.00038
2050 40/13 DZ	Tristor Straight	Plastic	40 (base) x 13 x 36 (top)	0.00205

a 1000 *mL* graduated cylinder and the total amount of water added ($\pm 1\text{mL}$) was recorded. Each media type was measured three times and the results averaged. The packing density for each media type was then calculated using Equation 5.1. The averaged results of the measurements as well as the calculated packing densities are located in Table 5.2.

$$\rho_p = \frac{m}{V_p} \quad (5.1)$$

Where ρ_p is the packing density of the media in $\frac{\text{kg}}{\text{m}^3}$, m is the mass of the media in kg and V_p is the material packing volume determined by the displaced water in *mL*.

Table 5.2: Media Weight and Calculated Packing Densities

Rösler Media	Mass of Sample (<i>kg</i>)	Volume Water Displaced (<i>mL</i>)	Calculated Packing Density ($\frac{\text{kg}}{\text{m}^3}$)
RS 10/10	10.30 ± 0.005	6803.33 ± 92.91	1470.05 ± 19.93
RS 19K	12.00 ± 0.005	8200.00 ± 138.68	1464.29 ± 24.62
RS 10/22 ZS	10.40 ± 0.005	8000.00 ± 107.86	1299.62 ± 17.64
RCP 09/09	11.05 ± 0.005	5770.00 ± 20.00	1915.09 ± 5.42
2mm Ball	6.95 ± 0.005	5020.00 ± 155.88	1385.34 ± 42.26
RS 10/10S	10.30 ± 0.005	5790.00 ± 43.59	1416.29 ± 10.62
2050 40/13 DZ	7.70 ± 0.005	10920.00 ± 220.08	705.10 ± 14.22

The media density was also determined using the media geometry as seen in Table 5.3 and compared to the calculated media packing density results.

Figure 5.3 shows the difference between the packing density and the density cal-

Table 5.3: Media Weight and Calculated Densities by Geometry

Rösler Media	Mass (g)	Calculated Volume (mm^3)	Calculated Density ($\frac{kg}{m^3}$)
RS 10/10	$2.15 \pm .06$	709.35 ± 18.53	3027.80 ± 15.03
RS 19K	$8.90 \pm .02$	2189.25 ± 18.21	2577.08 ± 33.95
RS 10/22 ZS	$4.74 \pm .01$	2156.91 ± 22.18	2198.96 ± 23.40
RCP 09/09	$1.82 \pm .03$	459.20 ± 7.10	3964.69 ± 7.15
2mm Ball	$.01 \pm .00$	$4.15 \pm .36$	2633.71 ± 57.91
RS 10/10S	$2.17 \pm .02$	773.74 ± 7.78	2803.21 ± 29.50
2050 40/13 DZ	$7.49 \pm .04$	4904.02 ± 659.37	705.10 ± 14.22

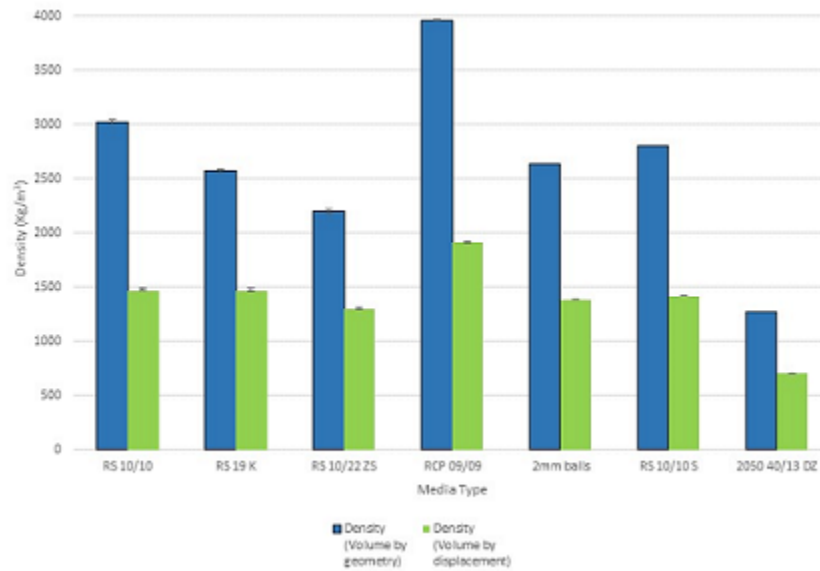


Figure 5.3: Density of media by geometry and displacement

culated using geometry. The packing density, which was calculated by water displacement was approximately 50% of the density calculated by geometry. Some of the differences are attributed to the complex geometries of the media, which cause a lower packing density due to regions between the media pieces that are occupied by air.

5.2 Particle Image Velocimetry

The PIV setup and system used for this experiment is non-traditional as it does not require a pulsing light source against a reflective seeding to produce light intensity

data acquired by an imaging system. It was determined that utilizing a high speed camera to record images of the highly lit area, that the Dantec Dynamic PIV software could detect sub grain scale, near uniform size, bright spots on the surface of the grains. The movement of these sub grain bright spots were then utilized in place of reflective seeding to produce the vector fields[76, 77, 85].

5.2.1 Camera

The camera utilized was a Redlake Motionextra HGXR high speed camera with 1504 x 1128 resolution and the capability to capture images up to 1,000 frames per second (fps). The camera was placed on a rigid frame as seen in Figure 5.1 with the camera lens perpendicular to the open surface of the grain piles. An 18-250 *mm* zoom lens with a 1:3.6-6.3 lens ratio was attached to the camera[85].

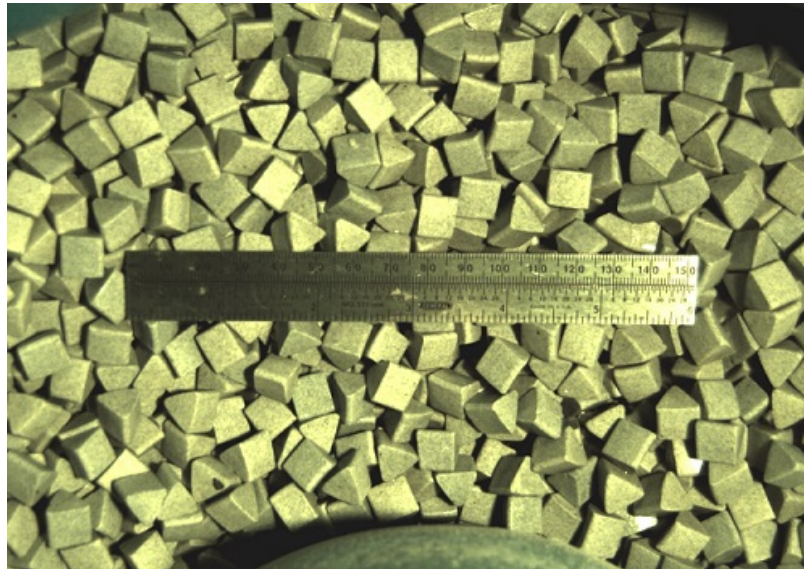


Figure 5.4: Camera field of view with ruler used for calibration

5.2.2 Calibration

To calibrate the PIV system, a single image was taken by the camera with a ruler placed in the FOV as seen in Figure 5.4. This image was imported into the PIV

system software and marked as "New Calibration". Inside the calibration window, the scale factor is measured in the display screen and the absolute distance entered from one point on the ruler to another known point[85] similar to the process outlined in Section 4.2.3 with the calibration target.

5.3 Sensors and Programs

A single triple-axis PCB Piezotronics accelerometer was utilized to gather bowl vibrations, both empty and with media present. The accelerometer has a non-linearity of $\leq 1\%$ with a range of 7,000 Hz on the x-axis and 10,000 Hz on the y and z-axis. The accelerometer was attached to the center of the bowl.

The sensor utilized to measure the force exerted by the grains as they passed through the test area was a single Uxcell 1 *kg* load cell. The load cell has a rated output of $1 \pm 0.15 \text{ mv/V}$ with a non-linearity of 0.05% full load and non-repeatability of 0.05% full load. A 25.4 *mm* diameter cylinder tube was attached to the load cell as seen in Figure 5.5 which was then suspended into the flow to measure the impact force. To remove edge effects, the cylinder was cut into three sections with the top and bottom sections securely attached to a stainless steel mounting rod, and the center section attached to the load cell to measure the force.

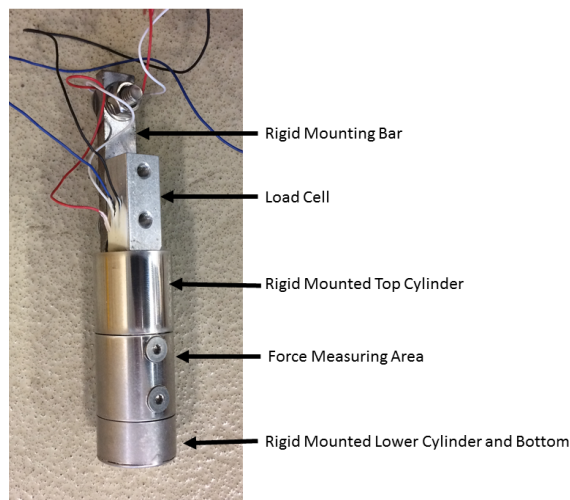


Figure 5.5: Load cell drag measurement apparatus

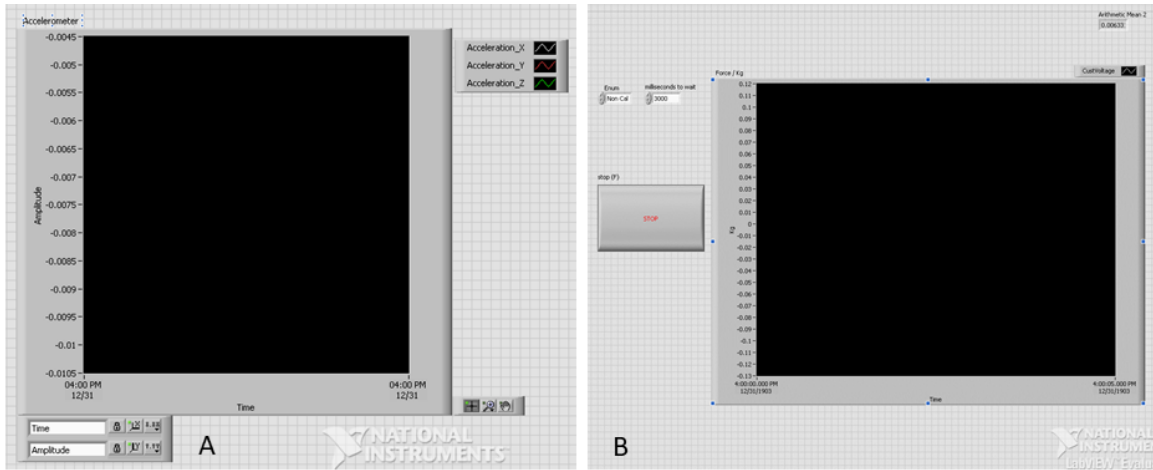


Figure 5.6: Front screen of vibrated grain piles A) accelerometer LabVIEW[®] program and B) force LabVIEW[®] program.

Both the accelerometer and the load cell were then wired into a National Instruments[®] SCXI-1000. The data acquisition programs were written in LabVIEW[®] with an acquisition frequency of 1,000 Hz. Figure 5.6A shows the front screen of the accelerometer program and Figure 5.6B shows the front screen of the force program. A detailed view of the LabVIEW[®] block diagrams can be found in Appendix B.1 and B.2 respectively.

5.4 Experimental Setup and Processing

A rigid frame as seen in Figure 5.1 was set up, separate from the vibrational system to insure that the vibrations from the system did not effect imaging or data acquisition. The camera was attached to the rigid frame with the lens opening approximately 550 *mm* above the surface of the vibrating media. This distance was determined to reduce edge effects while still allowing enough light to enter to produce usable images. At 550 *mm* with i) the specified lens, ii) the distance from the lens to the media surface and iii) the maximum spread angle of the field of view, it was determined that the distance differences between the lens and the media surface from the center to the edge of the FOV was $\leq 2\%$.

An ARRI EB-400 high intensity halogen light was used to illuminate the test area. The f-stop on the lens was determined by visually inspecting the computer screen and changed to achieve maximum brightness. For this experiment the f-stop was determined to be 3.6. The focal length of 180mm was determined to be the proper setting to achieve the desired FOV ($210\text{ mm} \times 160\text{ mm}$). In the camera software, the camera acquisition rate was set to 500 frames/sec in order to resolve the grain-collision-time-scale dynamics, which requires the frame rate to be at least an order of magnitude larger than the imposed vibration frequency of the system, which was determined to be 29.3 Hz [76, 77, 85] from previous results and verified in Section 5.5.1.

5.4.1 Data Acquisition

Once the experimental apparatus was setup, the vibrating bowl was operated without any media present to determine the vibration frequency of the system. Once this was complete, the chosen media was added to the bowl and the vibrational frequency of the system was determined a second time. To ensure smooth movement of the media and minimize friction between individual pieces, 150 *mL* of a 3% finishing compound was added to the bowl. To maintain lubrication throughout the experiment, a Mity Flex peristaltic pump was set to provide 1.9 *L/h* of the finishing compound to the bowl.

With camera software activated and lighting conditions verified, the camera was focused. The experimental run time was determined by trial and error to ensure that it was long enough that statistically stationary grain flow conditions set in, but not so long as to produce excessive amounts of redundant data. With an acquisition frequency of 500 Hz, the experimental run time was determined to be 10.1 seconds, thus acquiring 5060 image frames. It was determined that steady state conditions in the flow were met at approximately 1 second.

The vibratory system was activated along with the peristaltic pump providing the 3% finishing solution. The system was allowed to operate for one minute to ensure an equal amount of solution was exiting the bowl drain as was being added by the pump. The camera was triggered to initialize image capture in the camera software for 10.1 seconds based on the pre-determined experimental run time. This was repeated three times without the force sensor in place.

The load cell probe was then suspended on an arm attached to the rigid support frame into the media. The sensor was calibrated in position with the media restrained to avoid contact. Once the calibration was complete, the media was allowed to fill the void and contact the sensor. The vibratory system was activated along with the peristaltic pump as explained in the previous paragraph. The camera was triggered to initialize image capture in the camera software at the same time as the force data acquisition was initiated in the LabVIEW[®] program. Both the camera image acquisition and the force data acquisition were conducted for 10.1 seconds. This process was also repeated three times.

The calibration and data acquisition was repeated for each of the seven types of media listed in Table 5.1.

5.4.2 Data Processing

To conduct the PIV data processing, all of the images were downloaded from the high speed camera and transferred to the PIV computer. In order for the PIV system to accurately calculate the vector fields, each image was converted from a color image to a gray scale image using a MATLAB[®] program seen in Appendix B.3.

Once all of the images were imported into Dantec Dynamics, the calibration image was separated and calibration conducted as outlined in the calibration section of this chapter. This process gathered images in single frame-mode, instead of image pairs (double-frame mode) as outlined in previous chapters. To process the data, image

pairs were created inside the import software options by pairing each image with the next image in sequence (1-2, 2-3, 3-4, ...) utilizing the "Make Double Frame" option[85].

The particle density, which for the media is sub grain scale bright spots on the surface of the grains that the software recognizes was then checked. The probe size area was changed until a minimum of three particles were consistently viewed in the probe area. This probe area was then used as the interrogation area during processing[85]. The images were divided into an $n \times n$ grid of pixels using the adaptive correlation method and a defined area of pixels. This sets the individual interrogation areas. As the PIV program processes the image, it compares the pattern of sub-grain-scale bright spots within each established interrogation area against corresponding patterns captured in the next image in the image pair. From this comparison, the PIV software determines an area-averaged displacement vector and dividing by the time increment between frames, determines the area-averaged velocity[85].

The vibration data for both empty and full bowl was processed utilizing MATLAB[®] built in functions. The force data was processed utilizing Excel[®] and Minitab[®] statistical software.

5.5 Results

5.5.1 Vibrational Spectra

For the series of experiments, the vibrational frequency of the empty bowl system was determined to be 29.3 Hz in the X-direction as seen in Figure 5.7, which confirms previous tests [76, 77, 85]. The spectra in the Y- and Z- direction match the X-direction frequencies, only with different magnitudes.

With the empty bowl frequency verified, the media was added to the bowl and the test repeated for each media type. The data was processed and frequencies

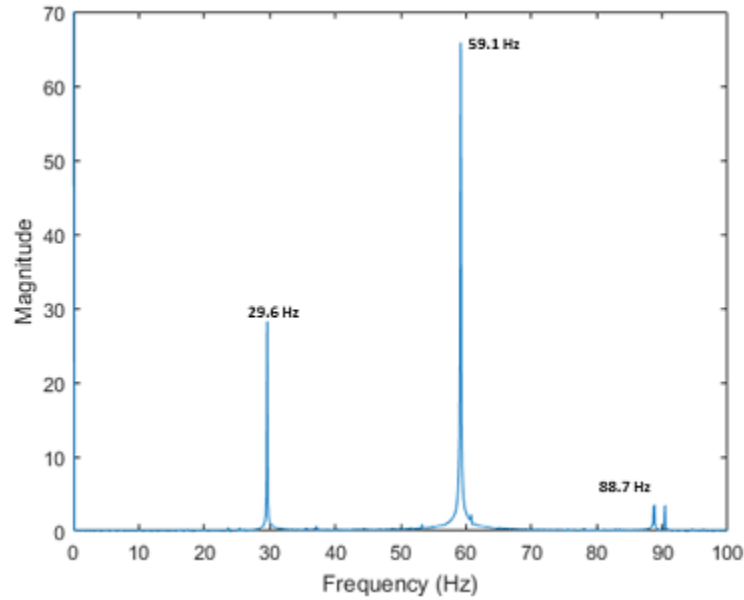


Figure 5.7: Bowl vibrational spectra without media present

determined.

Figure 5.8 shows the vibrational spectra with RS 10/10 media present (blue) overlaid on the graph of the vibrational spectra without media (orange). Figures 5.7 and 5.8 show that the dominate frequency, which details the motor speed is at 29.3 Hz and its harmonics at 58.6 Hz and 87.9 Hz. With the media in the bowl, the combination takes on the characteristics of a solid, which produce additional peaks at 44 Hz and 73.3 Hz. As with Figure 5.7, the spectra in the Y- and Z- direction with media present match the X-direction frequencies, only with different magnitudes. Once normalized, these results match those previously reported [76, 77, 85, 96].

Figure 5.9 shows the normalized vibrational spectra with media present (blue) overlaid on the without media graph (orange) for the other six types of media. The frequencies remain the same through all of the media types, only the magnitudes vary. As previously stated, the spectra in the Y- and Z- direction with media present match the X-direction frequencies.

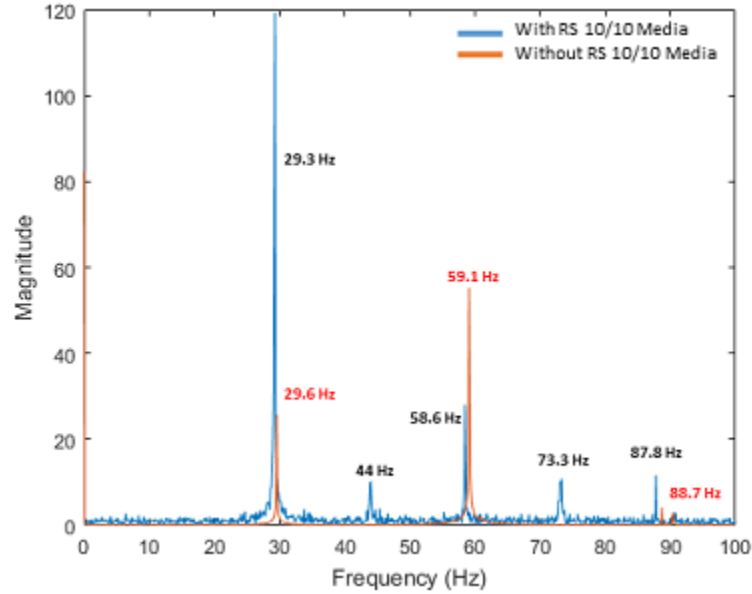


Figure 5.8: Bowl vibrational spectra with RS 10/10 media (blue) and without out (red) media present

5.5.2 Force Measurements

For the series of experiments the force of the media impact on the sensor varied by media type. Table 5.4 shows the average impact measurement in kilograms and converted force in Newtons for each media type, which averaged between $0.25N$ and $0.80N$.

Table 5.4: Average Impact Measurement and Force

Rösler Media	Average Impact Measurement (kg)	Average Impact Force (N)
RS 10/10	0.0470 ± 0.0129	0.4613 ± 0.1270
RS 19K	0.0466 ± 0.0205	0.4573 ± 0.2010
RS 10/22 ZS	0.0508 ± 0.0211	0.4986 ± 0.2068
RCP 09/09	0.0379 ± 0.0116	0.3715 ± 0.1133
2mm Ball	0.0260 ± 0.0018	0.2550 ± 0.0177
RS 10/10S	0.0823 ± 0.0282	0.8070 ± 0.2768
2050 40/13 DZ	0.0586 ± 0.0164	0.5744 ± 0.1604

As seen in Table 5.4, the smallest average force with the smallest deviation was experienced in the presence of the $2mm$ ball media, which is tightly packed and

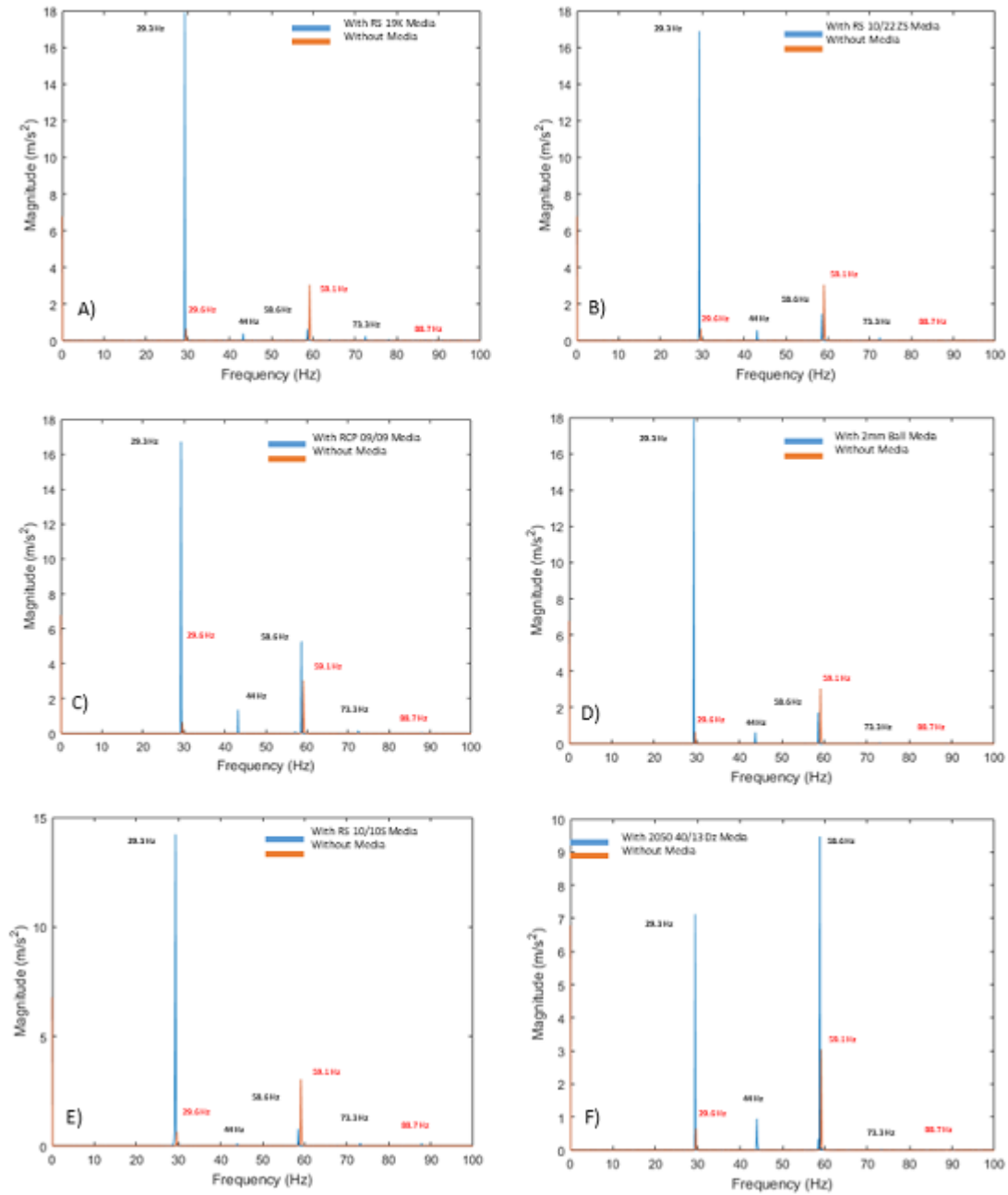


Figure 5.9: Normalized bowl vibrational spectra without media overlaid on vibrational spectra with media present for A) RS 19K B) RS 10/22 ZX C) RCP 09/09 D) 2mm Ball E) RS 10/10S and F) 2050 40/13 DZ

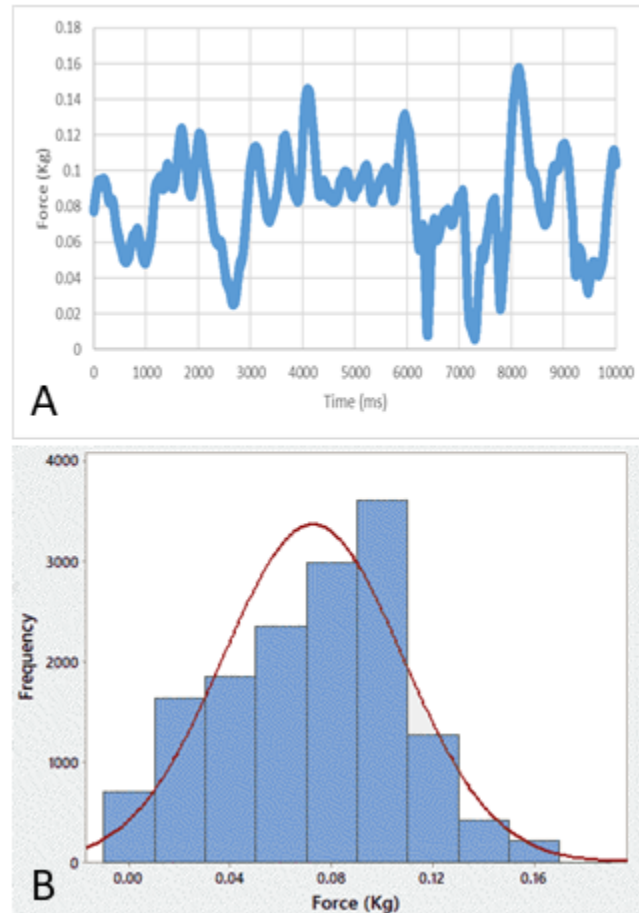


Figure 5.10: A) Raw force data and B) histogram of the force data from one 10/10S test

symmetric. The largest force was experienced in the presence of the RS 10/10S which has 30° angled sides. This media type tumbled off of its corners at varying angles causing the higher forces and larger deviations. The 2050 40/13 DZ, which has the most complex shape, largest volume and lowest density had impact forces that fell slightly above the other triangular and cylindrical media types, but below the RS 10/10S.

Figure 5.10A shows the raw data for a single 10 second impact force test. The figure also demonstrates the range of impact forces from near 0 *kg* up to 0.168 *kg* over the time period. This large variation of forces was due to complex geometry of the media and its perpetual tumbling at a variety of angles during impact with the

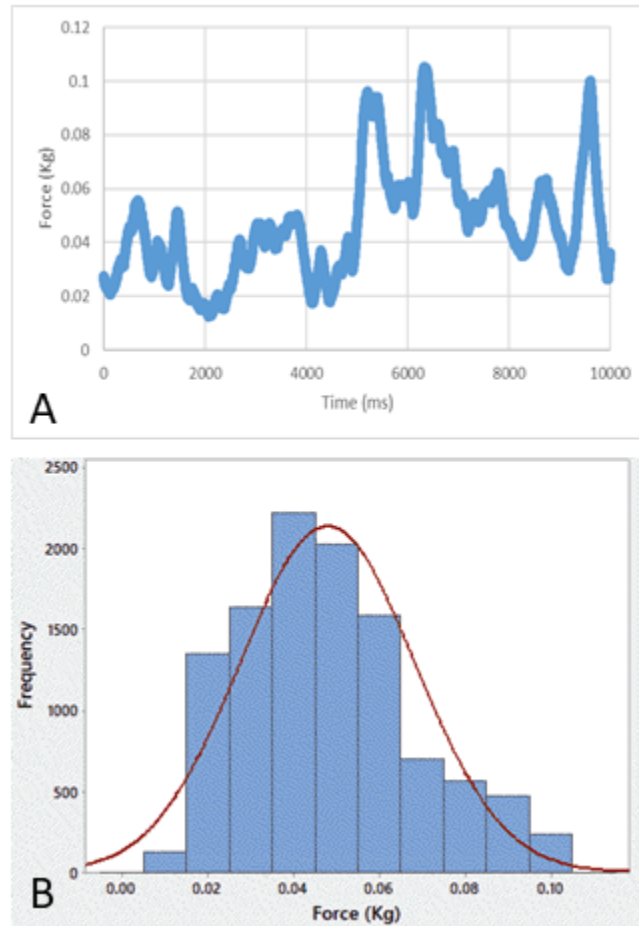


Figure 5.11: A) Raw force data and B) histogram of the force data from one RS 19K test

load sensor.

Figure 5.10B shows a histogram of the impact force results with a normal distribution curve overlaid. From Figure 5.10B it can be seen that the data presents a negative skew where the mean value of the data is to the left of the mode, or most often occurring value. The RS 10/10S media is the only media type tested that presents a negative skew.

Figure 5.11A shows the raw data for a single 10 second impact force test with the RS 19K media. The range of impact forces for the RS 19K media was between 0.013 *kg* up to 0.105 *kg*. Figure 5.11B shows a histogram of the impact force results with the normal distribution curve. From Figure 5.11B it can be seen that the data

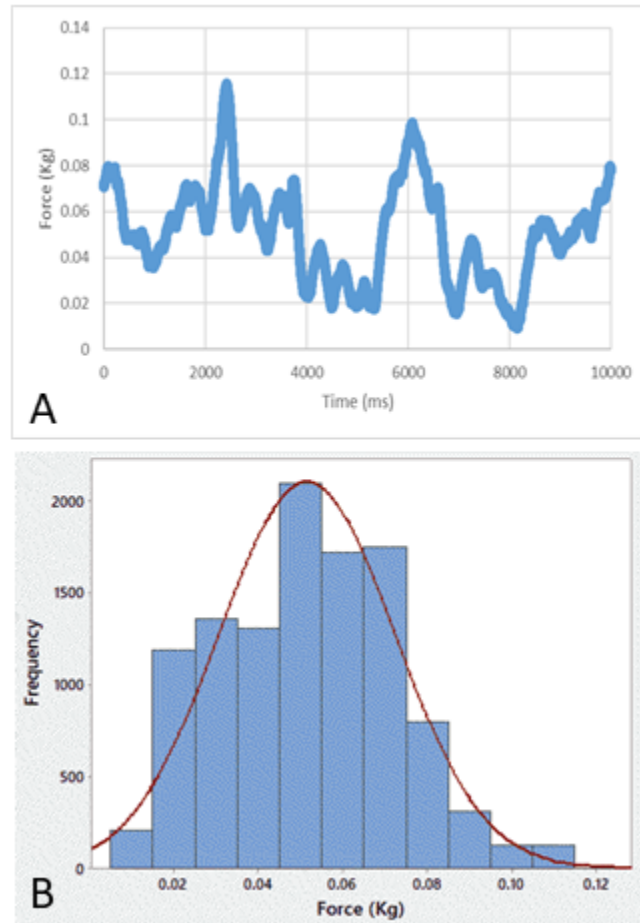


Figure 5.12: A) Raw force data and B) histogram of the force data from one RS 10/22 ZS test

presents a positive skew where the mean value of the data is to the right of the mode.

Figure 5.12A shows the raw data for the RS 10/22 ZS media test. The range of impact forces for the RS 10/22 ZS media was between 0.010 *kg* up to 0.115 *kg*. Figure 5.12B shows a histogram of the impact force results with the normal distribution curve. From Figure 5.12B it can be seen that this data also presents a positive skew.

Figure 5.13A shows the raw data for a single test with the RCP 09/09 media. The range of impact forces for the RCP 09/09 media was between 0.015 *kg* up to 0.074 *kg*. Figure 5.13B shows a histogram of the impact force results with the normal distribution curve and positive skew.

Figure 5.14A shows the raw data for a single test with the 2mm ball media. The

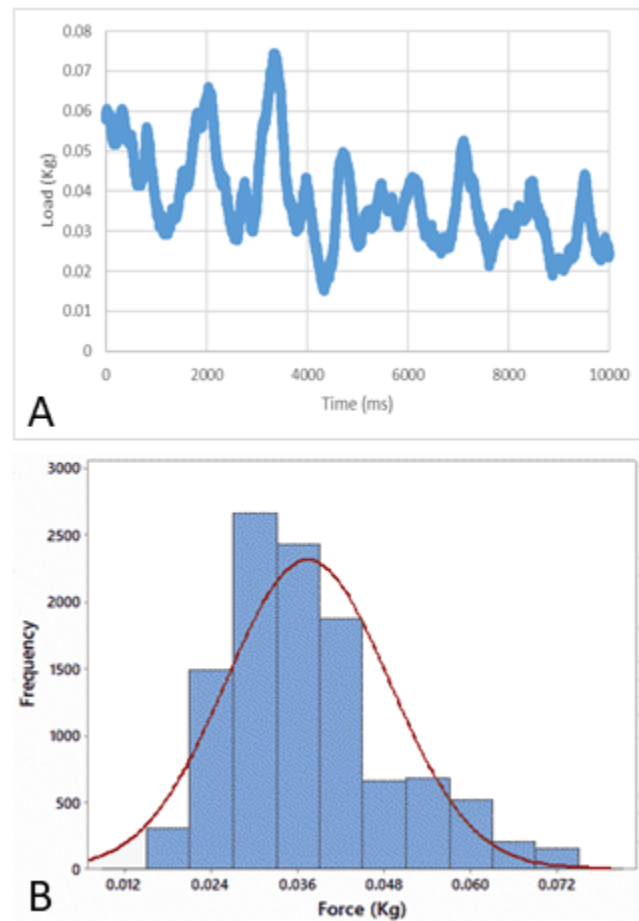


Figure 5.13: A) Raw force data and B) histogram of the force data from one RCP 09/09 test

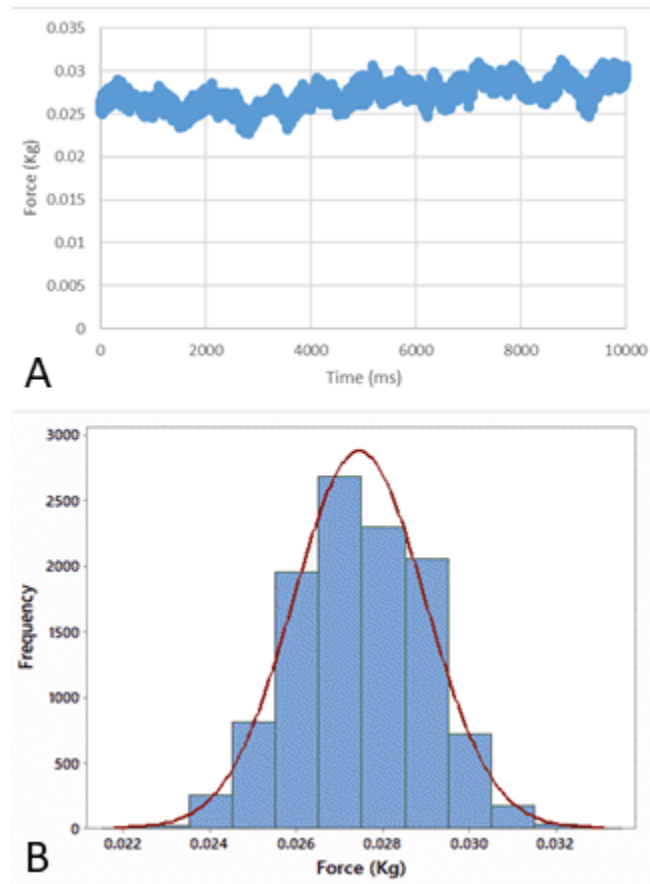


Figure 5.14: A) Raw force data and B) histogram of the force data from one 2mm ball test

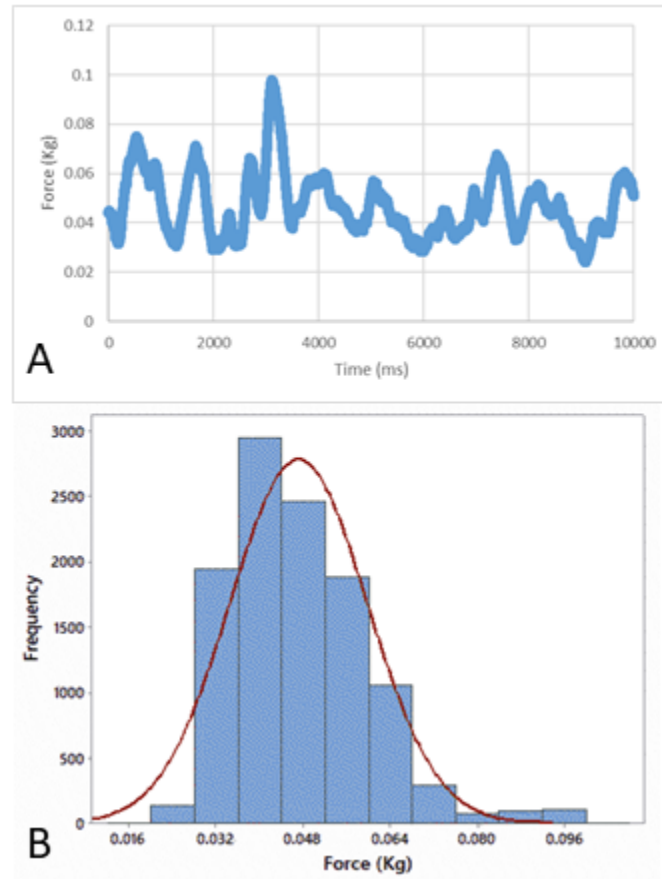


Figure 5.15: A) Raw force data and B) histogram of the force data from one RS 10/10 test

range of impact forces for the $2mm$ ball media was between 0.023 kg up to 0.032 kg . This is the smallest range of impact forces of all of the media types as highlighted earlier. Figure 5.14B shows a histogram of the impact force results with the normal distribution curve. From Figure 5.14B it can be seen that the data presents a slightly positive skew. The $2mm$ ball media also displayed the lowest skewness value of .015.

Figure 5.15A shows the raw data for a single test with the RS 10/10 media. The range of impact forces for the RS 10/10 media was between 0.024 kg up to 0.098 kg . Figure 5.15B shows a histogram of the impact force results with the normal distribution curve with a positive skew. The RS 10/10 media displayed the highest total skewness value of 0.995.

Figure 5.16A shows the raw data for a single test with the 2050 40/13 DZ media.

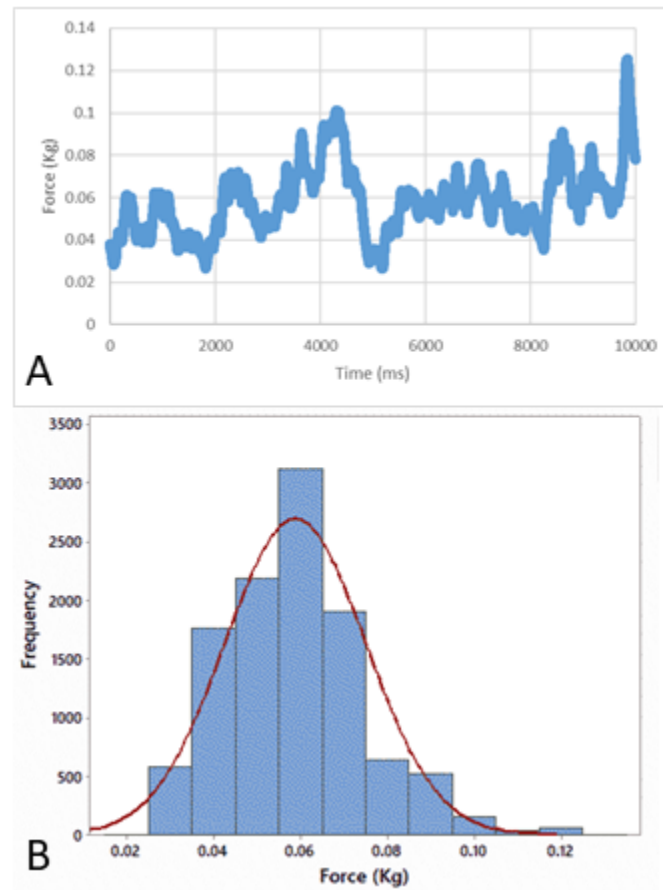


Figure 5.16: A) Raw force data and B) histogram of the force data from one 2050 40/13 DZ test

The range of impact forces for the 2050 40/13 DZ media was between 0.026 *kg* up to 0.126 *kg*. This media type presents the largest minimum impact force of all of the tests. Figure 5.16B shows a histogram of the impact force results with the normal distribution curve with a slightly positive skew.

5.5.3 Velocity Measurements

To determine the velocity at the point of impact on the sensor, two separate tests were conducted per media type (with and without force sensor) as outlined in Section 5.4.1. Figure 5.17A shows the test without the force sensor in place. After the images were gathered and downloaded, the sensor was placed into the non-vibrating flow and calibrated. After the calibration was complete, the bowl was activated and flow monitored to ensure uniform distribution of the media around the sensor. Once the flow was uniform, a second set of images were gathered as seen in Figure 5.17B. The data was then processed as outlined in Section 5.4.2 and vector fields were created. Each of the individual vector maps contained 6417 vectors. The vector map without the force sensor present (Figure 5.17C) had 10 vectors rejected and 47 vectors substituted. The vector map with the force sensor present (Figure 5.17D) had 76 vectors rejected and 65 vectors substituted.

Figure 5.17C shows the processed vector field without the load cell present and Figure 5.17D shows the processed vector field with the load cell present. The statistics of the two runs were compared and determined to be in good agreement with the exception of the differences in the immediate vicinity of the force sensing device.

Table 5.5 shows the measured point velocities for all seven media types.

The highest velocities were recorded for the RS19K and RS 10/22 ZS, both of which presented a large amount of roll due to their geometries and smooth sides. All of the media types with sharp edges or geometries displayed similar velocities, except the RS 10/10S, which has 30° angled sides. These angled sides caused slightly higher

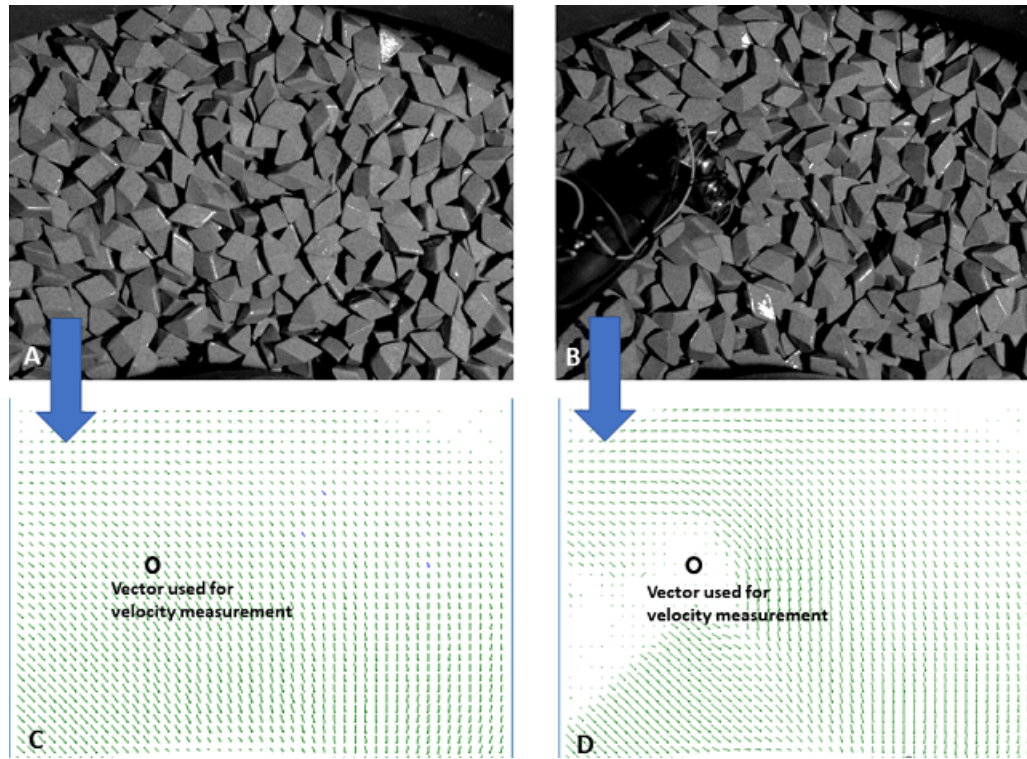


Figure 5.17: RS 10/10S grain pile A) without force sensor B) with force sensor C) vector map without force sensor D) vector map with force sensor

Table 5.5: Point Velocities	
Media	Velocity ($\frac{m}{sec}$)
RS 10/10	0.0566
RS 19K	0.0759
RS 10/22 ZS	0.0791
RCP 09/09	0.0566
2mm Ball	0.0388
RS 10/10S	0.0673
2050 40/13 DZ	0.0551

velocities than the similar media with non-angled sides. The 2mm ball showed the lowest velocities due to their symmetry and close packing.

5.5.4 Media Coefficient of Drag

Given the measured average forces, velocity of media and force sensing area, the coefficient of drag was calculated using Equation 5.2.

$$C_d = \frac{F_d}{\frac{1}{2}\rho_p v_m^2 A} \quad (5.2)$$

Where C_d is the coefficient of drag (dimensionless), F_d is the measured drag force in N, ρ_p is the packing density of the media in $\frac{kg}{m^3}$, v_m is the velocity of the media in $\frac{m}{sec}$ and A is the orthogonal projection area of the cylinder on the plane normal to fluid flow in m^2 .

Table 5.6 shows the calculated coefficient of drag values for all seven media types.

Table 5.6: Coefficient of Drag	
Media	Coefficient of Drag
RS 10/10	218.24
RS 19K	170.88
RS 10/22 ZS	193.00
RCP 09/09	140.71
2mm Ball	385.06
RS 10/10S	252.60
2050 40/13 DZ	845.33

5.5.5 Determining Reynolds Number

The vibrated grain piles utilized in this study can be described as having very low Reynolds numbers (<0.02) which are also known as Stokes flow or creeping flow ($Re \ll 1$). This type of flow was studied by Stokes, using a circular cylinder in a cross flow. Several future researchers continued this line of research into the early and

mid twentieth century [148–151]. Each of these researchers made minor modifications to the original work to improve their results. Through these methods, drag force can be determined for low Reynolds numbers or Reynolds numbers determined based on drag force. Although the methods of Oseen [148], Kaplum [150], Chaplin [149] and Tomotika and Aois [151] used different methods, they are very similar in the low Reynolds number region.

To determine the Reynolds number of each media type, a table was created as seen in Appendix B.4 which utilized three different classical Reynolds number dependent coefficient of drag equations. The equations were utilized to determine the Reynolds number of the flow based on the the drag coefficient which was calculated from the experimental data. The first method utilized the 1st Term of the Lamb-Oseen Equation (Equation 5.3), the second method utilized the first two terms of the same equation (Equation 5.3) and the final method utilized the Chaplin Equation (Equation 5.4).

$$C_d = \frac{4\pi}{Re} [\Delta_1 - 0.87\Delta_1^3 + O\Delta_1^4] \text{ where } \Delta_1 = \frac{1}{\text{Log}(\frac{4}{Re}) - \gamma - \frac{1}{2}} \quad (5.3)$$

Where γ is Euler's constant = 0.577216... [152].

$$C_d = 7.638Re^{-0.849} \exp \left[0.04 \text{Log}^3 \left(\frac{Re}{0.01} \right) 0.000611 \log^5 \left(\frac{Re}{0.01} \right) \right] \quad (5.4)$$

The coefficient of drag was first calculated as shown in Section 5.5.4 with the measured PIV data, drag force data and the calculated packing density. The coefficient of drag was then located on the table and the corresponding Reynolds number was determined.

Table 5.7 shows corresponding Reynolds number for each media type and method based on the calculated coefficient of drag.

The results of Table 5.7 show that the 1st term Oseen equation and the Chaplin equation are nearly identical in every situation with the two term Oseen equation

Table 5.7: Reynolds Number Comparison

Media	1st Term Oseen	2 term Oseen	Chaplin Equation
RS 10/10	0.0097	0.0094	0.0097
RS 19K	0.0130	0.0126	0.0129
RS 10/22 ZS	0.0112	0.0109	0.0112
RCP 09/09	0.0165	0.0159	0.0163
2mm Ball	0.0049	0.0048	0.0049
RS 10/10S	0.0081	0.0079	0.0081
2050 40/13 DZ	0.0020	0.0020	0.0020

producing results which are slightly less. Since the Reynolds number stays $\ll 1$ for all three equations, the flow is considered creeping.

5.5.6 Kinematic and Dynamic Viscosity Realization for Vibrated Grain Piles

Viscosity is a fluid's resistance to flow. There are two types of viscosity, dynamic and kinematic. Dynamic viscosity is also referred to as shear or absolute viscosity. The major difference between the two viscosities in their simplest terms is that kinematic viscosity does not take into consideration the fluid density, where dynamic viscosity does. Equation 5.5 is the typical equation for dynamic viscosity and Equation 5.6 is the standard equation used to get the kinematic viscosity from the dynamic viscosity.

$$\mu = \frac{\tau}{\frac{du}{dy}} \quad (5.5)$$

Where μ is the dynamic viscosity in $\frac{kg}{m \cdot sec}$, τ is the shear stress $\frac{N}{m^2}$, du is unit velocity of the media in $\frac{m}{sec}$ and dy is the distance between shear layers in m .

$$\nu = \frac{\mu}{\rho_p} \quad (5.6)$$

Where ν is the kinematic viscosity in $\frac{m^2}{sec}$ and ρ_p is the packing density of the media in $\frac{kg}{m^3}$.

Due to the difficulty in measuring quantities for the variables in Equation 5.5, the relationship between kinematic and dynamic viscosities and the Reynolds number (Equation 2.1) were used to rewrite Equations 5.5 and 5.6 to utilize available data to determine kinematic and dynamic viscosities.

Equation 2.1 was re-expressed in terms of dynamic viscosity as shown in Equation 5.7.

$$\mu = \frac{\rho_p v_m L}{Re} \quad (5.7)$$

Where ρ_p is the packing density of the media in $\frac{kg}{m^3}$, v_m is media velocity in $\frac{m}{sec}$, L is the characteristic length or diameter of the cylinder in m and Re is the Reynolds number (dimensionless).

Equation 5.7 was then placed into Equation 5.6 resulting in become 5.8.

$$\nu = \frac{v_m * L}{Re} \quad (5.8)$$

All of the variables in Equation 5.8 are experimentally recorded data or the Reynolds number which was determined in Section 5.5.5. The kinematic viscosity (ν) was then substituted into Equation 5.9 to determine the dynamic viscosity.

$$\mu = \nu * \rho_p \quad (5.9)$$

Table 5.8 shows the results of the calculated kinematic viscosities utilizing Equation 5.8 and dynamic viscosities utilizing Equation 5.9. All of the calculations utilized the Reynolds number obtained using the Chaplin Equation results from Table 5.7 .

Table 5.9 shows a brief list of dynamic viscosities for common liquids and solids [153, 154]. Based on this list, the viscosity of the media is comparable to peanut butter at 20°C but less than lard at the same temperature.

Table 5.8: Kinematic and Dynamic Viscosity

Media	Kinematic Viscosity ($\frac{m^2}{sec}$)	Dynamic Viscosity ($\frac{kg}{m*sec}$)
RS 10/10	0.1764	259.78
RS 19K	0.1493	218.61
RS 10/22 ZS	0.1799	233.72
RCP 09/09	0.1028	196.92
2mm Ball	0.1992	275.76
RS 10/10S	0.3012	326.03
2050 40/13 DZ	0.7096	500.21

Table 5.9: Common Material Dynamic Viscosity

Material	Dynamic Viscosity ($\frac{kg}{m*sec}$)
Water at 20°C	.001 [153]
Caster Oil at 20°C	1 [153]
Honey at 20°C	10 [153, 154]
Chocolate at 20°C	25 [153]
Ketchup at 20°C	50 [153, 154]
Sour Cream at 20°C	100 [153]
Peanut Butter at 20°C	150-250 [153]
Lard at 20°C	1000 [154]
Vegetable Shortening at 20°C	1200 [154]
Glass at 724°C	$10^{6.6}$ [154]

5.6 Summary

It is believed that this process, when developed was the first to use vibrated grain piles to study liquid-state molecular hydrodynamic processes [85]. This technique uses the macroscopic, single particle and collective particle dynamics of vibrated grain system to indirectly identify the hydrodynamics of the system at single as well as multi-molecule level.

Basic material characteristics and properties were gathered for each media type. The media packing density was determined using the evacuation method[147]. PIV and impact force data were gathered and processed. The effective kinematic and dynamic viscosities were then calculated for each media type. This direct data can be

utilized to improve current computational models used to determine material removal rate in vibratory polishing [77]. The results of this series of experiments demonstrate that microscopic molecular hydrodynamic processes can be observed and studied using vibrated grain piles.

Despite the positive results, the technique does have limitations. In the presented configuration, vertical grain velocities can not be captured due to the opaque bowl and media. Based on observations and theory, it is believed that on average, the flow remains uniform and that the vertical component of the velocity is on the same order as the measured components [96]. These observations lead to the assumption that the statistical properties are also the same in the vertical component[96] and thus the limitation has very little impact on the stated results.

5.6.1 Future Work

As this work progresses it will be possible with some modifications to equipment and procedures to determine and verify theoretical values for hydrodynamic modes. Improvements to the sensor capabilities and increasing the size of the vibratory bowl will produce more accurate and uniform readings for analysis.

REFERENCES

- [1] E. Fleischhauer, J. L. Dahlberg, P. T. Tkacik, and S. Hellman, "Tomographic piv measurement in a bluff body wake utilizing an asymmetric camera configuration and least squares matching," in *55th AIAA Aerospace Sciences Meeting*, p. 1644, 2017.
- [2] E. Hansche, George and J. S. Rinehart, "Air drag on cubes at mach numbers 0.5 to 3.5," *Journal of Aeronautical Sciences*, vol. 19, no. 2, pp. 83–846, 1952.
- [3] S. Munshi, V. Modi, and T. Yokomizo, "Aerodynamics and dynamics of rectangular prisms with momentum injection," *Journal of Fluids and Structures*, vol. 11, no. 8, pp. 873–892, 1997.
- [4] A. Roshko, "On the wake and drag of bluff bodies," *Journal of the aeronautical sciences*, vol. 22, no. 2, pp. 124–132, 1955.
- [5] R. J. Martinuzzi and B. Havel, "Vortex shedding from two surface-mounted cubes in tandem," *International journal of heat and fluid flow*, vol. 25, no. 3, pp. 364–372, 2004.
- [6] I. Castro and A. Robins, "The flow around a surface-mounted cube in uniform and turbulent streams," *Journal of fluid Mechanics*, vol. 79, no. 02, pp. 307–335, 1977.
- [7] A. Robins and I. Castro, "A wind tunnel investigation of plume dispersion in the vicinity of a surface mounted cube i. the flow field," *Atmospheric Environment (1967)*, vol. 11, no. 4, pp. 291–297, 1977.
- [8] A. Robins and I. Castro, "A wind tunnel investigation of plume dispersion in the vicinity of a surface mounted cubeii. the concentration field," *Atmospheric Environment (1967)*, vol. 11, no. 4, pp. 299–311, 1977.
- [9] R. Martinuzzi, C. Tropea, *et al.*, "The flow around surface-mounted, prismatic obstacles placed in a fully developed channel flow," *TRANSACTIONS-AMERICAN SOCIETY OF MECHANICAL ENGINEERS JOURNAL OF FLUIDS ENGINEERING*, vol. 115, pp. 85–85, 1993.
- [10] R. J. Martinuzzi and B. Havel, "Turbulent flow around two interfering surface-mounted cubic obstacles in tandem arrangement," *Journal of fluids engineering*, vol. 122, no. 1, pp. 24–31, 2000.
- [11] M. Gohlke, J.-F. Beaudoin, M. Amielh, and F. Anselmet, "Experimental analysis of flow structures and forces on a 3d-bluff-body in constant cross-wind," *Experiments in Fluids*, vol. 43, no. 4, pp. 579–594, 2007.
- [12] A. Larousse, R. Martinuzzi, and C. Tropea, "Flow around surface-mounted, three-dimensional obstacles," in *Turbulent Shear Flows 8*, pp. 127–139, Springer, 1993.

- [13] H. J. Hussein and R. Martinuzzi, "Energy balance for turbulent flow around a surface mounted cube placed in a channel," *Physics of Fluids*, vol. 8, no. 3, pp. 764–780, 1996.
- [14] R. E. Eskridge and R. S. Thompson, "Experimental and theoretical study of the wake of a block-shaped vehicle in a shear-free boundary flow," *Atmospheric Environment (1967)*, vol. 16, no. 12, pp. 2821–2836, 1982.
- [15] R. E. Eskridge and S. T. Rao, "Turbulent diffusion behind vehicles: experimentally determined turbulence mixing parameters," *Atmospheric Environment (1967)*, vol. 20, no. 5, pp. 851–860, 1986.
- [16] E. Adams and J. Johnston, "Flow structure in the near-wall zone of a turbulent separated flow," *AIAA journal*, vol. 26, no. 8, pp. 932–939, 1988.
- [17] E. Adams and J. Johnston, "Effects of the separating shear layer on the reattachment flow structure part 1: Pressure and turbulence quantities," *Experiments in Fluids*, vol. 6, no. 6, pp. 400–408, 1988.
- [18] E. Adams and J. Johnston, "Effects of the separating shear layer on the reattachment flow structure part 2: Reattachment length and wall shear stress," *Experiments in Fluids*, vol. 6, no. 7, pp. 493–499, 1988.
- [19] P. Bearman, "Near wake flows behind two-and three-dimensional bluff bodies," *Journal of Wind Engineering and Industrial Aerodynamics*, vol. 69, pp. 33–54, 1997.
- [20] Y. Nakamura, "Vortex shedding from bluff bodies with splitter plates," *Journal of Fluids and Structures*, vol. 10, no. 2, pp. 147–158, 1996.
- [21] D. McArthur, D. Burton, M. Thompson, and J. Sheridan, "On the near wake of a simplified heavy vehicle," *Journal of Fluids and Structures*, vol. 66, pp. 293–314, 2016.
- [22] S. Mansor and M. Passmore, "Measurement of a bluff body aerodynamic yaw moment magnification and damping using a dynamic wind tunnel facility," *Journal of Applied Mechanics*, vol. 78, no. 3, p. 031004, 2011.
- [23] S. Jovic and D. Driver, "Reynolds number effect on the skin friction in separated flows behind a backward-facing step," *Experiments in Fluids*, vol. 18, no. 6, pp. 464–467, 1995.
- [24] S. Jovic and D. M. Driver, "Backward-facing step measurements at low reynolds number, re (sub h)= 5000," *NASA Technical Memorandum 108807*, 1994.
- [25] A. Talmon, J. Kunen, and G. Ooms, "Simultaneous flow visualization and reynolds-stress measurement in a turbulent boundary layer," *Journal of Fluid Mechanics*, vol. 163, pp. 459–478, 1986.

- [26] P. Bearman, “Near wake flows,” *Journal of Wind Engineering and Industrial Aerodynamics*, vol. 69, pp. 125–127, 1997.
- [27] E. Konstantinidis and D. Bouris, “Bluff body aerodynamics and wake control,” in *Applied Aerodynamics*, InTech, 2012.
- [28] W. C. Meecham and M. T. Tavis, “Theoretical pressure correlation functions in turbulent boundary layers,” *The Physics of Fluids*, vol. 23, no. 6, pp. 1119–1131, 1980.
- [29] W. Willmarth and B. J. Tu, “Structure of turbulence in the boundary layer near the wall,” *The Physics of Fluids*, vol. 10, no. 9, pp. S134–S137, 1967.
- [30] W. W. Willmarth and C. E. Wooldridge, “Measurements of the fluctuating pressure at the wall beneath a thick turbulent boundary layer,” *Journal of Fluid Mechanics*, vol. 14, no. 2, pp. 187–210, 1962.
- [31] A. Favre, J. Gaviglio, and R. Dumas, “Space-time double correlations and spectra in a turbulent boundary layer,” *Journal of Fluid Mechanics*, vol. 2, no. 4, pp. 313–342, 1957.
- [32] A. Favre, J. Gaviglio, and R. Dumas, “Further space-time correlations of velocity in a turbulent boundary layer,” *Journal of Fluid Mechanics*, vol. 3, no. 4, pp. 344–356, 1958.
- [33] R. F. Blackwelder and L. S. Kovasznay, “Time scales and correlations in a turbulent boundary layer,” *The Physics of Fluids*, vol. 15, no. 9, pp. 1545–1554, 1972.
- [34] S. Ghaemi, D. Ragni, and F. Scarano, “Piv-based pressure fluctuations in the turbulent boundary layer,” *Experiments in fluids*, vol. 53, no. 6, pp. 1823–1840, 2012.
- [35] B. Lohrer, P. Valiorgue, H. B. Hadid, J. Frolich, and D. Doppler, “Pressure measurements using particle image velocimetry in the vicinity of a flexible moving structure,” in *PIV15, 11th International Symposium on Particle Image Velocimetry*, 2015.
- [36] J. McClure and S. Yarusevych, “Instantaneous piv/ptv-based pressure gradient estimation: a framework for error analysis and correction,” *Experiments in Fluids*, vol. 58, no. 8, p. 92, 2017.
- [37] B. Van Oudheusden, “Piv-based pressure measurement,” *Measurement Science and Technology*, vol. 24, no. 3, p. 032001, 2013.
- [38] A. Yakhot, H. Liu, and N. Nikitin, “Turbulent flow around a wall-mounted cube: A direct numerical simulation,” *International journal of heat and fluid flow*, vol. 27, no. 6, pp. 994–1009, 2006.

- [39] H. C. Lim, T. Thomas, and I. P. Castro, “Flow around a cube in a turbulent boundary layer: Les and experiment,” *Journal of Wind Engineering and Industrial Aerodynamics*, vol. 97, no. 2, pp. 96–109, 2009.
- [40] S. Krajnovic and L. Davidson, “Development of large-eddy simulation for vehicle aerodynamics,” in *ASME 2002 International Mechanical Engineering Congress and Exposition*, pp. 165–172, American Society of Mechanical Engineers, 2002.
- [41] S. A. Sisalah, E. G. Filali, and D. Cherrared, “A numerical study of coherent flow structures around a cubic bluff body using large eddy simulation,” *Journal of the Brazilian Society of Mechanical Sciences and Engineering*, vol. 38, no. 3, pp. 827–842, 2016.
- [42] S. E. Haupt, F. J. Zajackowski, and L. J. Peltier, “Detached eddy simulation of atmospheric flow about a surface mounted cube at high reynolds number,” *Journal of Fluids Engineering*, vol. 133, no. 3, p. 031002, 2011.
- [43] R. P. Wilson, S. E. Haupt, L. J. Peltier, and R. F. Kunz, *Detached eddy simulation of atmospheric flow about a surface mounted cube at high Reynolds number*. PhD thesis, Pennsylvania State University, 2006.
- [44] A. Curley, M. Uddin, and B. Peters, “Direct numerical simulation of turbulent flow around a surface mounted cube,” in *22nd AIAA Computational Fluid Dynamics Conference*, p. 3431, 2015.
- [45] M. Farhadi and K. Sedighi, “Flow over bluff bodies using les,” in *The Fourth International Symposium On Computational Wind Engineering (CWE2006)*, Yokohama, 2006.
- [46] D. Lakehal and W. Rodi, “Calculation of the flow past a surface-mounted cube with two-layer turbulence models,” *Journal of Wind Engineering and Industrial Aerodynamics*, vol. 67, pp. 65–78, 1997.
- [47] J. Paik, F. Sotiropoulos, and F. Porté-Agel, “Detached eddy simulation of flow around two wall-mounted cubes in tandem,” *International Journal of Heat and Fluid Flow*, vol. 30, no. 2, pp. 286–305, 2009.
- [48] Y. Gao and W. Chow, “Numerical studies on air flow around a cube,” *Journal of Wind Engineering and Industrial Aerodynamics*, vol. 93, no. 2, pp. 115–135, 2005.
- [49] K.-Y. Chien, “Predictions of channel and boundary-layer flows with a low-reynolds-number turbulence model,” *AIAA journal*, vol. 20, no. 1, pp. 33–38, 1982.
- [50] P. R. Spalart, “Strategies for turbulence modelling and simulations,” *International Journal of Heat and Fluid Flow*, vol. 21, no. 3, pp. 252–263, 2000.

- [51] S. D. Hall and T. J. Barber, “A detailed cfd and experimental investigation of a benchmark turbulent backward facing step flow.”
- [52] W. L. Oberkampf and M. F. Barone, “Measures of agreement between computation and experiment: validation metrics,” *Journal of Computational Physics*, vol. 217, no. 1, pp. 5–36, 2006.
- [53] I. Babuska and J. T. Oden, “Verification and validation in computational engineering and science: basic concepts,” *Computer Methods in Applied Mechanics and Engineering*, vol. 193, no. 36, pp. 4057–4066, 2004.
- [54] G. E. Erickson, D. Peak, J. Delfrate, A. M. Skow, and G. N. Malcolm, “Water facilities in retrospect and prospect: An illuminating tool for vehicle design,” 1986.
- [55] C. Beckner and R. E. Curry, “Water tunnel flow visualization using a laser,” *NASA Technical Memorandum 86743*, 1985.
- [56] D. Sabatino and T. Rossmann, “Tomographic piv measurements of a regenerating hairpin vortex,” *Experiments in Fluids*, vol. 57, no. 1, p. 6, 2016.
- [57] ELD, “Model 504 water tunnel,” tech. rep., 2017.
- [58] S. C. Ko, “Design and construction of a water tunnel,” tech. rep., Fritz Engineering Laboratory, Department of Civil Engineering, Lehigh University, 1971.
- [59] S. Hellman, *Experimental Investigation of Turbulent Wake Structures and Dynamic Coupling of Tandem Lifting Bodies in a Hydrodynamic Channel*. PhD thesis, UNCC (University of North Carolina at Charlotte), 2012.
- [60] J. Katz, *Race car aerodynamics: designing for speed*. R. Bentley, 2006.
- [61] Aerolab, “Educational wind tunnel,” 2017.
- [62] R. Ruderich and H. Fernholz, “An experimental investigation of a turbulent shear flow with separation, reverse flow, and reattachment,” *Journal of Fluid Mechanics*, vol. 163, pp. 283–322, 1986.
- [63] R. S. Thompson and R. E. Eskridge, “Turbulent diffusion behind vehicles: experimentally determined influence of vortex pair in vehicle wake,” *Atmospheric Environment (1967)*, vol. 21, no. 10, pp. 2091–2097, 1987.
- [64] P. M. Bevilaqua and P. S. Lykoudis, “Turbulence memory in self-preserving wakes,” *Journal of Fluid Mechanics*, vol. 89, no. 03, pp. 589–606, 1978.
- [65] C. E. Willert, “High-speed particle image velocimetry for the efficient measurement of turbulence statistics,” *Experiments in fluids*, vol. 56, no. 1, p. 17, 2015.

- [66] S. Watanabe, H. Kato, D.-Y. Kwak, M. Shirotake, and K. Rinoie, "Stereoscopic piv measurements of leading edge separation vortices on a cranked arrow wing," *Measurement Science and Technology*, vol. 15, no. 6, p. 1079, 2004.
- [67] F. J. Martins, J.-M. Foucaut, L. F. Azevedo, and M. Stanislas, "Near-wall study of a turbulent boundary layer using high-speed tomo-piv," in *Progress in Wall Turbulence 2*, pp. 347–356, Springer, 2016.
- [68] P. Tkacik, Z. Carpenter, A. Gholston, B. J. Cobb, S. Kennedy, E. Blankenship, M. Uddin, and S. P. K. Nukala, "A low cost rolling road for tire measurements in a small eiffel wind tunnel," tech. rep., SAE Technical Paper, 2017.
- [69] S. Arnette and B. Martindale, "Advances in wind tunnel aerodynamics for motorsport testing," tech. rep., SAE Technical Paper, 2000.
- [70] B. R. McAuliffe and A. D'Auteuil, "A system for simulating road-representative atmospheric turbulence for ground vehicles in a large wind tunnel," *SAE International Journal of Passenger Cars-Mechanical Systems*, vol. 9, no. 2016-01-1624, pp. 817–830, 2016.
- [71] J. Walter, J. Bordner, B. Nelson, and A. Boram, "The windshear rolling road wind tunnel," *SAE International Journal of Passenger Cars-Mechanical Systems*, vol. 5, no. 2012-01-0300, pp. 265–288, 2012.
- [72] K. Cooper, "Bluff-body aerodynamics as applied to vehicles," *Journal of Wind Engineering and Industrial Aerodynamics*, vol. 49, no. 1-3, pp. 1–21, 1993.
- [73] E. Maskell, "A theory of the blockage effects on bluff bodies and stalled wings in a closed wind tunnel," tech. rep., AERONAUTICAL RESEARCH COUNCIL LONDON (UNITED KINGDOM), 1963.
- [74] R. Gould, *Wake blockage corrections in a closed wind tunnel for one or two wall-mounted models subject to separated flow*. HM Stationery Office, 1969.
- [75] L. M. Couch and C. W. Brooks Jr, "Effect of blockage ratio on drag and pressure distributions for bodies of revolution at transonic speeds," 1973.
- [76] B. Mullany, H. Shahinian, J. Navare, F. Azimi, E. Fleischhauer, P. Tkacik, and R. Keanini, "The application of computational fluid dynamics to vibratory finishing processes," *CIRP Annals-Manufacturing Technology*, 2017.
- [77] E. Fleischhauer, F. Azimi, P. Tkacik, R. Keanini, and B. Mullany, "Application of particle image velocimetry (piv) to vibrational finishing," *Journal of Materials Processing Technology*, vol. 229, pp. 322–328, 2016.
- [78] E. Uhlmann, A. Dethlefs, and A. Eulitz, "Investigation of material removal and surface topography formation in vibratory finishing," *Procedia CIRP*, vol. 14, pp. 25–30, 2014.

- [79] N. Jain, J. M. Ottino, and R. M. Lueptow, “An experimental study of the flowing granular layer in a rotating tumbler,” *Physics of Fluids*, vol. 14, no. 2, pp. 572–582, 2002.
- [80] J. Navare, “Experimental and computational evaluation of a vibratory finishing process,” Master’s thesis, UNCC (University of North Carolina at Charlotte), 2017.
- [81] K. Hashemnia, A. Mohajerani, and J. K. Spelt, “Development of a laser displacement probe to measure particle impact velocities in vibrationally fluidized granular flows,” *Powder technology*, vol. 235, pp. 940–952, 2013.
- [82] K. Hashemnia and J. K. Spelt, “Particle impact velocities in a vibrationally fluidized granular flow: measurements and discrete element predictions,” *Chemical Engineering Science*, vol. 109, pp. 123–135, 2014.
- [83] D. Ciampini, M. Papini, and J. Spelt, “Impact velocity measurement of media in a vibratory finisher,” *Journal of materials processing technology*, vol. 183, no. 2-3, pp. 347–357, 2007.
- [84] A. Yabuki, M. Baghbanan, and J. Spelt, “Contact forces and mechanisms in a vibratory finisher,” *Wear*, vol. 252, no. 7-8, pp. 635–643, 2002.
- [85] J. L. Dahlberg, P. T. Tkacik, B. Mullany, E. Fleischhauer, H. Shahinian, F. Azimi, J. Navare, S. Owen, T. Bisel, T. Martin, J. Sholar, and R. G. Keanini, “An analog macroscopic technique for studying molecular hydrodynamic processes in dense gases and liquids,” *Journal of Visualized Experiments*, vol. 130, 2017.
- [86] M. Abdelrahman, “Investigation of turbulence in granular flow,” Master’s thesis, UNCC (University of North Carolina at Charlotte), 2017.
- [87] J. P. Boon and S. Yip, *Molecular hydrodynamics*. Courier Corporation, 1980.
- [88] D. Levesque and L. Verlet, “Computer” experiments” on classical fluids. iii. time-dependent self-correlation functions,” *Physical Review A*, vol. 2, no. 6, p. 2514, 1970.
- [89] D. Levesque and W. Ashurst, “Long-time behavior of the velocity autocorrelation function for a fluid of soft repulsive particles,” *Physical Review Letters*, vol. 33, no. 5, p. 277, 1974.
- [90] S. Lovesey, “Dynamics of solids and liquids by neutron scattering (topics in current physics vol 3) ed sw lovesey and t springer,” 1977.
- [91] T. Dorfmueller, “Bj berne and r. pecora: Dynamic light scattering, john wiley and sons ltd., baffins lane 1976, 376 seiten, preis:£ 14,.,” *Berichte der Bunsengesellschaft für physikalische Chemie*, vol. 81, no. 1, pp. 101–101, 1977.

- [92] M. P. Ciamarra, A. Coniglio, and M. Nicodemi, “Thermodynamics and statistical mechanics of dense granular media,” *Physical review letters*, vol. 97, no. 15, p. 158001, 2006.
- [93] B. J. Berne and R. Pecora, *Dynamic light scattering: with applications to chemistry, biology, and physics*. Courier Corporation, 2000.
- [94] D. Forster, *Hydrodynamic fluctuations, broken symmetry, and correlation functions*. CRC Press, 2018.
- [95] H. Herrmann, “On the thermodynamics of granular media,” *Journal de Physique II*, vol. 3, no. 4, pp. 427–433, 1993.
- [96] R. Keanini, P. T. Tkacik, E. Fleischhauer, H. Shahinian, J. Sholar, F. Azimi, and B. Mullany, “Macroscopic liquid-state molecular hydrodynamics,” *Scientific Reports*, vol. 7, p. 41658, 2017.
- [97] L. Graftieaux, M. Michard, and N. Grosjean, “Combining piv, pod and vortex identification algorithms for the study of unsteady turbulent swirling flows,” *Measurement Science and technology*, vol. 12, no. 9, p. 1422, 2001.
- [98] B. Wieneke, *PIV Uncertainty Quantification and Beyond*. PhD thesis, Delft University of Technology, 2017.
- [99] S. Burgmann, J. Dannemann, and W. Schröder, “Time-resolved and volumetric piv measurements of a transitional separation bubble on an sd7003 airfoil,” *Experiments in Fluids*, vol. 44, no. 4, pp. 609–622, 2008.
- [100] E. Paterna, P. Moonen, V. Dorer, and J. Carmeliet, “Mitigation of surface reflection in piv measurements,” *Measurement science and technology*, vol. 24, no. 5, p. 057003, 2013.
- [101] A.-J. Buchner, N. Buchmann, K. Kilany, C. Atkinson, and J. Soria, “Stereoscopic and tomographic piv of a pitching plate,” *Experiments in fluids*, vol. 52, no. 2, pp. 299–314, 2012.
- [102] J. G. Santiago, S. T. Wereley, C. D. Meinhart, D. Beebe, and R. J. Adrian, “A particle image velocimetry system for microfluidics,” *Experiments in fluids*, vol. 25, no. 4, pp. 316–319, 1998.
- [103] A. Schröder, R. Geisler, G. E. Elsinga, F. Scarano, and U. Dierksheide, “Investigation of a turbulent spot and a tripped turbulent boundary layer flow using time-resolved tomographic piv,” *Experiments in Fluids*, vol. 44, no. 2, pp. 305–316, 2008.
- [104] A. Schröder, R. GeisDaler, K. Staack, B. Wieneke, G. Elsinga, F. Scarano, and A. Henning, “Lagrangian and eulerian views into a turbulent boundary layer flow using time-resolved tomographic piv,” in *14th international symposium on applications of laser techniques of fluid mechanisms, Lisbon*, 2008.

- [105] F. Hegner, D. Hess, and C. Brücker, “Volumetric 3d piv in heart valve flow,” in *11th International Symposium on Particle Image Velocimetry*, 2015.
- [106] G. E. Elsinga, F. Scarano, B. Wieneke, and B. W. van Oudheusden, “Tomographic particle image velocimetry,” *Experiments in Fluids*, vol. 41, no. 6, pp. 933–947, 2006.
- [107] G. E. Elsinga, B. Wieneke, F. Scarano, and A. Schröder, “Tomographic 3d-piv and applications,” in *Particle image velocimetry*, pp. 103–125, Springer, 2007.
- [108] G. Elsinga and S. Tokgoz, “Ghost hunting an assessment of ghost particle detection and removal methods for tomographic-piv,” *Measurement Science and Technology*, vol. 25, no. 8, p. 084004, 2014.
- [109] R. Humble, G. Elsinga, F. Scarano, and B. Van Oudheusden, “Three-dimensional instantaneous structure of a shock wave/turbulent boundary layer interaction,” *Journal of Fluid Mechanics*, vol. 622, pp. 33–62, 2009.
- [110] G. Elsinga, J. Westerweel, F. Scarano, and M. Novara, “On the velocity of ghost particles and the bias errors in tomographic-piv,” *Experiments in fluids*, vol. 50, no. 4, pp. 825–838, 2011.
- [111] J. Sousa, “Turbulent flow around a surface-mounted obstacle using 2d-3c dpiv,” *Experiments in Fluids*, vol. 33, no. 6, pp. 854–862, 2002.
- [112] B. S. Thurow and T. Fahringer, “Recent development of volumetric piv with a plenoptic camera,” 2013.
- [113] DantecDynamics, “Flow field diagnostics: Particle image velocimetry solutions,” tech. rep., 2017.
- [114] R. D. Keane and R. J. Adrian, “Theory of cross-correlation analysis of piv images,” *Applied scientific research*, vol. 49, no. 3, pp. 191–215, 1992.
- [115] R. J. Adrian, “Particle-imaging techniques for experimental fluid mechanics,” *Annual review of fluid mechanics*, vol. 23, no. 1, pp. 261–304, 1991.
- [116] S. Scharnowski and C. J. Kähler, “On the loss-of-correlation due to piv image noise,” *Experiments in Fluids*, vol. 57, no. 7, p. 119, 2016.
- [117] R. Adrian, “Dynamic ranges of velocity and spatial resolution of particle image velocimetry,” *Measurement Science and Technology*, vol. 8, no. 12, p. 1393, 1997.
- [118] S. Scharnowski and C. J. Kähler, “Estimation and optimization of loss-of-pair uncertainties based on piv correlation functions,” *Experiments in Fluids*, vol. 57, no. 2, p. 23, 2016.

- [119] F. Mengel and T. Moerck, “Prediction of piv recording performance,” in *Laser Anemometry: Advances and Applications—Fifth International Conference*, pp. 331–338, International Society for Optics and Photonics, 1993.
- [120] T. Fuchs, R. Hain, and C. J. Kähler, “Double-frame 3d-ptv using a tomographic predictor,” *Experiments in Fluids*, vol. 57, no. 11, p. 174, 2016.
- [121] M. F. Kerho and M. B. Bragg, “Neutrally buoyant bubbles used as flow tracers in air,” *Experiments in Fluids*, vol. 16, no. 6, pp. 393–400, 1994.
- [122] F. Scarano, S. Ghaemi, G. C. A. Caridi, J. Bosbach, U. Dierksheide, and A. Sciacchitano, “On the use of helium-filled soap bubbles for large-scale tomographic piv in wind tunnel experiments,” *Experiments in Fluids*, vol. 56, no. 2, p. 42, 2015.
- [123] P. J. Schmid, D. Violato, and F. Scarano, “Decomposition of time-resolved tomographic piv,” *Experiments in Fluids*, vol. 52, no. 6, pp. 1567–1579, 2012.
- [124] M. Raffel, C. E. Willert, J. Kompenhans, *et al.*, *Particle image velocimetry: a practical guide*. Springer Science & Business Media, 2007.
- [125] J. Kitzhofer, T. Nonn, and C. Brücker, “Generation and visualization of volumetric piv data fields,” *Experiments in fluids*, vol. 51, no. 6, pp. 1471–1492, 2011.
- [126] A. Fouras, D. L. Jacono, C. V. Nguyen, and K. Hourigan, “Volumetric correlation piv: a new technique for 3d velocity vector field measurement,” *Experiments in fluids*, vol. 47, no. 4-5, p. 569, 2009.
- [127] G. Elsinga and I. Marusic, “Evolution and lifetimes of flow topology in a turbulent boundary layer,” *Physics of Fluids*, vol. 22, no. 1, p. 015102, 2010.
- [128] C. Atkinson and J. Soria, “An efficient simultaneous reconstruction technique for tomographic particle image velocimetry,” *Experiments in Fluids*, vol. 47, no. 4-5, p. 553, 2009.
- [129] H.-G. Maas, A. Stefanidis, and A. Gruen, “From pixels to voxels: Tracking volume elements in sequences of 3d digital images,” in *ISPRS Commission III Symposium: Spatial Information from Digital Photogrammetry and Computer Vision*, vol. 2357, pp. 539–547, International Society for Optics and Photonics, 1994.
- [130] P. Westfeld, H.-G. Maas, O. Pust, J. Kitzhofer, and C. Brücker, “3-d least squares matching for volumetric velocimetry data processing,” in *Proceedings of the 15th International Symposium on Applications of Laser Techniques to Fluid Mechanics*, pp. 5–8, 2010.
- [131] B. Wieneke, “Piv uncertainty quantification from correlation statistics,” *Measurement Science and Technology*, vol. 26, no. 7, p. 074002, 2015.

- [132] J. J. Charonko and P. P. Vlachos, “Estimation of uncertainty bounds for individual particle image velocimetry measurements from cross-correlation peak ratio,” *Measurement Science and Technology*, vol. 24, no. 6, p. 065301, 2013.
- [133] C. J. Kähler, S. Scharnowski, and C. Cierpka, “On the uncertainty of digital piv and ptv near walls,” *Experiments in fluids*, vol. 52, no. 6, pp. 1641–1656, 2012.
- [134] B. M. Wilson and B. L. Smith, “Uncertainty on piv mean and fluctuating velocity due to bias and random errors,” *Measurement Science and Technology*, vol. 24, no. 3, p. 035302, 2013.
- [135] A. Sciacchitano, B. Wieneke, and F. Scarano, “Piv uncertainty quantification by image matching,” *Measurement Science and Technology*, vol. 24, no. 4, p. 045302, 2013.
- [136] R. Lueptow, A. Akonur, and T. Shinbrot, “Piv for granular flows,” *Experiments in Fluids*, vol. 28, no. 2, pp. 183–186, 2000.
- [137] S. M. Soloff, R. J. Adrian, and Z.-C. Liu, “Distortion compensation for generalized stereoscopic particle image velocimetry,” *Measurement Science and Technology*, vol. 8, no. 12, p. 1441, 1997.
- [138] R. N. Chuk and V. J. Thomson, “A comparison of rapid prototyping techniques used for wind tunnel model fabrication,” *Rapid Prototyping Journal*, vol. 4, no. 4, pp. 185–196, 1998.
- [139] E. Kroll and D. Artzi, “Enhancing aerospace engineering students’ learning with 3d printing wind-tunnel models,” *Rapid Prototyping Journal*, vol. 17, no. 5, pp. 393–402, 2011.
- [140] T. Bisel, Tucker, J. L. Dahlberg, T. R. Martin, S. S. Owen, R. G. Keanini, P. T. Tkacik, N. Narayan, and N. Goudarzi, “A comparison of flat white aerosol and rhodamine (r6g) fluorescent paints and their effect on the results of tomographic piv measurements,” in *IMECE 2017, ASME, International Mechanical Engineering Congress and Exposition*, 2017.
- [141] H. Schlichting, “Boundary layer theory; trans. j. kestlin,” 1960.
- [142] B. R. Munson, T. H. Okiishi, A. P. Rothmayer, and W. W. Huebsch, *Fundamentals of fluid mechanics*. John Wiley & Sons, 2014.
- [143] B. Ewald, “Wind tunnel wall corrections (la correction des effets de paroi en soufflerie),” tech. rep., DTIC Document, 1998.
- [144] A. Melling, “Tracer particles and seeding for particle image velocimetry,” *Measurement Science and Technology*, vol. 8, no. 12, p. 1406, 1997.
- [145] DantecDynamics, “Dyanamicstudio user’s guide,” tech. rep., 2017.

- [146] F. G. Ergin, “Piv accuracy improvement near stationary walls using interrogation window masking,” in *PIV17, 12th International Symposium on Particle Image Velocimetry*, 2017.
- [147] H. Throop, S. Archer, H. C. Monger, and S. Waltman, “When bulk density methods matter: Implications for estimating soil organic carbon pools in rocky soils,” *Journal of Arid Environments*, vol. 77, pp. 66–71, 2012.
- [148] H. Lamb, *Hydrodynamics*. Cambridge university press, 1932.
- [149] J. Chaplin, “History forces and the unsteady wake of a cylinder,” *Journal of Fluid Mechanics*, vol. 393, pp. 99–121, 1999.
- [150] S. Kaplun, “Low reynolds number flow past a circular cylinder,” *Journal of Mathematics and Mechanics*, pp. 595–603, 1957.
- [151] S. Tomotika and T. Aoi, “The steady flow of viscous fluid past a sphere and circular cylinder at small reynolds numbers,” *The Quarterly Journal of Mechanics and Applied Mathematics*, vol. 3, no. 2, pp. 141–161, 1950.
- [152] B. Huner and R. Hussey, “Cylinder drag at low reynolds number,” *The Physics of Fluids*, vol. 20, no. 8, pp. 1211–1218, 1977.
- [153] “Viscosity tables,” 2010.
- [154] G. Elert, “Viscosity,” 1998.

APPENDIX A: WIND TUNNEL PROGRAMS AND CODE

A.1 LabVIEW[®] Data Acquisition Program Block Diagram for Wind Tunnel Pressures and Wind Velocity

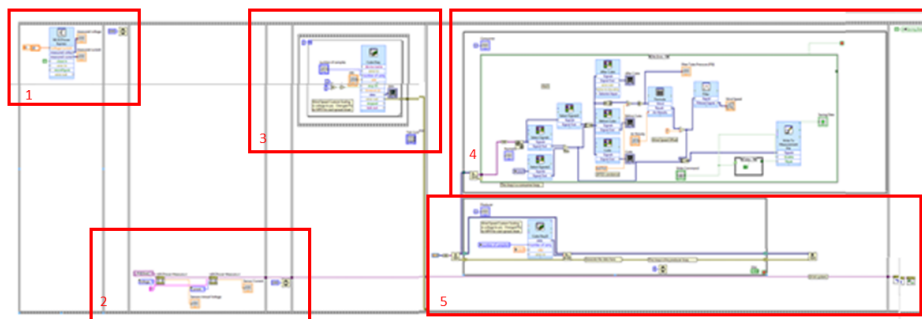


Figure A.1: Block diagram for LabVIEW[®] program used to acquire pressure and velocity data. Detailed areas outlined in red box is shown in following five figures.

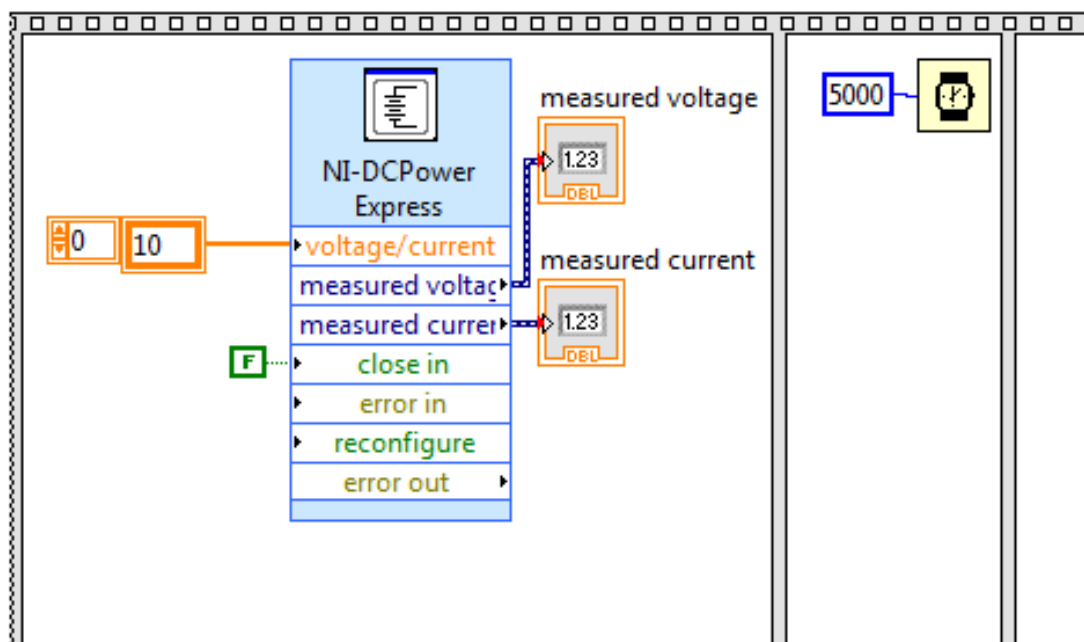


Figure A.2: Detailed view of block 1 from block diagram in Figure A.1

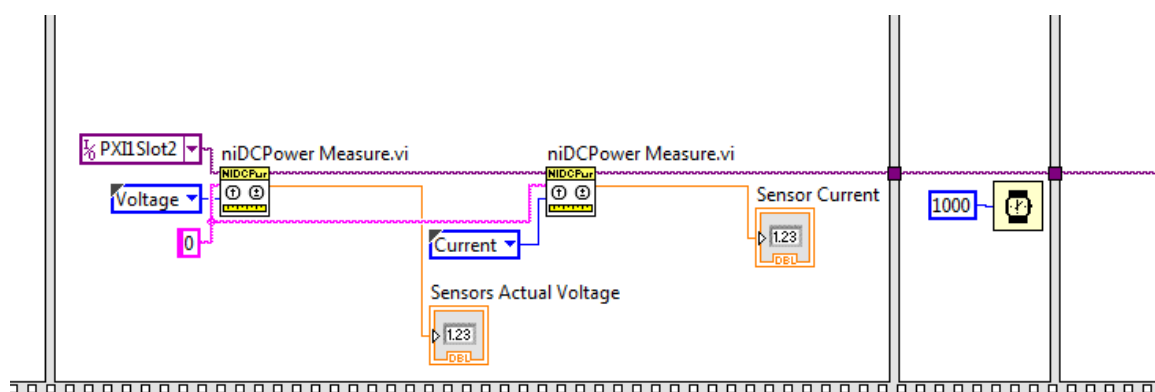


Figure A.3: Detailed view of block 2 from block diagram in Figure A.1

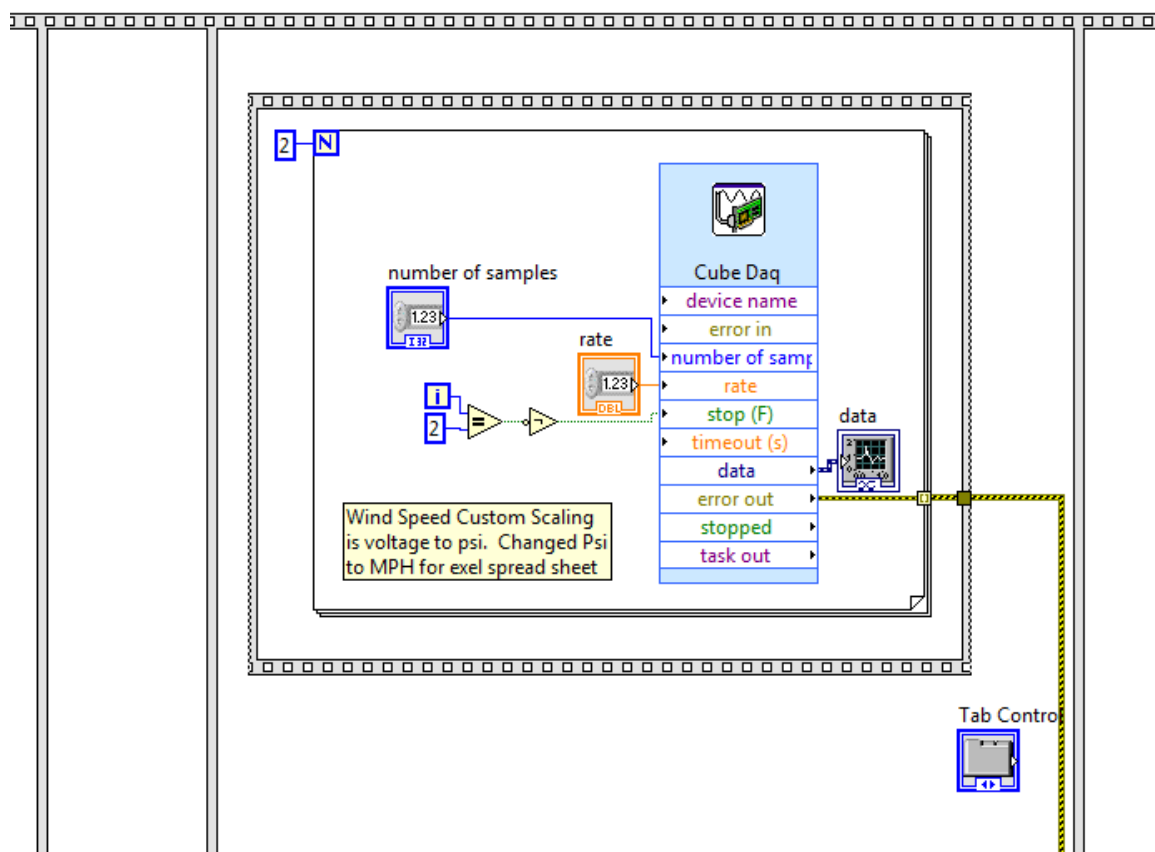


Figure A.4: Detailed view of block 3 from block diagram in Figure A.1

The screenshot displays a LabVIEW block diagram for a Producer-Consumer system. The diagram is divided into two main sections: the Producer and the Consumer. The Producer section, enclosed in a blue border, contains a 'Cube Data II' block and a 'Wind Speed Custom Scaling' block. The Consumer section, enclosed in a red border, contains a 'stop' block. The loop is controlled by a 'Generate the data here.' block and a 'This loop is the producer loop.' block. The diagram is labeled '32 bit system'.

A.2 MATLAB[®] Pressure Data Filtering Program

```
clc; clear all; close all;

%%%%%%%%%%%%%%%%%%%%%%%%%%%%%%%%%%%%%%%%%%%%%%%%%%%%%%%%%%%%%%%%%%%%%%%%%%%%%%
% Written by Jerry Dahlberg to filter cube pressure data.
%
% Pressure Sensor Cube Filtering Program for Wind tunnel Program
%
% using butterworth low pass filter.
%
%%%%%%%%%%%%%%%%%%%%%%%%%%%%%%%%%%%%%%%%%%%%%%%%%%%%%%%%%%%%%%%%%%%%%%%%%%%%%%

% import data

Front=xlsread('Compiledresults19April','Average','C24:C100024');
Right=xlsread('Compiledresults19April','Average','D24:D100024');
Top=xlsread('Compiledresults19April','Average','E24:E100024');
```

```

Left=xlsread('Compiledresults19April','Average','F24:F100024');
Rear=xlsread('Compiledresults19April','Average','G24:G100024');

%Variables
FS=10000; %Sampling Frequency
L=100001; %Number of samples
T=1/FS; %Sampling period
t=(0:L-1)*T; % Time vector
fnyquist = FS/2 %Nyquist frequency

%Figures
figure (1) %Plot Raw Data
plot(t,Front,' r', t, Right, 'c', t, Top,' g', t, Left, 'm', t,Rear,
' b')
grid;
legend ('Front', 'Right','Top','Left','Rear');
xlabel ('Time (sec)')
ylabel ('Pressure (MPa)')

% plot first half of DFT (normalized frequency) of magnitude spectrum
%of Front of cube
Front_mags=abs(fft(Front));
num_bins = length (Front_mags);
figure (2)
plot([0:1/(num_bins/2-1):1], Front_mags(1:num_bins/2))
xlabel('Normalised frequency (pi rads/sample)')
ylabel('Magnitude')

```

```

%design a second order filter using a butterworth
[b a] = butter(5,.004 , 'low')

%plot the frequncy response (normalised frequency)
FrontAA=freqz(b,a, floor(num_bins/2));
hold on
plot([0:1/(num_bins/2-1):1], abs(FrontAA), 'r');

%plot first half of DFT (normalized frequency) of magnitude spectrum
%of Right side pressure tap of cube
Right_mags=abs(fft(Right));
num_bins = length (Right_mags);
figure (3)
plot([0:1/(num_bins/2-1):1], Right_mags(1:num_bins/2))
xlabel('Normalised frequency (pi rads/sample)')
ylabel('Magnitude')

%design a second order filter using a butterworth
[c d] = butter(5,.002 , 'low')

%plot the frequncy response (normalised frequency)
RightBB=freqz(c,d, floor(num_bins/2));
hold on
plot([0:1/(num_bins/2-1):1], abs(RightBB), 'r');

%plot first half of DFT (normalized frequency) of magnitude spectrum

```



```

%of Top side pressure tap of cube
Top_mags=abs(fft(Top));
num_bins = length (Top_mags);
figure (4)
plot([0:1/(num_bins/2-1):1], Top_mags(1:num_bins/2))
xlabel('Normalised frequency (pi rads/sample)')
ylabel('Magnitude')

%design a second order filter using a butterworth
[f e] = butter(5,.003 , 'low')

%plot the frequncy response (normalised frequency)
TopAA=freqz(f,e, floor(num_bins/2));
hold on
plot([0:1/(num_bins/2-1):1], abs(TopAA), 'r');

%plot first half of DFT (normalized frequency) of magnitude spectrum
%of Left side pressure tap of cube
Left_mags=abs(fft(Left));
num_bins = length (Left_mags);
figure (5)
plot([0:1/(num_bins/2-1):1], Left_mags(1:num_bins/2))
xlabel('Normalised frequency (pi rads/sample)')
ylabel('Magnitude')

%design a second order filter using a butterworth
[g h] = butter(5,.003 , 'low')

```

```

%plot the frequncy response (normalised frequency)
LeftAA=freqz(g,h, floor(num_bins/2));
hold on
plot([0:1/(num_bins/2-1):1], abs(LeftAA), 'r');

%plot first half of DFT (normalized frequency) of magnitude spectrum
%of Rear side pressure tap of cube
Rear_mags=abs(fft(Rear));
num_bins = length (Rear_mags);
figure (6)
plot([0:1/(num_bins/2-1):1], Top_mags(1:num_bins/2))
xlabel('Normalised frequency (pi rads/sample)')
ylabel('Magnitude')

%design a second order filter using a butterworth
[i j] = butter(5,.003 , 'low')

%plot the frequncy response (normalised frequency)
RearAA=freqz(i,j, floor(num_bins/2));
hold on
plot([0:1/(num_bins/2-1):1], abs(RearAA), 'r');

%filter the signal using a and b butterworth coefficients
Front_filtered=filter(b,a,Front);
Right_filtered=filter(c,d,Right);
Top_filtered=filter(f,e,Top);

```

```

Left_filtered=filter(g,h,Left);
Rear_filtered=filter(i,j,Rear);

%Plot filtered Cube data
figure(7)
plot(t, Front_filtered,'r', t, Right_filtered, 'c', t, Top_filtered,
'g', t, Left_filtered,'m', t, Rear_filtered, 'b')
grid;
legend ('Front', 'Right','Top','Left', 'Rear');
xlabel ('Time (sec)')
ylabel ('Pressure (MPa)')

%Write filtered data to file
xlswrite('filteredpressure.xlsx', Front_filtered, 'Sheet1',
'D2:D100003');
xlswrite('filteredpressure.xlsx', Right_filtered,'Sheet1',
'E2:E100003');
xlswrite('filteredpressure.xlsx', Top_filtered,'Sheet1','F2:F100003');
xlswrite('filteredpressure.xlsx', Left_filtered,'Sheet1','G2:G100003');
xlswrite('filteredpressure.xlsx', Rear_filtered,'Sheet1','H2:H100003');

```

A.3 MATLAB® Pressure Data Correlation / Autocorrelation Program

```

clc; clear all; close all;

%%%%%%%%%%%%%%%%%%%%%%%%%%%%%%%%%%%%%%%%%%%%%%%%%%%%%%%%%%%%%%%%%%%%%%%%%%%%%%

% Matlab code written by Jerry Dahlberg to determine Correlation %
% and Autocorrelation values for experimental pressure data      %
% inside of the wind tunnel                                     %
%%%%%%%%%%%%%%%%%%%%%%%%%%%%%%%%%%%%%%%%%%%%%%%%%%%%%%%%%%%%%%%%%%%%%%%%%%%%%%

% import data

Speed=xlsread('Compiledresults19April','Average','B24:B100024');
Front = xlsread('Compiledresults19April','Average','C24:C100024');
Right = xlsread('Compiledresults19April','Average','D24:D100024');
Top = xlsread('Compiledresults19April','Average','E24:E100024');
Left = xlsread('Compiledresults19April','Average','F24:F100024');
Back = xlsread('Compiledresults19April','Average','G24:G100024');
a = xlsread('Compiledresults19April','Average','H24:H100024');
b = xlsread('Compiledresults19April','Average','I24:I100024');
h = xlsread('Compiledresults19April','Average','J24:J100024');
i = xlsread('Compiledresults19April','Average','K24:K100024');
j = xlsread('Compiledresults19April','Average','L24:L100024');
k = xlsread('Compiledresults19April','Average','M24:M100024');
l = xlsread('Compiledresults19April','Average','N24:N100024');
m = xlsread('Compiledresults19April','Average','O24:O100024');
n = xlsread('Compiledresults19April','Average','P24:P100024');
oo = xlsread('Compiledresults19April','Average','Q24:Q100024');
p = xlsread('Compiledresults19April','Average','R24:R100024');

```

```

figure (1)
plot(Speed); % plot velocity for duration of experiment.
grid;
title('Speed of Wind Tunnel');
xlabel('Time');
ylabel('Velocity (meter per second)')

%Variables
Vel=mean(Speed)%Average Velocity for duration of experiment.

% Autocorrelation for single variable.  Change variable to get
% autocorrelation for each location. An autocorrelation of 1 is
% perfectly correlated, 0 is no correlation.  Any peak under .5 is
% weakly correlated.

AA=autocorr(Front, 100000);
figure (2)
plot (AA);
grid;
xlabel ('lags')
ylabel ('Autocorrelation')

% Crosscorrelation for two variable.  Change second variable to get
% crosscorrelation between the two locations.

```

```
figure(3)
crosscorr(Front,Top, 100000,25)
title('')
xlabel('Time Lag')
ylabel('Cross Correlation')

figure(4)
crosscorr(Front,Right, 100000,25)
title('')
xlabel('Time Lag')
ylabel('Cross Correlation')

figure(5)
crosscorr(Front,Left, 100000,25)
title('')
xlabel('Time Lag')
ylabel('Cross Correlation')

figure(6)
crosscorr(Front,Back, 100000,25)
title('')
xlabel('Time Lag')
ylabel('Cross Correlation')
end
```

A.4 Wake Region Cross-Correlation Tables

Table A.1: Cross-Correlation with Sensor H

Sensor	Magnitude	Number of Lags
I	0.5586	57
J	0.0	0
K	0.3499	0
L	0.3428	0
M	0.3743	126
N	0.3752	0
O	0.4256	0

Table A.2: Cross-Correlation with Sensor I

Sensor	Magnitude	Number of Lags
H	0.5586	-57
J	0.4736	58
K	0.2799	141
L	0.2444	-4
	0.1642	-114
	0.1195	-245
	0.1593	107
	0.1724	194
	0.1215	311
M	0.2383	9
	0.2383	93
	0.2499	222
N	0.2765	0
O	0.3053	0

Table A.3: Cross-Correlation with Sensor J

Sensor	Magnitude	Number of Lags
H	0	0
I	0.4736	-58
K	0.1922	-79
	0.4859	52
	0.1918	183
L	0.1759	-114
	0.2060	0
	0.2978	102
	0.1750	210
M	0.2149	18
	0.2780	155
	0.1835	332
N	0.2387	-66
	0.1471	-207
	0.2537	42
	0.1537	241
	0.1135	378
O	0.2865	0
	0.1407	300

Table A.4: Cross-Correlation with Sensor K

Sensor	Magnitude	Number of Lags
H	0.3499	0
I	0.2799	-141
J	0.4859	-52
	0.1918	-183
	0.1922	79
L	0.2266	-73
	0.1287	-182
	0.5335	48
	0.1862	169
M	0.2297	-41
	0.4162	91
N	0.3061	5
	0.2992	135
O	0.2844	0
	0.2719	45
	0.2419	186

Table A.5: Cross-Correlation with Sensor L

Sensor	Magnitude	Number of Lags
H	0.3428	0
I	0.1593	-107
	0.1724	-194
	0.1215	-311
	0.2444	4
	0.1642	114
	0.1195	245
J	0.2978	-102
	0.1750	-210
	0.2060	0
	0.1759	114
K	0.5335	-48
	0.1862	-169
	0.2266	73
	0.1287	182
M	0.2853	-88
	0.6643	45
	0.3196	168
	0.2212	272
	0.1667	391
N	0.3123	-41
	0.2023	-174
	0.4757	89
	0.1982	221
O	0.2507	-119
	0.1092	-348
	0.3474	0
	0.3735	126

Table A.6: Cross-Correlation with Sensor M

Sensor	Magnitude	Number of Lags
H	0.3743	-126
I	0.2383	-9
	0.2383	-93
	0.2499	-222
J	0.2149	-18
	0.2780	-155
	0.1835	-332
K	0.4162	-91
	0.2297	41
L	0.6643	-45
	0.3196	-168
	0.2212	-272
	0.1667	-391
	0.2853	88
N	0.3660	-85
	0.3042	-195
	0.6809	46
	0.2531	179
O	0.3551	-40
	0.3465	-156
	0.5135	86
	0.2151	213

Table A.7: Cross-Correlation with Sensor N

Sensor	Magnitude	Number of Lags
H	0.4256	0
I	0.2765	0
J	0.2537	-42
	0.1537	-241
	0.1135	-378
	0.2387	66
	0.1471	207
K	0.3061	-5
	0.2992	-135
L	0.4757	-89
	0.1982	-221
	0.3123	41
	0.2023	174
M	0.6809	-46
	0.2531	-179
	0.3660	85
	0.3042	195
O	0.3768	-84
	0.7714	39
	0.3210	162

Table A.8: Cross-Correlation with Sensor O

Sensor	Magnitude	Number of Lags
H	0.4256	0
I	0.3053	0
J	0.1407	-300
	0.2865	0
K	0.2719	-45
	0.2419	-186
	0.2844	0
L	0.3735	-126
	0.3474	0
	0.2507	119
	0.1092	348
M	0.5135	-86
	0.2151	-213
	0.3551	40
	0.3465	156
N	0.7714	-39
	0.3210	-162
	0.3768	84

APPENDIX B: VIBRATED GRAIN PILE PROGRAM AND CODE

B.1 LabVIEW[®] Frequency Data Acquisition Program Block Diagram

Gather Data from Accelerometer for 10 seconds, 1K Samples per Second. The results are presented on the Front Panel for X, Y, and Z and written to a file on the desk top for future analysis.

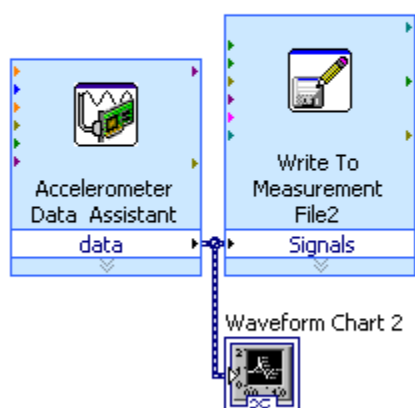


Figure B.1: Block diagram for LabVIEW[®] program used to acquire accelerometer data in vibratory polishing experiments

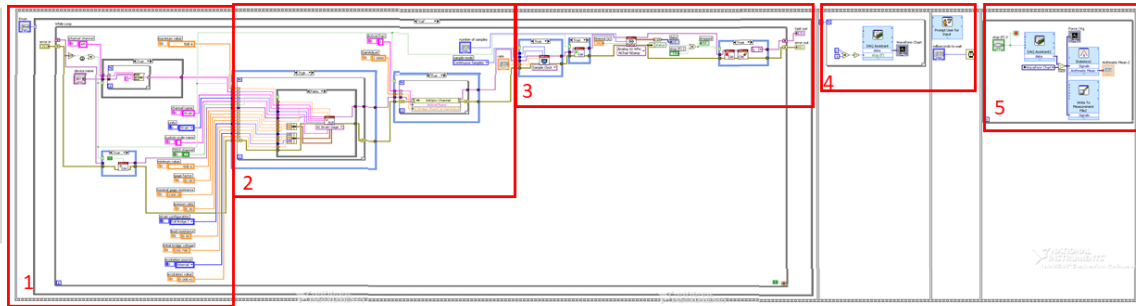


Figure B.2: Block diagram for LabVIEW[®] program used to acquire force data in vibratory polishing experiments. Detailed areas outlined in red box is shown in following five figures.

B.2 LabVIEW[®] Force Data Acquisition Program Block Diagram

Figure B.3: Detailed view of block 1 from block diagram in Figure B.2

Figure B.6: Detailed view of block 4 from block diagram in Figure B.2

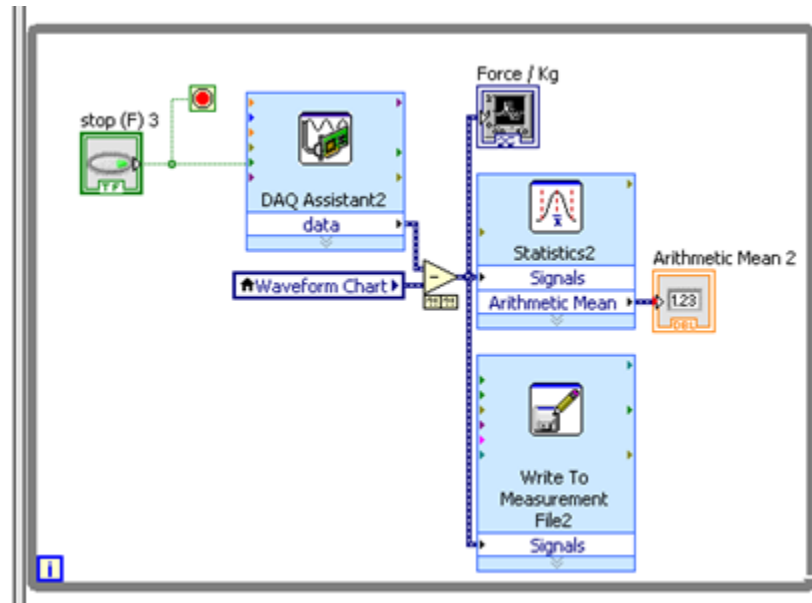


Figure B.7: Detailed view of block 5 from block diagram in Figure B.2

B.3 MATLAB[®] Image Conversion Program

```

clc; clear all; close all;

%%%%%%%%%%%%%%%%%%%%%%%%%%%%%%%%%%%%%%%%%%%%%%%%%%%%%%%%%%%%%%%%%%%%%%%%%%%%%%

%Written by Tucker Bisel for JoVE article and modified by Jerry      %
%Dahlberg. Read in images and convert from color to grayscale for PIV%
%processing imwrite(rgb2gray(imread(Image Location\Image Name.tif,   %
%'tif'))),Save location\Save Name.tif, '.tif'));                      %
%%%%%%%%%%%%%%%%%%%%%%%%%%%%%%%%%%%%%%%%%%%%%%%%%%%%%%%%%%%%%%%%%%%%%%%%%%%%%%

%convert calibration image from RGB to Grayscale.
imwrite(rgb2gray(imread('F:\JoVE Files\56632_calibration\56632_
calibration _001\Calibration.tif','tif')),'B:\Image Imports\Grayscale
Calibration\Calibration.tif');

for x = 0 : 4999 % For Number of Images in file (excluding

```

calibration) Loop

```
% imwrite(rgb2gray(imread(strcat('Image Location, Image Name',
%sprintf ('%06d',x),'.tif'),'.tif')),strcat('Image New Location\
%Image New Name Grayscale',sprintf('%06d',x),'.tif'));
imwrite(rgb2gray(imread(strcat('F:\JoVE Files\56632_RunFinal\
56632_RunFinal_001\Right Side',sprintf('%06d',x),'.tif'),
'tif')), strcat('B:\Image Imports\Grayscale Conversion
Demo\Right Side', sprintf('%06d',x),'.tif'));
end
```

```
%Loop converts images in order from RGB to Grayscale, location
%addresses will need to be inserted into the file names depending on
%image names and locations. strcat concatenates string horizontally,
%sprintf formats data into string
```

B.4 Reynolds number / Coefficient of Drag Table

Table B.1: Reynolds Number Comparison

Reynolds Number	Oseen (1st term)	Oseen (2 terms)	Chaplin
0.001	1529.3433	1509.6365	1474.0670
0.002	835.1198	822.2845	827.4441
0.003	588.4597	578.3557	587.6784
0.004	459.9329	451.3565	460.5115
0.005	380.3725	372.7925	381.0480
0.006	325.9718	319.1020	326.4100
0.007	286.2726	279.9393	286.3988
0.008	255.9384	250.0271	255.7581
0.009	231.9522	226.3832	231.4952
0.010	212.4760	207.1911	211.7768
0.011	196.3238	191.2794	195.4155
0.012	182.69535	177.8576	181.6072
0.013	171.0302	166.3721	169.7874
0.014	160.9238	156.4237	159.5478
0.015	152.0766	147.7168	150.5858
0.016	144.2619	140.0275	142.6717
0.017	137.3049	133.1834	135.6284
0.018	131.0684	127.0492	129.3169
0.019	125.4434	121.5174	123.6265
0.020	120.3420	116.5013	118.4679
0.021	115.6925	111.9302	113.7684
0.022	111.4360	107.7461	109.4680
0.023	107.5235	103.9005	105.5168
0.024	103.9137	100.3529	101.8730
0.025	100.5719	97.0691	98.5013
0.026	97.4686	94.0200	95.3716
0.027	94.5785	91.1806	92.4583
0.028	91.8797	88.5295	89.7390
0.029	89.3534	86.0479	87.1946
0.030	86.9830	83.7198	84.8084
0.031	84.7542	81.5308	82.5656
0.032	82.6543	79.4686	80.4534
0.033	80.6721	77.5222	78.4604
0.034	78.7977	75.6817	76.5767
0.035	77.0224	73.9385	74.7931
0.036	75.3381	72.2850	73.1018
0.037	73.7380	70.7140	71.4956
0.038	72.2157	69.2195	69.9680

Table B.2: Reynolds Number Comparison Continued

Reynolds Number	Oseen (1st term)	Oseen (2 terms)	Chaplin
0.039	70.76544	67.7958	68.5132
0.040	69.3821	66.4379	67.1261
0.041	68.0610	65.1411	65.8019
0.042	66.7979	63.9013	64.5363
0.043	65.5890	62.7147	63.3254
0.044	64.4308	61.5779	62.1656
0.045	63.3200	60.4877	61.0537
0.046	62.2538	59.4411	59.9867
0.047	61.2293	58.4356	58.9618
0.048	60.2441	57.4687	57.9766
0.049	59.2960	56.5382	57.0286
0.050	58.3828	55.6419	56.1159
0.051	57.5026	54.7780	55.2363
0.052	56.6535	53.9446	54.3881
0.053	55.8339	53.1402	53.5696
0.054	55.0422	52.3632	52.7791
0.055	54.2770	51.6121	52.0153
0.056	53.5369	50.8858	51.2768
0.057	52.8207	50.1828	50.5623
0.058	52.1272	49.5021	49.8705
0.059	51.4553	48.8426	49.2005
0.060	50.8040	48.2033	48.5512
0.061	50.1724	47.5832	47.9215
0.062	49.5594	46.9815	47.3107
0.063	48.9643	46.3973	46.7177
0.064	48.3863	45.8299	46.1419
0.065	47.8246	45.2785	45.5825
0.066	47.2785	44.7424	45.0388
0.067	46.7475	44.2209	44.5101
0.068	46.2307	43.7135	43.9957
0.069	45.7277	43.2196	43.4951
0.070	45.2379	42.7387	43.0077
0.071	44.7607	42.2701	42.5330
0.072	44.2957	41.8134	42.0704
0.073	43.8424	41.3682	41.6196
0.074	43.4003	40.9340	41.1800
0.075	42.9691	40.5104	40.7512
0.076	42.5482	40.0970	40.3328
0.077	42.1374	39.6935	39.9245
0.078	41.7362	39.2994	39.5258

APPENDIX C: CURRICULUM VITAE

Jerry Dahlberg

1940 Winsted Ct. Charlotte N.C. 28262, (704)776-8895 jdahlbe2@uncc.edu

EDUCATION

University of North Carolina at Charlotte, Charlotte, NC

Doctor of Philosophy in Mechanical Engineering Dec 2018

Dissertation: *Aspects of Turbulence and Stochastic Processes in Fluid Mechanics*

Advisor: Dr. Peter Tkacik

Masters of Science in Mechanical Engineering May 2016

Bachelor of Science in Mechanical Engineering May 2014

University of Maryland University College, Ft. Benning, GA

Bachelor of Art in Business Management (106 hrs) GPA 3.83

Associates of Arts in General Curriculum Dec 2004

PROFESSIONAL ASSOCIATIONS

Member; American Physical Society 2017

Member; American Society for Engineering Education
2017

Member; Society of Automotive Engineers 2015

Member; American Institute of Aeronautics and Astronautics 2013

President; UNCC Rocketry and Projectile Club 2012-2015

Member; National Association of Rocketry 2012

Member; American Society of Mechanical Engineers 2011

Member; National Society of Professional Engineers 2011

HONORS/AWARDS

Outstanding Graduate Student (2017-2018)

Service to Department Award; Lee College of Engineering (2017-2018)

Service to Department Award; Lee College of Engineering (2016-2017)

Service to Department Award; Lee College of Engineering (2015-2016)

Benjamin O. Hood Service Award (2013-2014)

MAPS Scholar; University of North Carolina at Charlotte

Chancellors List; University of North Carolina at Charlotte

Deans List; University of North Carolina at Charlotte and University of Maryland

University College Sigma Alpha Lambda (Leadership and Honors Society)

Phi Kappa Phi (Leadership and Honors Society)

PUBLICATIONS

Lim, J. H., Interiano, C. G., Nowell, C. E., Tkacik, P. T., & Dahlberg, J. L., Invisible cultural barriers: Contrasting perspectives on student veterans transition. *Journal of College Student Development*. 59(3), 291-308, DOI: 10.1353/CSD.2018.0028 (2018).

Dahlberg, J.L. , Tkacik, P. T., Mullany, B., Fleischhauer, E., Shahinian, H., Azimi, F., et al. An Analog Macroscopic Technique for Studying Molecular Hydrodynamic Processes in Dense Gases and Liquids. *J. Vis. Exp.* (130), e56632, DOI: 10.3791/56632 (2017).

PEER REVIEWED CONFERENCE PROCEEDINGS

Lim, J., Dahlberg, J.L., Findlater, N.A., Faw, L., Interiano, C.G., Hunt, B., Tkacik, P.T., and Nguyen, N.V., "Our Little World": (Un)envisioning the Social and

Ethical Implications of Engineering”. Proceeding of the Frontiers in Education Conference (FIE). San Jose, Ca, October 2018

Interiano, C.G., Tkacik, P.T., Dahlberg, J.L., and Lim, J., "Authentic Knowledge, Learning Outcomes, and Professional Identity: A Mixed-Methods Study of a Successful Engineering Course", Proceeding of the Frontiers in Education Conference (FIE). San Jose, Ca, October 2018

Gambil, S., Narayan, N., Dahlberg, J.L., Tkacik, P.T. and Goudarzi, N., "Aerodynamic Study of Flow Around a Tire on a Rolling Road". Thirty seventh annual meeting of The Tire Society. Akron, Oh, September 2018

Interiano, C.G. Lim, J., Tkacik, P.T., and Dahlberg, J.L., "The few, the proud, the marginalized: Minority student veterans identity rupture in racialized America". Annual meeting of the American Educational Research Association (AERA). New York, NY, 2018

Lim, J., Interiano, C.G., Tkacik, P.T. and Dahlberg, J.L., "Gendered interpretation of legitimate knowledge: How female engineering students construct meaning in military technology class". Annual meeting of the American Educational Research Association (AERA). New York, NY 2018

Bisel, T., Dahlberg, J., Martin, T., Owen, S., Tkacik, P.T., Keanini, R.G., Narayan, N., and Goudarzi, N., A Comparison of Flat White Aerosol and Rhodamine (R6G) Fluorescent Paints and Their Effect on the Results of Tomographic PIV Measurements in the Proceedings of the International Mechanical Engineering Congress and Exposition (IMECE), IMECE Paper ID# 71507, Tampa, FL, November 2017

Claudia G. Interiano, Jae Hoon Lim, Carolina E. Nowell, Peter T. Tkacik, Jerry L. Dahlberg Challenging Unidimensional Models of Student Veterans Cultural Transition: A Multi-layered Framework in the Proceedings of the Association for the Study of Higher Education (ASHE), Houston, TX, November 2017

Jae Hoon Lim, Peter T. Tkacik, Claudia G. Interiano, Jerry L. Dahlberg and Carolina E. Nowell, Engineering as a Pathway to Reintegration: Student Veterans Transition Experience into Higher Education in the Proceedings of the American Society for Engineering Education (ASEE), ASEE Paper ID# 14987, New Orleans, LA, June 2016

CONFERENCE PRESENTATIONS

Jerry Dahlberg, Claudia Interiano, Patricia Tolley, Peter Tkacik and Jae Hoon Lim, "Engaging Military Veterans to Increase STEM Enrollment and Degrees Awarded: The Second Year", UNC Charlotte College of Health and Human Service Veterans Health Conference 2017

Eric Fleischhauer, Jerry L. Dahlberg, Tucker T. Bisel, Peter T. Tkacik, and Samuel Hellman. "Tomographic PIV Measurement in a Bluff Body Wake Utilizing an Asymmetric Camera Configuration and Least Squares Matching", 55th AIAA Aerospace Sciences Meeting, AIAA SciTech Forum, (AIAA 2017-1644)

Jerry Dahlberg, Claudia Interiano, Peter Tkacik and Jae Hoon Lim, "Engaging Military Veterans to Increase STEM Enrollment and Degrees Awarded", UNC Charlotte College of Health and Human Service Veterans Health Conference 2016

Claudia Interiano, Jerry Dahlberg, Dymilah Hewitt and Jae Hoon Lim, "Supporting Student Veterans: Identity Reintegration in Higher Education, UNC Charlotte College of Health and Human Service Veterans Health Conference 2016

Jerry Dahlberg, Daniel Deese, Daniel Saulnier, Robert Stone, Matthew Perry, Caleb Watts, Dewey Greer and Benjamin Griffith, "Thrust Modulation of a Solid Fuel Rocket Controlled Using NI MyRio and LabVIEW", National Instruments Week 2014 - Student Design Competition

MILITARY SERVICE

2 Years Army Reserve

Stationed at Sioux City, IA; 1988-1990

20 Years Active Army

Stationed at Nurnberg Germany; 1990-1992

Ft. Riley, KS; 1992-1994

Stuttgart, Germany; 1995-1998

Ft. Benning, GA; 1998-2000

Vicenza, Italy; 2001-2005

Ft. Benning, GA; 2005-2012

Multiple Deployments to the former Republic of Yugoslavia and Iraq

Retired from Active Federal Service May 31 2010

AWARDS

Bronze Star awarded twice; Meritorious Service Medal awarded twice; Army Accommodation Medal awarded three times; Army Achievement Medal awarded seven times; Combat Action Badge; Meritorious Unit Citation

DD 214 available upon request

SUMMARY OF QUALIFICATIONS

- Over 15 years experience as a mid-level manager of over 40 employees
- Experience working as part of a team and as an individual; excellent attention to detail
- Submitted comprehensive and timely reports to supervisor and senior leadership
- Worked under extreme pressure, multi tasked, met tight deadlines and made difficult decisions in stressful environment while enforcing 100% of the company policies and procedures
- Proficient in Microsoft Office Programs to include Word, Power point, Excel and Access
- Five years experience working with ProE Creo 2.0, Solidworks, Matlab, Mathcad and Labview

RESEARCH EXPERIENCE

Student Launch Initiative (NASA)

May 2013-May 2014

Senior Capstone Project: Modifying Thrust of a Solid Fuel Rocket Motor

Team lead for the project to design, document, test and launch a student-built solid rocket thrust modulation experimental vehicle. A variable extension slider was used to effectively change the shape of the nozzle, altering the efficiency of the nozzle and attenuating the thrust to reach a target altitude. The control system featured a closed-loop system based on accelerometer readings programmed in LabVIEW. The vehicle also had a ground hazard identification system, atmospheric sensor package and body stress analysis package designed by the team. The team placed third at the UNC Charlotte Senior Design Expo and won Best Vehicle Design for the most creative, innovative, and well-constructed overall vehicle design for the

intended payload while maximizing safety and efficiency at the NASA Student Launch Competition.

Scholars Research for Undergraduates

May 2013- Aug 2013

Undergraduate Research Project: Measurement of Compressible Flow Separation in a Planar Rocket Nozzle

- Conducted research on shock-boundary layer interactions within rocket nozzles
- Utilized High-Speed Schlieren Imaging to analyze shock-boundary layers and side loads
- Conducted analytical modeling of supersonic rocket nozzle flows

WORK EXPERIENCE

University of North Carolina Charlotte

July 2018- Current

Associate Professor of Practice / Senior Design Committee Chair

- Oversees academic issues related to the Senior Design program
- Oversees coordination, logistics, and infrastructure associated with the colleges Senior Design Program
- Evaluates capstone design project scopes proposed by industry supporters and assigns students to teams
- Mentors multi-disciplinary teams and grade student work
- Supports other faculty who serve as project mentors

University of North Carolina Charlotte

May 2014- July 2018

Research Assistant

- Managed Veteran STEM education outreach and recruitment program

- Designed and supervised overhaul of 100 mile per hour wind tunnel and scaled rolling road
- Assisted with upgrade of PIV system to TopoPIV system

University of North Carolina Charlotte

Jan 2013- May 2014

Grader / Teaching Assistant

- Assisted with supplemental instruction for Static Mechanics and Manufacturing Systems
- Graded assignments for Manufacturing Systems and Static Mechanics
- Worked with fellow students on Static Mechanics, Thermodynamics and Physics

Cutter Tech

Apr 2010-Feb 2011

Insituform Technologies

Monroe, NC

- Maintained and operated IBOT and Aries crawler sewer taping and tap cutting equipment and vehicle
- Installed cured-in-place-pipe line to rehabilitate deteriorated sewer lines

U.S. Army

Feb 1998-May 2010

Platoon Sergeant/Mid-Level Manager

May 2005-May 2010 Fort

Benning, GA (Final Duty Assignment)

- Successfully planned, supervised and conducted over 600 combat patrols and operations
- Worked as part of a multi-national combat operations team involving over 30 team members
- Trained Iraqi Police and Army on job skills including force protection, operations planning and public relations

- Supervised the training of over 160 Soldiers on civilian law enforcement and combat operations
- Maintained composure in daily stressful, dangerous and life threatening situations under strict time lines

Police Station Operations Sergeant

Feb 2001-May 2005

Vicenza, Italy

- Responded to and supervised crowd control operations while maintaining good public relations with foreign nationals
- Wrote, implemented, supervised and inspected post security procedures for military community
- Briefed senior leaders on incidents, cases and security shortcomings in a timely manner